Dielectrophoretic filtration of particles in porous media: Concept, design, and selectivity

Vom Fachbereich Produktionstechnik
der
UNIVERSITÄT BREMEN

zur Erlangung des Grades
Doktor-Ingenieur
genehmigte

Dissertation
von
Malte Lorenz, M.Sc.

Gutachter: Prof. Dr.-Ing. Jorg Thöming
(Universität Bremen)
Prof. Dr.-Ing. Sergiy Antonyuk
(Technische Universität Kaiserslautern)

Tag der mündlichen Prüfung: 22.04.2021

Zusammenfassung

Die Trennung mikro- und submikroskaliger Partikel von Flüssigkeiten und voneinander gemäß ihrer Eigenschaften ist eine schwierige und teils ungelöste Aufgabe vieler industrieller Prozesse. Neue Trenntechniken werden benötigt um diese Aufgaben zu lösen.

Dielektrophorese (DEP) beschreibt die Bewegung polarisierbarer Partikel in inhomogenen elektrischen Feldern, welche zur hochselektiven Partikeltrennung nach deren Größe, Material und innerer Struktur (Morphologie) und ohne die Partikeleigenschaften zu verändern genutzt werden kann. Die meisten DEP-basierten Partikeltrenntechniken nutzen mikrofluidische Kanäle, die für Durchsätze industriellen Maßstabs ungeeignet sind. Der Grund dafür liegt in den hohen Feldgradienten, welche für ausreichend große dielektrophoretische Kräfte notwendig sind. Die dielektrophoretische Kraft skaliert mit dem Gradienten des Quadrats des elektrischen Felds, $\nabla|\mathbf{E}|^2$. Die Einheit dieses Gradienten ist $\mathrm{V^2\,m^{-3}}$, was verdeutlicht, dass hohe Spannungen und kleine Maßstäbe für einen hohen Gradienten notwendig sind. $\nabla|\mathbf{E}|^2$ ist groß an Grenzflächen von Materialien unterschiedlicher dielektrischer Eigenschaften, aber fällt mit zunehmendem Abstand von Grenzflächen schnell auf geringe Werte ab. Ein alternativer Ansatz zur Lösung der Durchsatzlimitierung ist die dielektrophoretische Filtration. Bei dieser Technik werden offenporige Filter verwendet, welche eine große Anzahl gewundener Kanäle aufweisen und daher einen hohen Durchsatz ermöglichen. Das elektrische Feld wird an der Oberfläche des Filters gestört, sodass hohe Feldgradienten und gute Bedingungen zur dielektrophoretischen Partikelrückhaltung bestehen. Die wenigen Studien über dielektrophoretische Filtration lösen sehr spezifische Trennprobleme aber eignen sich nicht, um die physikalischen Grundlagen der DEP Filtration zu verstehen. Ein solches Verständnis ist jedoch erforderlich, um neue Anwendungen dieses Trennverfahrens zu entwickeln.

Diese Arbeit beleuchtet DEP Filtration in einer umfassenden experimentellen Studie um fundamentales Verständnis zu erlangen. Dafür wurde zunächst ein DEP Filteraufbau zur Durchführung der Experimente konzipiert und aufgebaut. In der entwickelten Filterzelle wurde nahezu hundertprozentige Partikelabtrennung (Polystyrol, 500 nm) bei Volumendurchflüssen von $9\,\mathrm{mL\,min^{-1}}$ erreicht (Filterquerschnittsfläche: $2\,\mathrm{cm^2}$). In einer Parameterstudie wurde die Abhängigkeit der Abtrenneffizienz als Funktion der angelegten

elektrischer Spannung (ΔU), des volumetrischen Durchflusses (Q), und des hydraulischen Porendurchmessers (d_h) untersucht. Die Abtrenneffizienz kann als Funktion einer Variablen $\bar{x}$ beschrieben werden, welche die Prozessparameter und deren Einfluss enthält, $\bar{x} = (\Delta U)^2 Q^{-1} d_\mathrm{h}^{-1}$. Diese Abhängigkeit wurde in unterschiedlichen Filterstrukturen experimentell und simulativ validiert und kann somit als Designrichtlinie für DEP Filtrationsanwendungen verwendet werden. Darüber hinaus wurde der Einfluss der Filterporengeometrie anhand von unterschiedlichen Filtern untersucht. Es zeigte sich, dass geschäumte Filterstrukturen deutlich höhere DEP Abtrenneffizienzen erzielen konnten als Filterstrukturen bestehend aus Glaskugelschüttungen. Die wesentliche Ursache dafür ist, dass die Partikel in geschäumten Strukturen scharfe Kanaleinschnürungen durchqueren müssen, an denen $\nabla|\mathbf{E}|^2$ und infolgedessen die dielektrophoretische Kraft groß sind. In Kugelschüttungen gibt es diese scharfen Einschnürungen nicht, wodurch die DEP Kräfte zur Partikelabtrennung geringer sind.

Außerdem, wurden die Möglichkeiten selektiver Partikeltrennung durch DEP Filtration untersucht. Es wurde festgestellt, dass die Abtrenneffizienz in DEP Filtrationsprozessen durch Einstellung der Polarisierbarkeit des fluiden Mediums im Vergleich zur Polarisierbarkeit der Partikel gesteuert werden kann. Dieser Effekt wurde erstmals experimentell untersucht und erfolgreich zur Trennung von Partikeln unterschiedlicher Polarisierbarkeit eingesetzt. Die dabei erreichten Durchsätze liegen im Vergleich zu anderen selektiven, DEP-basierte Trennanwendungen (die fast ausschließlich im Bereich $< \mu\mathrm{L\,min}^{-1}$ liegen) in einem hohen Bereich und können durch Vergrößerung der Filterfläche gut auf industrielle Maßstäbe gesteigert werden.

Die in dieser Arbeit vorgestellten Ergebnisse liefern grundlegendes Verständnis über DEP Filtration. Diese stellen einen wesentlichen Schritt zur Lösung aktuell ungelöster Trennprobleme, wie zum Beispiel der Aufkonzentrierung und der Rückgewinnung wertvoller Partikel aus gemischten Suspensionen, dar. Da der Durchsatz durch Vergrößerung der Filterquerschnittsfläche einfach erhöht werden kann, erscheinen Anwendungen von industriellem Maßstab möglich.

Abstract

Separation of micron and sub-micron particles from liquids and from each other according to their properties is a challenging but essential task for applications in many industrial fields. Despite the variety of existing particle separation techniques, many separation tasks remain unsolved and new separation techniques are required to solve them.

Dielectrophoresis (DEP) describes the motion of polarizable particles in inhomogeneous electric fields. It can be used for highly selective particle separation according to their size, material, and morphology, without changing the particle properties. Most DEP-based particle separation techniques use microfluidic channels that are unsuited to process industrial-scale throughputs. The reason for this is that the DEP force scales with the gradient of the squared electric field, $\nabla|\mathbf{E}|^2$. The unit of this gradient is $\mathrm{V^2\,m^{-3}}$, showing that high electric voltages and small structures are required for high gradients. $\nabla|\mathbf{E}|^2$ is high at interfaces of materials with different dielectric properties, but quickly decreases with increasing distance from these interfaces. An alternative approach that can potentially solve the throughput limitation is a technique called DEP filtration. This technique uses open-porous filters that provide numerous tortuous flow paths, which are suited for high throughputs. The electric field is distorted at the filter surface so that high electric field gradients are generated providing good conditions for DEP particle retention. The few existing studies on DEP filtration solve very specific separation tasks but are not suited to understand the basic physical phenomena of DEP filtration. However, such understanding is required to improve the technique and develop new applications.

This work investigates DEP filtration in a comprehensive experimental study to gain fundamental understanding. In a first step, a DEP filtration setup to conduct experiments was conceptualized and built. In the developed filter cell, almost 100% particle separation efficiency was achieved using 500 nm polystyrene particles and throughputs of $9\,\mathrm{mL\,min^{-1}}$ (filter cross section: $2\,\mathrm{cm^2}$). In a parametric study, the dependency of the separation efficiency on the applied voltage (ΔU), volumetric throughput (Q), and hydraulic pore diameter (d_h) was investigated. The separation efficiency can be described as a function of a single variable $\bar{x} = (\Delta U)^2 Q^{-1} d_\mathrm{h}^{-1}$. This dependence was validated for different filter structures in experiments and simulations. It can be regarded as a design guideline for

DEP filtration applications. Another topic was to investigate the influence of the filter pore geometry. It was shown that separation efficiency in foamed filter structures was significantly higher than in packed beds of glass beads. The reason is that in a foamed structures, particles have to penetrate many sharp channel constrictions, at which $\nabla|\mathbf{E}|^2$ and consequently the DEP force is high. In packed beds of glass beads, these sharp constrictions are missing and hence DEP forces are much smaller.

Furthermore, the possibilities of selective particle separation by DEP filtration were investigated. It was shown that the separation efficiency of DEP filtration processes can be controlled by adjusting the fluids polarizability with respect to the particle polarizability. This effect was studied for the first time experimentally and was successfully applied for separation of particles with different polarizability.

The results, presented in this work, provide a fundamental understanding of DEP filtration. They are an essential step to solve currently unsolved separation problems, such as, purification and recovery of valuable particles from mixed suspensions. Since throughput can be raised by simply increasing the filter cross section, applications on industrial-scale should be possible.

Acknowledgement

This work has been developed at the Center for Environmental Research and Sustainable Technology at the University of Bremen in the framework of the research training group (GRK 1860) “Micro-, meso- and macroporous nonmetallic Materials: Fundamentals and Applications” (MIMENIMA) that was funded by the German Research Association (DFG).

I thank Prof. Dr.-Ing. Jorg Thöming, not only for supervising my work and revising my thesis, but for his unlimited support, motivating conversations, and his sometimes required patience throughout this work.

I thank Prof. Dr.-Ing. Sergiy Antonyuk for his spontaneous acceptance to be second reviewer of my thesis and for his time to read and review it.

I thank my supervisor Michael Baune for his ideas, his confidence in my abilities, his positive and truly interested presence, and his cabinet of useful and useless things.

I thank my colleague, part-time office mate, and supervisor Georg Pesch for his advice and collaboration, his patience to let me find my own way of science, his appreciation of my work, and of course for the time we spent together in the office, labs, and bars (albeit he apparently thinks he has that green thumb).

I thank Fei Du for sharing his perspective on my scientific work and his motivating ideas on how to continue.

I would like to thank Arne-Brün Vogelsang for his comprehensive work in the lab that was a great support. I would like to thank all my colleagues from the working group of Chemical Process Engineering for countless discussions and making it a good time (!) and my family and friends for being around.

I thank Valentin Baric, Philipp Bruck, and Chiara Vanni for proofreading this thesis so carefully.

List of Publications

G. R. Pesch, M. Lorenz, S. Sachdev, S. Salameh, F. Du, M. Baune, P. E. Boukany, and J. Thöming (2018). Bridging the scales in high-throughput dielectrophoretic (bio-)particle separation in porous media. *Scientific Reports*, 8:10480. doi: 10.1038/s41598-018-28735-w
GRP, ML, FD, MB, and JT conceived the experiments. GRP and ML conducted the experiments. GRP, FD, SaS, ShS, MB, PEB, and JT analyzed the results. GRP wrote the manuscript with input from all other authors. GRP and ML contributed equally to this work.

L. Weirauch, M. Lorenz, N. Hill, B. H. Lapizco-Encinas, M. Baune, G. R. Pesch, and J. Thöming (2019). Material-selective separation of mixed microparticles via insulator-based dielectrophoresis. *Biomicrofluidics*, 13, 064112. doi: 10.1063/1.5124110
LW, ML, GRP, and JT conceived the experiments. LW and ML conducted the experiments. LW, ML, BHL, MB, GRP, and JT analyzed the results. GP MB, and JT supervised the project. LW, ML wrote the manuscript with input from all other authors. LW and ML contributed equally to this work.

M. Lorenz, D. Malangré, F. Du, M. Baune, J. Thöming, and G. R. Pesch (2020). High-throughput dielectrophoretic filtration of sub-micron and micro particles in macroscopic porous materials. *Analytical and Bioanalytical Chemistry*, 412, 3903-3914. doi: 10.1007/s00216-020-02557-0
ML, GRP, FD, MB, and JT conceived the experiments. ML conducted the experiments. DM provided the porous ceramic samples. ML, GRP, FD, MB, and JT analyzed the results. GP and MB supervised the project. ML wrote the manuscript with input from all other authors.

M. Lorenz, A. P. Weber, M. Baune, J. Thöming, and G. R. Pesch (2020). Aerosol classification by dielectrophoresis: a theoretical study on spherical particles. *Scientific Reports*, 10:10617. doi: 10.1038/s41598-020-67628-9
JT and GRP conceived of the idea. ML created the model and performed the calculations under supervision of MB, JT, and GRP. All authors discussed the results. ML and GRP wrote the manuscript with input from all other authors.

Contents

Chapter 1

Introduction

Separation of micron and sub-micron particles from liquids according to their properties is essential for many fields. It is key for industrial processes, where particle separation is used for product purification, for recovery and mining of valuable materials and to increase sustainability and cost efficiency. Currently available separation processes such as deep bed filtration, membrane filtration, centrifugation (for industrial scale throughputs), and chromatography (for analytical scale throughputs) can solve some of these separation tasks but have limitations especially for micron and sub-micron particles. For these small particle scales, size exclusion mechanisms require high pressure differences to achieve significant throughputs and density separation fails as the weight differences become negligible in comparison to other forces. The lack of efficient physical separation techniques to separate micron and sub-micron particles with difficult properties is problematic (Peukert and Wadenpohl, 2001, Ermolin and Fedotov, 2016). New separation techniques are required to solve these separation tasks.

An example to illustrate this problem is the recovery of precious materials from electronic waste. In an initial step, the electronic waste is shredded down to small pieces so that standard physical separation processes for material recovery can be applied. These processes can separate particles according, for instance, their density or magnetism. However, a byproduct of the milling is a fine dust that contains a substantial part of noble metals (10% to 35% of the total amount of noble metals). This significant fraction of noble metals is currently lost because available separation techniques are inefficient (Tuncuk et al., 2012). A separation technique to recover these valuable particles from the dust would allow mining otherwise lost materials from electronic waste.

Dielectrophoresis (DEP) is an electrokinetic effect that can be utilized for micron and sub-micron particle separation. It has shown to be highly selective on particle properties size, shape, and material. Although DEP was early on applied for separation of non-biological particles at throughputs of industrial scale (Fritsche and Haniak, 1975), today it

has developed into a technique that is mainly used for bio applications in microchannels of analytical throughput and selectivity. This development makes sense because dielectrophoretic motion is driven by the gradient of the electric field squared that has the unit $V^2\,m^{-3}$. It requires high voltages and small structure sizes which are easily produced in microchannels.

While analytical separation processes favor selectivity over throughput, this priority changes for industrial separation processes. These require sufficiently high throughputs to be profitable, which cannot be achieved in expensively produced microchannels. In order to increase the throughput, this thesis suggests to use particle retention in inhomogeneous open porous filters, a technique called DEP filtration. The inhomogeneous porous filters can contain numerous tortuous flow paths in parallel, each similar to a microchannel. As they are also cheap to produce, they provide excellent conditions for increased throughput. The principle of DEP filtration is remarkably simple. Two electrodes are used to apply an alternating current (ac) electric field across the filter. The electric field is distorted at the surface of the inhomogeneous filter structure. This produces high electric field gradients in the filter which are suited for dielectrophoretic particle retention. If the filter pores are significantly larger than the suspended particles, depth filtration mechanisms are negligible and particle recovery is possible by switching off the electric field. In contrast to other filtration techniques that base on size exclusion DEP filtration is therefore unsusceptible to filter clogging.

Despite its properties, there are only a few studies about DEP filtration (Sec. 4.3). Most of them solve specific separation problems but do not provide an in-depth understanding of the technique. The working group at the University of Bremen (Pesch et al.) was the first that aimed for general design rules for DEP filtration. They started with a theoretical investigation of DEP filtration in simplified 2-dimensional models of porous filter structures. In simulations, they predicted how DEP particle retention scales with essential process parameters such as electric field strength, filter post geometry, particle size, and particle velocity (Pesch et al., 2016, 2017, 2018). Ironically, they validated these scaling laws with experiments in microchannels because the microchannels allowed easy fabrication of the model porous structures. They found good agreement between predictions and experiments. However, experimental studies that investigate the fundamental mechanisms and possibilities of DEP filtration in real (inhomogeneous) porous filter structures are still missing.

This thesis aims to close this scientific gap and put DEP filtration into practice. The fundamentals about DEP, related electrokinetic effects, DEP-based separation techniques, and depth filtration are presented in Chapter 2 and Chapter 3. Chapter 4 presents the concept and the state-of-the-art of DEP filtration together with the aims and the approach

of this thesis. Applied materials and methods are presented in Chapter 5. The results of investigations are shown in Chapters 6–8. Chapter 6 gives a theoretical evaluation of the fluid flow, particle motion, and particle trapping in the filter, based on simulations. It describes how DEP filtration is predicted to work in 3-dimensional filter structures. Chapter 7 focuses on an experimental study of DEP filtration. The influence of essential parameters, like volumetric throughput, applied electric field strength, filter pore size, and pore geometry, which can be used to control the separation process will be determined. Further, this chapter studies the capacity of the filter and the possibility to recover particles from the filter once they have been retained. Chapter 8 focuses on how DEP filtration can be applied. This chapter works towards selective separation of particles according to their electric conductivities. The possibilities of selective separation is investigated by using binary particle suspensions in form of latex-graphite particle suspensions and latex-copper particle suspensions. This chapter further studies how filter geometry and material can be redesigned to reduce mechanical trapping effects caused by sedimentation and adhesion in the filter. These aspects are also essential for particle recovery from the filter. Conclusion and outlook are given in Chapter 9.

Chapter 2

Theory: From electric force to dielectrophoresis

The word electric derives from the Greek word amber, since it was found that when amber is rubbed it attracts small things like chaff. There have been quite different theories about this peculiar phenomenon that were often contradictory. Electrical phenomena of all sorts (like for example lightnings, electric fish referred to as “thunder of the Nile” (Moller, 1991)) have been studied since antiquity. However it took until the seventeenth and eighteenth century until the theory about electricity that is known today was developed and until the nineteenth century that it was put to use. Since then the understanding of electrical phenomena and technology has developed rapidly and transformed industry and society. Today electric charge is seen as part of every material and matter starting at a subatomic scale. The electric force that acts between charges is accounted as one of the four fundamental forces that all phenomena derive from.

This chapter gives an overview of essential parts of electromagnetic theory. It starts from the fundamentals of electric charge on a subatomic scale progresses with electric fields, dielectrics, and polarization to give the basis for dielectrophoresis and related effects. This section will end with a brief overview of dielectrophoretic particle separation.

2.1 Electric force and electric field

In 1600 William Gilbert showed in experiments that not only amber but many materials produced and “electric force” like amber when suitable prepared. It took about 150 years more until Benjamin Franklin postulated that rubbing transfers a tangible electric “fluid” from one body to another leaving one with a surplus and the other with a deficit. He recommended that these two kinds of electrification should be called *positive* and *negative* leading to the terms positive and negative charge. It was found that charges of opposite

type attract and charges of the same type repel each other. Around 1785 Charles-Augustin de Coulomb used the torsion balance (that was independently developed by John Michel) to verify that the force between two stationary point charges Q_1 and Q_2 is proportional to their product and the inverse of the square of their distance:

$$\mathbf{F} = \frac{Q_1 Q_2}{4\pi\varepsilon_0 x^2}\hat{\mathbf{x}}_{12}\,. \tag{2.1}$$

This was later called Coulomb's law. x is the distance between Q_1 to Q_2, $\hat{\mathbf{x}}_{12}$ is the unit vector that points from Q_1 to Q_2, and ε_0 is the permittivity of vacuum (free space) that has the value $8.854 \times 10^{-12}\,\mathrm{Fm}^{-1}$. When two or more point charges act on a charge, the resulting force on it is the vector sum of each individual force exerted by the other charges (principle of superposition).

The electric field $\boldsymbol{E}$ at a point in space is defined as the electric force that acts on a unit (1 Coulomb (C)) test charge (at that point). The electric field that is generated by a point charge Q_1 is thus after the Coulomb's law,

$$\mathbf{E} = \frac{Q_1}{4\pi\varepsilon_0 x^2}\hat{\mathbf{x}}\,. \tag{2.2}$$

The direction of the electric field (the direction of the electric force) is provided by the unit vector $\hat{\mathbf{x}}$. By convention $\hat{\mathbf{x}}$ points along the electric field lines (Chapter 2.2) from positive to negative charge. Two simple cases of electric fields are shown in Fig. 2.1. The lines of iso-potential are shown in blue (lines) the electric field lines as black arrows.

In analogy to the electric force, the electric field follows the *principle of superposition*. The electric field at an arbitrary point $\mathbf{x}$ can thus be calculated by the electric field vector sum of all present charges. Introducing the volumetric charge density ρ, that describes the spatial charge distribution, the electric field vector $\mathbf{E}$ can be expressed by the volume integral of ρ,

$$\mathbf{E}(\mathbf{x}) = \frac{1}{4\pi\varepsilon_0}\int_V \rho(\mathbf{x}')\frac{\mathbf{x}-\mathbf{x}'}{|\mathbf{x}-\mathbf{x}'|^3}\mathrm{d}^3\mathbf{x}'\,. \tag{2.3}$$

2.2 Electric potential and electric energy

Energy is never lost but can only convert to another form and/or transferred to another system. A common example is the energy of a pendulum. To let a pendulum swing work (energy) is required to lift the weight and thus increasing its potential energy. In order to reduce its potential energy (all systems try to attain an equilibrium state by minimizing its potential energy) the pendulum is swinging down and the potential energy is converted

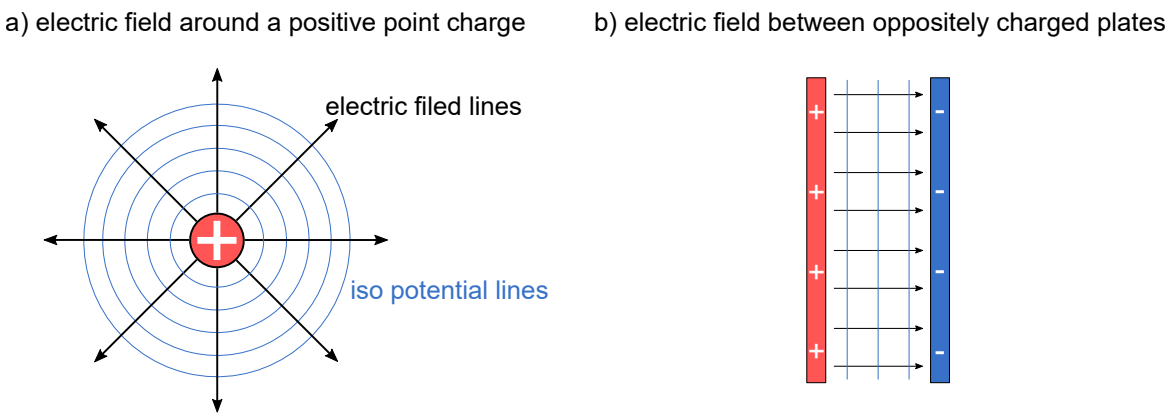

Figure 2.1: Electric fields around a positive point charge (a) and between two oppositely charged plates (b). The electric field lines are shown as black arrows, the iso potential lines as blue lines.

to kinetic energy. At the lowest point all potential energy is transferred to kinetic energy and reconversion to potential energy starts. If no frictional forces were exerted onto the pendulum this process would never end since no energy would leave the system of the pendulum.

Similar to the work that is needed to move a mass against the gravitational field, work is needed to move a positive charge against or a negative charge along the direction of an electric field line. It increases the potential work that can be recovered by moving the electric charge back to the equilibrium state. For further understanding, the more work is put into concentrating charges of the same kind, the higher is the electric potential in the system. Eventually, the system aims to reach equilibrium state which is a homogeneous distribution of positive and negative charges. The energy $W_{\mathrm{a,b}}$ that we give into the system by moving a charge Q from point **a** to point **b** in an electric field is written as,

$$W_{\mathrm{a,b}} = \int_{\mathbf{a}}^{\mathbf{b}} Q\mathbf{E}\mathrm{d}\mathbf{l} = Q(\Phi(\mathbf{b}) - \Phi(\mathbf{a})) = W_{\mathrm{b}} - W_{\mathrm{a}}\Delta W \ . \tag{2.4}$$

The difference in electric potential energy ΔW is independent of the path **l** that the charge is moved along. It just depends the charge Q and **a** and **b** and their respective electric potentials, $\Phi(\mathbf{a})$ and $\Phi(\mathbf{b})$. Dividing Eq. (2.4) by the amount of charge Q, gives the electric potential difference between **a** and **b**,

$$\int_{\mathbf{a}}^{\mathbf{b}} \mathbf{E}\mathrm{d}\mathbf{l} = \Phi(\mathbf{b}) - \Phi(\mathbf{a}) = \Delta\Phi \ . \tag{2.5}$$

In analogy to a mechanical system the iso-potential lines would be represented as lines of equal height that embrace the mountain and the whole. The path perpendicular to the iso-potential lines are the electric field lines. A simple form to describe electric potential Φ

and electric field is given by

$$\mathbf{E} = -\nabla\Phi, \tag{2.6}$$

with the del operator ∇. The unit of the electric potential is volts V and is equivalent to the work that can be done per amount of charge (V=JC^{-1}). Another and in many cases more convenient description of the electric field is given by Gauss' law. His formulation determines that the total flux of $\mathbf{E}$ (amount of electric field lines) through a closed surface equals the charge inside (the by the surface enclosed volume). The charge inside the volume is the volume integral of ρ so that Gauss' law reads

$$\nabla \cdot \mathbf{E} = \frac{\rho}{\varepsilon_0}\,. \tag{2.7}$$

Substituting for the electric potential according to Eq. (2.6) yields the Poisson equation

$$\nabla^2\Phi = -\frac{\rho}{\varepsilon_0}\,. \tag{2.8}$$

The equations of this chapter are sufficient to describe the electric potential and field for an arbitrary charge configuration in perfect vacuum. However, in most situations we are not confronted with electrostatics in perfect vacuum. The following section will thus go on with electrostatic problems in volumes containing materials which interact with the electric field – dielectrics.

2.3 Electric fields through dielectric media

Although most fluids and solids are uncharged or neutral, they contain charges that interact with an electric field. It is distinguished between two types of charges.

> *Free charges* are excess charges that are not bound to other charges. Their movement is determined by the conductivity of the medium they are in. Charge conduction takes place by transfer of electrons as it is the case in metals, semi conductors, or plasma or by ion transfer as it is taking place in ionic liquids (e. g. salt water) and by charged particles. While charges can move rather freely in electrically conducting media, electrically isolating materials do not allow charges to move at all.
>
> The second type of charges is called *bound charges*. They appear in pairs of same magnitude but opposite sign and their mobility is restricted to short distances between each other. Bound charges react to an electric field by polarization and store a capacity of electrical energy comparable to a spring that absorbs mechanical energy.

The following sections will describe the behavior of bound charges in an electric field, start-

ing at the fundamental effects that appear on atomic and molecular level and transferring them onto whole materials in which numerous of these effects sum up.

2.3.1 Introducing dipoles

The simplest form of polarization is a *dipole*. A dipole consists of two coupled point charges of the same magnitude Q but opposite sign (Fig. 2.2). The model of a dipole can be used as a simplified but exact model to describe more complex distributions of coupled charges. It can be used to describe polarization of single atoms, molecules, materials, and whole particles. A dipole is characterized by its so called dipole moment that describes strength and direction of a dipole. It is defined as the product of charge Q and the vector between the charges $\mathbf{a}$

$$\mathbf{p} = Q\mathbf{a}\,. \tag{2.9}$$

In a homogeneous electric field the force on both charges is the same but to opposite

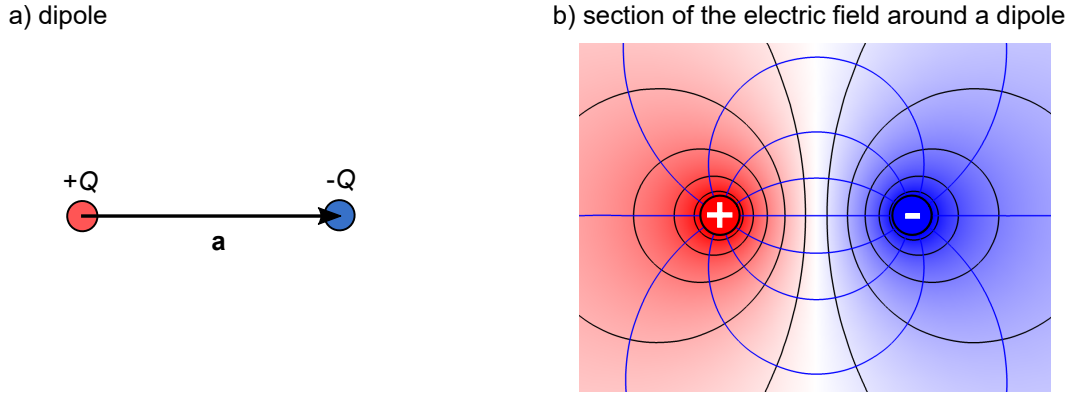

Figure 2.2: Dipole with the vector $\mathbf{a}$ that point from positive to negative charge (a). (b) section of the electric field generated by the dipole. Electric field lines are shown as blue lines, lines of iso potential as black lines.

directions so that the total force exerted on the dipole is zero. However, a dipole experiences a torque $\mathbf{\Gamma}$ when it is not aligned with the electric field:

$$\mathbf{\Gamma} = \mathbf{p} \times \mathbf{E}\,. \tag{2.10}$$

In non-uniform electric fields, where the change in electric field magnitude is described by its gradient $\nabla\mathbf{E}$, the electric force on both dipole charges differs. The force on a dipole in an electric field is given by

$$\mathbf{F} = (\mathbf{p} \cdot \nabla)\mathbf{E}\,. \tag{2.11}$$

It is the basic equation for the dielectrophoretic force that will be described in Sec. 2.5.

2.3.2 Fundamental polarization mechanisms

There are three different polarization mechanisms on atomic and molecular level that are described here to emphasize their different nature.

i) *Electronic polarization.* Electronic polarization around an atom is polarization at the smallest scale. The smallest unit of electric charge that we know is equivalent to the charge of an electron $q_e = 1.602 \times 10^{-19}$ C. All particles possess an integer multiple of it (Zangwill, 2012). An atom consists of at least two charges of opposite sign, a positive charge in form of a proton at the center/nucleus of the atom and a negative charge in form of an electron that surrounds the nucleus in an orbit. To the outside an atom in its normal state appears neutral (without charge) because both charges have the same center and compensate each other. However, when placed in an electric field the positive nucleus and the negative electron orbit experience electric forces to opposite directions. These lead to a relative displacement of their centers to each other. The atom is electrically polarized and appears to the outside as a dipole. The electronic polarizability of an hydrogen atom is $\alpha_e = 1.6 \times 10^{-41}\mathrm{Fm}^2$.

ii) *Orientational polarization.* A polarization mechanism that takes place on a slightly bigger scale is orientational polarization. Many molecules contain permanent dipoles. A commonly known examples is water consisting of two hydrogen atoms and one oxygen atom. Oxygen as a high electronegativity (tendency to attract a shared pair of electrons towards itself) and attracts the electrons of the two hydrogen atoms. The resulting charge displacement leads to a dipole ($1.84\,\mathrm{Debye} = 6.14 \times 10^{-30}\,\mathrm{Fm}^2$) with the negative side towards the oxygen atom. Permanent dipoles around a molecule are usually stronger than dipoles around atoms.

iii) *Atomic polarization.* The third and last fundamental polarization mechanism occurs in crystalline materials. Crystalline materials contain ions. Positive and negative ions are connected via ionic bindings. In an electric field the differently charged ions shift to opposite direction causing atomic polarization.

Atoms and molecules in an electric field are polarized by at least one of these polarization mechanisms. The dipole that is generated in them can be described by their polarizability α and the local electric field around them $\mathbf{E}'$

$$\mathbf{p}_{av} = \alpha \mathbf{E}' \,. \tag{2.12}$$

Assuming that electric (α_e), orientational (α_{or}), and atomic (α_a) polarizability are independent of each other the total polarizability of atoms and molecules calculates as the sum of

them, $\alpha = \alpha_e + \alpha_{or} + \alpha_a$. While the polarizability α describes the dipole of single atoms and molecules they further provide the basis to derive the polarization of charge containing materials.

2.3.3 Ideal dielectrics

An *ideal* dielectric media is by definition polarizable but not conductive and thus contains only bound charges that are polarizable but no free charges. The sum of charge displacement of n molecules leads to a volume specific polarization $\mathbf{P}$ of,

$$\mathbf{P} = \alpha n \mathbf{E}' \tag{2.13}$$

that represents the induced electric field due to dipoles in the material. The density of all bound charges ρ_b gives the negative gradient of the polarization

$$\rho_b = -\nabla \cdot \mathbf{P} \,. \tag{2.14}$$

For dielectrics that are linear and isotropic (which is a sufficient approximation for most homogeneous and non-ferrous media) electric field and polarization are related by

$$\mathbf{P} = \varepsilon_0 \chi_{ae} \mathbf{E} \,, \tag{2.15}$$

with the *electric susceptibility* χ_{ae} of the dielectric. From Gauss' law (2.7) and with the total charge density being the sum of bound and free charges, $\rho = \rho_b + \rho_f$ it follows

$$\nabla \cdot (\varepsilon_0 \mathbf{E} + \mathbf{P}) = \rho_f \,. \tag{2.16}$$

A third vector field the *electric flux* (displacement field) $\mathbf{D}$ was defined by Maxwell

$$\mathbf{D} = \varepsilon_0 \mathbf{E} + \mathbf{P} \,. \tag{2.17}$$

$\mathbf{D}$ is useful tool to visualize how an electric field behaves in dielectric media. For an ideal dielectric (linear, isotropic, and not conductive) $\mathbf{P}$ can be substituted according to (2.15) to obtain

$$\mathbf{D} = \varepsilon_0 (1 + \chi_{ae}) \mathbf{E} \,. \tag{2.18}$$

The dimensionless factor $(1 + \chi_{ae})$ is material dependent and is defined as the *relative permittivity* ε_r so that the electric flux writes as

$$\mathbf{D} = \varepsilon_0 \varepsilon_r \mathbf{E} \,. \tag{2.19}$$

The electric field lines through a homogeneous ideal dielectric medium have thus the same

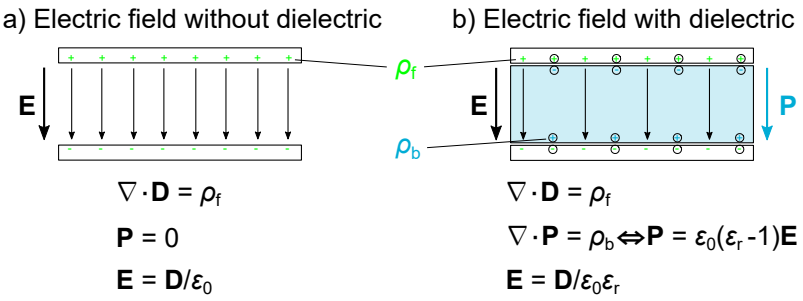

Figure 2.3: Electric field generated in a capacitor consisting of two plate electrodes without (a) and with a dielectric (b) between the electrodes. The charge density is schematically shown by + and -. Green marks the free charges and blue the bound charges. Neutralized charges (pairs of + and -) are framed by circles.

shape as in vacuum, but the effective electric potential decreases by factor ε_r. By defining $\mathbf{P}$ and $\mathbf{D}$ and their connections to ρ_b and ρ_f we have now a tool to describe the electric field $\mathbf{E}$ as the sum of both. While electric flux field $\mathbf{D}$ correlates with the electric field caused by free charges, the effective electric field is reduced due to the counteracting polarization field $\mathbf{P}$. The electric field magnitude decreases by the factor ε_r^{-1} when the electric field is penetrating a dielectric medium instead of a vacuum. At the same time the capacity of the electric field increases by factor ε_r so that the potential energy of the electric field

$$\mathbf{W} = \frac{1}{2}\int_V \rho(\mathbf{x})\Phi(\mathbf{x})\mathrm{d}^3\mathbf{x}\,, \tag{2.20}$$

remains unchanged. Besides having a capacity to store electric energy, dielectrics that are inhomogeneous influence the path that electric field lines take. A dielectric with high susceptibility (high permittivity) is from an energetic point easier to penetrate as than a dielectric with lower susceptibility. This is the reason why particles of higher permittivity than the surrounding medium attract electric field lines. If the particle has a lower permittivity than the surrounding medium electric field lines are repelled. This phenomena will be described later in further detail when turning towards particle polarization.

2.3.4 Dielectric relaxation, dispersion

Displacement of charge is not instant but charges need time to react to an electric field. Polarization is therefore a function of time. How quick an electric field changes is often discribed by the field frequency ω. At sufficiently high electric field frequencies charges cannot react to the electric field changes. At these frequencies the permittivity of all materials is equal to the permittivity of free space ε_0 because no polarization is taking place. Electronic and atomic polarization can follow the highest frequencies because their

charge displacement is of short range. They follow field frequencies up to about 10^{13} Hz (Pethig, 2017a). Orientational polarization of molecules can react to frequencies up to $10^7 - 10^8$ Hz to fully align all permanent dipoles of the molecules against the randomizing force of Brownian motion. The reaction time is dependent on the size of the molecules and viscosity of the media the molecules are solved in.

The different reaction times of polarization mechanisms to an electric field leads to a frequency dependent polarization. If the frequency is low enough to allow electronic and atomic polarization, polarization $\mathbf{P}$ can be expressed as the sum of a frequency independent part $\mathbf{P}_{\mathrm{e,a}}$ and a frequency (ω) dependent part $\mathbf{P}_{\mathrm{or}}(\omega)$. In a simple case, when orientational polarization is caused by just one type of molecule, polarization can be written as (Pethig, 2017a)

$$\mathbf{P}(\omega) = \mathbf{P}_{\mathrm{e,a}} + \mathbf{P}_{\mathrm{or}}(\omega) = \left[(\varepsilon_{\mathrm{e,a}} - 1) + \frac{\varepsilon_{\mathrm{or}} - 1}{1 + i\omega\tau_{\mathrm{or}}} \right] \varepsilon_0 \mathbf{E}. \tag{2.21}$$

with the imaginary number $i^2 = -1$ and $\varepsilon_{\mathrm{a,e}}$ and $\varepsilon_{\mathrm{or}}$ the relative permittivities at too high and sufficiently low frequency so that the accounted polarization mechanism can fully build. The relaxation time of the polarization mechanism is represented by τ_{or}. This can be translated into a frequency dependent relative permittivity of

$$\varepsilon_{\mathrm{r}}(\omega) = \varepsilon_{\mathrm{e,a}} + \frac{\varepsilon_{\mathrm{or}} - \varepsilon_{\mathrm{e,a}}}{1 + i\omega\tau_{\mathrm{or}}}. \tag{2.22}$$

Depending on the number of different polarization effects Eqns. (2.21) and (2.22) are extended by more terms that become relevant at different relaxation times τ.

Separating the real and the imaginary part of Eq. (2.22) in the form $\varepsilon_{\mathrm{r}} = \varepsilon_0(\varepsilon' - i\varepsilon'')$ and replacing $\varepsilon_{\mathrm{a,e}}$ and $\varepsilon_{\mathrm{or}}$ by more general forms of a high frequency permittivity ε_∞ and a low frequency permittivity ε_{s} leads to the Debye relations.

$$\begin{aligned} \varepsilon' &= \varepsilon_\infty + \frac{\varepsilon_{\mathrm{s}} - \varepsilon_\infty}{1 + \omega^2\tau^2}, \\ \varepsilon'' &= \frac{(\varepsilon_{\mathrm{s}} - \varepsilon_\infty)\omega\tau}{1 + \omega^2\tau^2}. \end{aligned} \tag{2.23}$$

While the real part ε' describes the capacity to polarize, the imaginary part ε'' represents the energy dissipation which means a transfer of electrical to thermal energy. If ε'' is zero, there is no phase lag between $\mathbf{D}$ and $\mathbf{E}$. The energy induced into the material is saved by polarization during the first half-cycle of the field. It is given back to the driving electric source in the second half-cycle. This is the case at low frequencies where $\omega << \tau^{-1}$. The maximum dissipation is taking place at $\omega = \tau^{-1}$. At frequencies above τ^{-1} dissipation decreases again due to insufficient time for polarization.

2.3.5 Conduction and conducting media

While an *ideal* dielectric medium possess only bound charges and a capacity to store electrical energy by polarization it does not conduct charge. An *ideal* conductor possess only free charges that do not store energy by polarization but move freely in reaction to an electric field. In order to minimize their potential energy and reach equilibrium state the free charges in an ideal conductor will move until they experience no electric force anymore or an electric force that is perpendicular to the conductors surface. This is only the case when the electric field generated by the charge shift neutralizes the applied electric field. Therefore no effective electric field can exist inside an ideal conductor, $\mathbf{E}_{\mathrm{ic}} = 0$. To satisfy this, the induced bound charge density at the surface of an conductor must match the free charge density of the electric field. There is no tangential electric field component at a conducting surface. After Gauss' law this leads to the following correlations about the surface-normal component of the electric field outside E_{no} and inside E_{ni} of the conductor

$$\begin{aligned} E_{\mathrm{no}} &= \frac{\rho_{\mathrm{s,f}}}{\varepsilon_0}, \\ E_{\mathrm{ni}} &= 0. \end{aligned} \tag{2.24}$$

Here, $\rho_{\mathrm{s,f}}$ is the surface specific free charge density ($\mathrm{C\,m^{-2}}$) generated by the external electric field. A finite conductive material that is surrounded by a not conductive medium experiences polarization. Although conductors do not possess bound charges, charges cannot leave the material since they are bound to the bulk material of the conductor to keep the total charge at zero.

The ideal conductor is a theoretical model. Only in theory charge can move without loss through an ideal conductor of infinite conductivity σ. Real charge conduction leads always to some amount of dissipation. When charges move through another medium they are scattered by collisions with other charges which results in a partial conversion into undirected oscillation of atoms and molecules, defined as thermal energy. Even metallic conductors, that are highly conductive, because a relatively large amount of their electrons are freely moving in a cloud of electrons that penetrate through the whole metal, are not infinitely conductive. Electrons lose some of their energy because their motion along the electric field lines is disturbed by collisions with the materials lattice. The effect is called Joule heating and the volume specific thermal energy generated by an electric field per second (unit: $\mathrm{W\,m^{-3}}$) is described by

$$q_{\mathrm{th}} = \sigma |\mathbf{E}|^2 . \tag{2.25}$$

2.3.6 Non-ideal dielectrics

While some dielectrics are well described by an ideal dielelectric ($\varepsilon \neq 0$, $\sigma = 0$) and some others by ideal conductors ($\sigma = \text{inf}$), many materials combine their properties and possess an electric permittivity and a finite electric conductivity. These effects can be considered by ascribing the materials permittivity as a *complex* permittivity

$$\tilde{\varepsilon} = \varepsilon_0 \varepsilon_\text{r} - i\frac{\sigma}{\omega}, \tag{2.26}$$

with the electric conductivity of the dielectric medium σ, and the angular frequency of the electric field ω. The derivation of the complex permittivity can be found e.g. in Morgan and Green (2003). The term on the right hand side of (2.26) shows that the $\tilde{\varepsilon}$ is conductivity- and ω-dependent. Dielectrophoresis uses the frequency-dependence of the complex permittivity to separate particles of different dielectric materials. Above (Sec. 2.3.4) we described the effects of dielectric relaxation and how ε_r becomes a function of ω at high frequencies. However, in this thesis frequencies below 10^5 Hz were used where ε_r is constant but particle polarization is dependent on another mechanism – interfacial polarization.

2.3.7 Heterogeneous materials and interfacial polarization

Real systems are often heterogeneous and consist of many dielectrics so that interfaces between homogeneous dielectrics become important. On interfaces charges experience electric forces different from those in a uniform bulk material. While in the bulk electric forces are usually balanced, at interfaces charges experience electric forces of the different materials that are usually different in strength. These charges are shifted to either the inside or outside of the surface. Therefore, most interfaces appear charged.

In an electric field charges on a material interface react to the electric field. Since the charges are bound to the material this leads to another form of polarization called *interfacial* polarization. At low frequencies interfacial polarization is usually the strongest polarization mechanism for low conductive particles. This is because charge displacement takes place along the full size of the particle and not just at atomic and molecular scale.

2.3.8 Interfaces with aqueous electrolytes – the electric double layer model

Most DEP applications are done with aqueous suspensions so that it is particularly important describe charge at interfaces between solid materials and water. Interfaces with water are influenced by ions that are solved in water. A schematic of a particle that is

overall uncharged but possesses a negative surface charge suspended in a solvent that contains ions is shown in Fig. 2.4. The illustration is after the Gouy-Chapman-Stern model. Positive ions (red circles) of the suspension are attracted by the negative surface charge and form the so called Stern layer that sits tightly at the surface. This compact layer may also contain specific ions that were absorbed to the surface before and are not constituent of the suspension (Bazant et al., 2004). In the diffusive layer charges are still mainly positive but charges can slightly move due to diffusion. The Stern layer and the diffusive layer form an electric double layer (DL) that accounts for the atmosphere of ions around the particle. The outside boarder of the diffusive layer is the slipping plane where molecules are considered to be able to move freely by convection. It acts as border to the bulk suspension. The potential at the slipping plane is the zeta (ζ) potential which is in addition to the double layer thickness the only measurable size to characterize the dielectric double layer. In a suspension of equal positive and negative ion concentrations (pH=7) the potential far from the particle falls to zero. The double layer thickness was introduced by Debye and is thus also called Debye length $\lambda_D = \kappa^{-1}$. For spherical particles in an electrolyte solution the Debye length is given by (Morgan and Green, 2003)

$$\lambda_D = \kappa^{-1} = \sqrt{\frac{\varepsilon k_B T}{2 z^2 e^2 c_m}} \tag{2.27}$$

with $\varepsilon = \varepsilon_0 \varepsilon_r$, the ion valence z, the concentration of ions in the suspension (bulk) c_m (m^{-3}), the Boltzmann constant $k_B = 1.38 \times 10^{-23}$ $m^2 kg s^{-2} K^{-1}$ and the temperature T. Depending on the fluid properties the Debye length can typically take values between 1 and 100 nm.

The Debye length is independent of the particle surface and zeta potential. It must not be mistaken for distance from the particle surface to the slipping plane which is dependent on the surface potential and the Debye length.

The Gouy-Chapman-Stern model is the most commonly applied model to describe the charge density at interfaces with ion containing solutions but there are many other models. The main weakness of the Gouy-Chapman-Stern model lies in the strict separation into homogeneous circuit elements that cannot fully describe the nonuniform distribution of ionic concentrations at surfaces. Bazant et al. (2004) give a good overview of the theory concerning double layers and diffuse-charge dynamics in electrochemical systems.

As will be described in the next section, the double layer can influence particle polarization majorly. Further the double layer can cause electrokinetic particle and fluid motion which will be described in Sec. 2.6.1 and Sec. 2.6.2. In the field of particle filtration the double layer plays a significant role regarding electrostatic particle-particle and particle-filter interactions (Sec. 3.2).

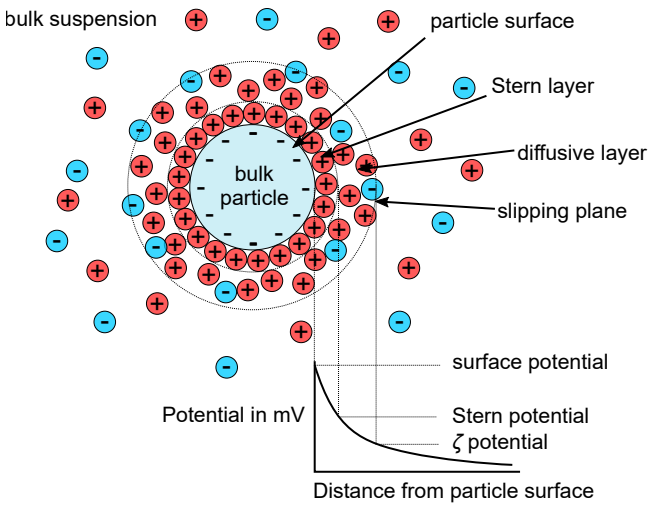

Figure 2.4: Gouy-Chapman-Stern illustration of a particle surface in a suspension containing ions.

2.4 Particle polarization

A particle that is placed in an electric field will polarize due to the described polarization mechanisms electric, atomic, orientational, and interfacial polarization. Independent of the polarization mechanism net charge will just appear at the surface of the particle as shown in Fig 2.5. The material inside the particle remains neutral because it still contains an equal amount of positive and negative charges. At the surface the induced charge displacement leads to an effective dipole that depends in strength and direction on the polarizability of the particle and the surrounding medium. The dependence of the particle dipole on the polarizability of the surrounding medium might surprise at first glance. The reason is that the outside layer (surrounding medium) is tightly bound to the particle surface due to electrostatic and frictional forces.

The simplest model to determine the polarization of a particle is to consider a homogeneous solid sphere with radius r and complex permittivity $\tilde{\varepsilon}_\mathrm{p}$ in a homogeneous medium of complex permittivity $\tilde{\varepsilon}_\mathrm{m}$. In a uniform parallel electric field $\mathbf{E}$ the induced dipole writes as (Morgan and Green, 2002),

$$\mathbf{p} = 4\pi r^3 \varepsilon_\mathrm{m} \left(\frac{\tilde{\varepsilon}_\mathrm{p} - \tilde{\varepsilon}_\mathrm{m}}{\tilde{\varepsilon}_\mathrm{p} + 2\tilde{\varepsilon}_\mathrm{m}} \right) \mathbf{E}. \tag{2.28}$$

This model is called Maxwell-Wagner polarization. The frequency dependent part is called the Clausius-Mossotti factor which will be referred to as CM factor,

$$\tilde{f}_\mathrm{CM}(\omega) = \frac{\tilde{\varepsilon}_\mathrm{p}(\omega) - \tilde{\varepsilon}_\mathrm{m}(\omega)}{\tilde{\varepsilon}_\mathrm{p}(\omega) + 2\tilde{\varepsilon}_\mathrm{m}(\omega)}. \tag{2.29}$$

When dielectric relaxation (Sec. 2.3.4) is neglected the complex permittivities are given by Eq. (2.26). While the real part of the CM factor ($\mathrm{Re}[\tilde{f}_{\mathrm{CM}}(\omega)]$) describes the polarizability of the particle, the imaginary part ($\mathrm{Im}[\tilde{f}_{\mathrm{CM}}(\omega)]$) correlates with the torque that a particle experiences in an electric field due to insufficient time to fully align all charges in field direction. The real and imaginary parts of the CM factor are shown in Fig 2.5c. The absolute value of the imaginary part reaches its maximum at the Maxwell-Wagner relaxation time which is dependent on the permittivities and conductivities of particle and medium, $\tau_{\mathrm{MW}} = (\varepsilon_{\mathrm{p}} + 2\varepsilon_{\mathrm{m}})/(\sigma_{\mathrm{p}} + 2\sigma_{\mathrm{m}})$. The Maxwell-Wagner relaxiation frequency can be calculated as,

$$\omega_{\mathrm{MW}} = \tau_{\mathrm{MW}}^{-1} = \frac{\sigma_{\mathrm{p}} + 2\sigma_{\mathrm{m}}}{\varepsilon_{\mathrm{p}} + 2\varepsilon_{\mathrm{m}}}. \tag{2.30}$$

At frequencies that are much lower than ω_{MW} the polarizability of the particle depends on the conductivities of particle and suspension. The real part of the CM factor is then given by,

$$\mathrm{Re}\left[\tilde{f}_{\mathrm{CM}}\right] = \frac{\sigma_{\mathrm{p}} - \sigma_{\mathrm{m}}}{\sigma_{\mathrm{p}} + 2\sigma_{\mathrm{m}}}. \tag{2.31}$$

At frequencies significantly higher than ω_{MW} permittivities are determining the particles, polarizability

$$\mathrm{Re}\left[\tilde{f}_{\mathrm{CM}}\right] = \frac{\varepsilon_{\mathrm{p}} - \varepsilon_{\mathrm{m}}}{\varepsilon_{\mathrm{p}} + 2\varepsilon_{\mathrm{m}}}. \tag{2.32}$$

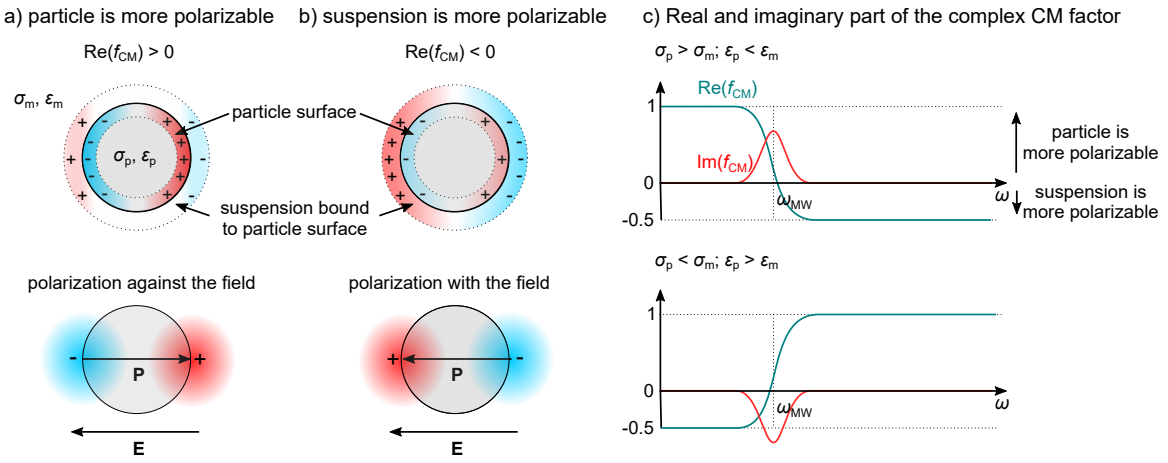

Figure 2.5: Particle polarization in a suspension. Scheme of the charge density at the in- and outside of the particle surface. (a) Particle is more polarizable than the surrounding medium, (b) vice versa. In case (a) the polarization **P** aligns against in case (b) with the electric field **E**. The real and imaginary part of the CM factor as a function of the electric field frequency is shown on the right (c) for the cases $\sigma_{\mathrm{p}} > \sigma_{\mathrm{m}}$, $\varepsilon_{\mathrm{p}} < \varepsilon_{\mathrm{m}}$ and $\sigma_{\mathrm{p}} < \sigma_{\mathrm{m}}$, $\varepsilon_{\mathrm{p}} > \varepsilon_{\mathrm{m}}$.

2.4.1 The influence of the double layer on a low or non-conducting particle

The Maxwell-Wagner polarization model provides a good model to describe particle polarization when the particle surface does not affect the particle conductivity. It is not suited to describe polarization of particles in aqueous suspensions where the double layer (DL) (Sec. 2.3.8) can lead to significant surface conductivities that change the particle polarizability entirely. The increased charge density in the double layer provides an electrically conductive layer around a particle. The influence of the DL on particle conductivity has been investigated for many materials like e. g. latex particles (Ermolina and Morgan, 2005) and silica particles (Honegger et al., 2011, Wei et al., 2009) and viruses (Hughes et al., 2002). A variation of the MW model that accounts for the conductivity of the DL is the Maxwell-Wagner-O'Konski (MWO) model (O'Konski, 1960). The MWO model extends the MW model by assuming the conductivity of a particle σ_p as the sum of its bulk materials conductivity σ_bulk and the contribution of the DL conductance K_DL,

$$\sigma_\mathrm{p} = \sigma_\mathrm{bulk} + \frac{2K_\mathrm{DL}}{r}. \tag{2.33}$$

The conductance of the double layer is dependent on the conductances of both the Stern and the diffuse layer, $K_\mathrm{DL} = K_\mathrm{Stern} + K_\mathrm{diff}$. While the conductance of the Stern layer is independent of the ionic concentration and thus conductivity of the suspension, the conductance of the diffuse layer is a function of suspension conductivity and particle size. The reason for the constant conductance of the Stern layer is that its structure is independent of the suspension's ion concentration. Once the ions are bound to the particle surface the layer remains typically unaltered. The ions in the diffuse layer however are mobile and move due to diffusion. The concentration of ions in DL and bulk suspension strive for equilibrium. The ion concentration in the DL increases with the ion concentration in the bulk suspension. Figure 2.6 a shows exemplary the Stern and diffuse layer conductance for latex particles with diameters between 44 nm and 1 µm that was determined by Ermolina and Morgan (2005). While the conductance of the Stern layer is constant at $K_\mathrm{Stern} = 1\,\mathrm{nS}$ (a for latex particles typical value), the diffuse layer conductance increases exponentially with the suspension conductivity. The diffuse layer conductance is considered relevant at suspension conductivities above $10^{-2}\ \mathrm{Sm}^{-1}$. Ermolina and Morgan (2005) showed further that the MWO model is in good agreement with experimental data for latex particles with diameters above 100 µm. Fig. 2.6 b shows the cross-over frequencies ω_co which is the frequency at which $\mathrm{Re}[\tilde{f}_\mathrm{CM}] = 0$. These were calculated by Ermolina and Morgan (2005) using their predicted conductances from Fig. 2.6 a.

The MWO model fails to describe the polarization of particles at low frequencies

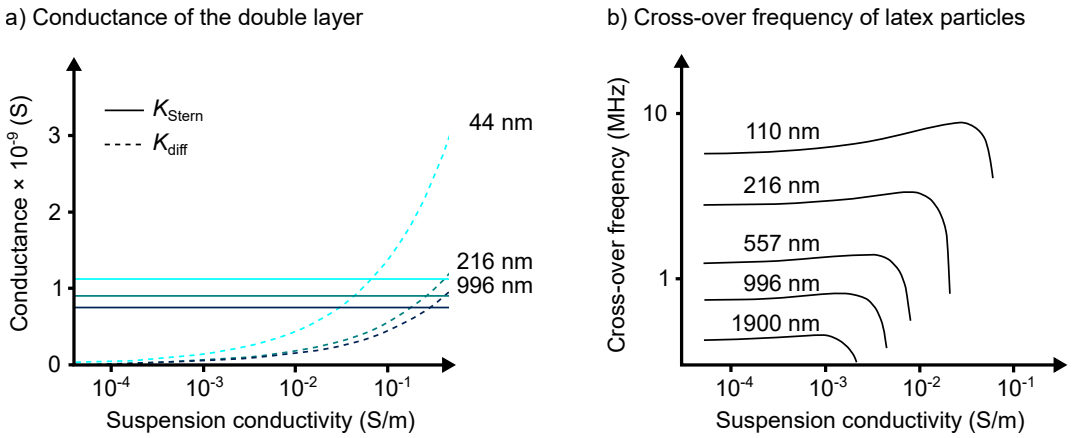

Figure 2.6: Conductance of Stern and diffuse layer of latex particles in an aqueous suspension as a function of the suspension conductivity. Both graphs were remade with permission from (Ermolina and Morgan, 2005), copyright (2004) Elsevier.

because it does not account for ion diffusion from a fully developed DL (Zhao, 2011). Zhao (2011) showed that the Dukhin-Shilov (DS) model can be applied for thin DL and low frequencies (Grosse and Shilov, 1996). This model assumes that diffusion will transport ions from a fully developed DL (ions are highly concentrated at the poles) into the suspension bulk (low ion concentration). The effect results in a dipole that is reduced in strength (because the DL polarization counteracts the primary induced dipole) but has the same direction as the primary induced dipole.

Neither the MWO nor the DS model are suited to describe the polarization of a nanoparticle enveloped by a thick DL. Zhao and Bau (2009) derived that for this case particle polarization can be described by solving the Poisson-Nernst-Planck (PNP) equation.

The above described models provide a basis to interpret the effects that lead to particle polarization. However, it shows that in many cases these models allow rather a prediction than an exact calculation of particle conductivity. In almost all cases the surface conductance of the particles needs to be determined experimentally because it cannot be predicted by calculations yet. A possible reason for this is that surface conductances of particles are very dependent on the various forms of particle surface structures (roughness, functionalization). It further depends on the thermodynamic conditions such as temperature, the types of ions that are involved and their concentration. For example, the surface conductance of latex particles was found to deviate in the range between 0.2 nS and 2 nS Ermolina and Morgan (2005), Schwarz (1962), Arnold et al. (1987), Chow and Takamura (1988).

2.4.2 The influence of the electric double layer on a conductive particle

According to the CM factor (Eq. (2.31)) highly conductive particles such as metal particles would be assumed to be more polarizable than almost any surrounding medium when $\omega < \omega_{MW}$. However, the CM factor of conductive particles at low frequencies is often found to be negative which means that it is less polarizable than the surrounding medium. In their review on the polarization of conductive microparticles Ramos et al. (2016) describe that at sufficiently low frequencies the primary induced dipole of the particle is compensated by charges of the DL. A fully build double layer at equilibrium perfectly disguises a conductive particle which then appears to be non-conducting. Even low conductive liquids appear in comparison more polarizable. The frequency required to fully charge the DL can be estimated by dividing the approximate capacity of the DL of a particle with radius r, $C_{DL}(r) = \varepsilon_m r\kappa$ (Ramos et al., 1999, Bazant et al., 2004), by the conductivity of the surrounding medium σ_m,

$$f_{RC} = \frac{C_{DL}}{\sigma_m} = \frac{\varepsilon_m r\kappa}{\sigma_m}. \tag{2.34}$$

Below this frequency $\mathrm{Re}[\tilde{f}_{CM}]$ of a conducting particle is negative, at higher frequencies it transits to positive values.

2.5 Dielectrophoresis

Particle polarization provides the basis for a magical phenomena called dielectrophoresis. If a polarizable particle is placed in a uniform electric field it will not move because both charges of the induced dipole experience the same magnitude of coulomb forces but to opposite directions. If the polarizable particle is placed in a non-uniform electric field instead, the forces on the dipole charges will differ and the particle move according to the sum of forces. This motion was first issued by Pohl (1951) and later termed dielectrophoresis (Pohl and Hawk, 1966). Particle that are more polarizable than the surrounding medium ($\mathrm{Re}[\tilde{f}_{CM}] > 0$ according to Eq. (2.29)) will move with the electric field gradient $\nabla\mathbf{E}$ and particles that are less polarizable than the surrounding medium ($\mathrm{Re}[\tilde{f}_{CM}] < 0$) will move against $\nabla\mathbf{E}$. The dielectrophoretic force on a spherical particle (neglecting higher order terms) derives from the force on a dipole (Eq. (2.11)) with the dipole of a spherical particle $\mathbf{p}$ (Eq. (2.28)). The time averaged DEP force $\langle\mathbf{F}_{DEP}\rangle$ in an AC field can be expressed with the amplitude of the electric field vector $\hat{\mathbf{E}}$ as (Morgan and Green, 2003)

$$\langle\mathbf{F}_{DEP}\rangle = \pi r^3 \varepsilon_m \mathrm{Re}[\tilde{f}_{CM}]\nabla|\hat{\mathbf{E}}|^2 \tag{2.35}$$

or with the root mean square electric field vector $\mathbf{E}_{\mathrm{RMS}} = \sqrt{0.5}\hat{\mathbf{E}}$

$$\langle \mathbf{F}_{\mathrm{DEP}} \rangle = 2\pi r^3 \varepsilon_{\mathrm{m}} \mathrm{Re}[\tilde{f}_{\mathrm{CM}}] \nabla |\mathbf{E}_{\mathrm{RMS}}|^2 . \tag{2.36}$$

Depending on the particle polarizability and the gradient of the electric field the DEP force is also correlated on the volume of the particle and thus proportional to r^3 and the permittivity of the fluid ε_{m}.

The resulting particle motion can be calculated with the DEP force and the friction factor f_{D} (that accounts for the viscous drag force). The relative motion between particle and fluid can be expressed as

$$\mathbf{v}_{\mathrm{DEP}} = \frac{\mathbf{F}_{\mathrm{DEP}}}{f_{\mathrm{D}}} . \tag{2.37}$$

Assuming a spherical particle and Stokes' drag (laminar flow conditions) the friction factor follows $f_{\mathrm{D}} = 6\pi\mu r$ (with the dynamic viscosity of the fluid μ) and the DEP velocity derives as

$$\mathbf{v}_{\mathrm{DEP}} = \frac{r^2 \varepsilon_{\mathrm{m}} \mathrm{Re}[\tilde{f}_{\mathrm{CM}}]}{3\mu} \nabla |\mathbf{E}_{\mathrm{RMS}}|^2 = \mu_{\mathrm{DEP}} \nabla |\mathbf{E}_{\mathrm{RMS}}|^2 \tag{2.38}$$

with the DEP mobility

$$\mu_{\mathrm{DEP}} = \frac{r^2 \varepsilon_{\mathrm{m}} \mathrm{Re}[\tilde{f}_{\mathrm{CM}}]}{3\mu} . \tag{2.39}$$

Fig. 2.7 shows the DEP mobility for particles of different diameter and effective conductivity as a function of the conductivity of the surrounding medium. The solid lines show that the DEP mobility for particles of 2 µm diameter and effective conductivities of $1 \times 10^{-4}\,\mathrm{S\,m^{-1}}$, $1 \times 10^{-3}\,\mathrm{S\,m^{-1}}$, and $1 \times 10^{-2}\,\mathrm{S\,m^{-1}}$. These curves show that the transition from positive to negative DEP mobility occurs when the fluid electric conductivity matches the particles electric conductivity. The light blue lines show the DEP mobility at constant effective particle conductivity ($1 \times 10^{-3}\,\mathrm{S\,m^{-1}}$) but different particle diameter. The DEP mobility scales proportional to r^2 (Eq. (2.39)).

In AC fields it is possible that particles possess a dipole with a permanent angle to the electric field. As a consequence these particles spin to align their dipole with the electric field. When the time that a particle dipole requires to build is close to the time in which the electric field changes, particle polarization is only partially taking place and is not fully aligned with the external electric field. This "incomplete" polarization is expressed by the imaginary part of the CM factor and the torque is expressed as (Morgan and Green, 2003)

$$\mathbf{\Gamma}_{\mathrm{rot}} = -4\pi \varepsilon_{\mathrm{m}} r^3 \mathrm{Im}[\tilde{f}_{\mathrm{CM}}] |\hat{\mathbf{E}}|^2 . \tag{2.40}$$

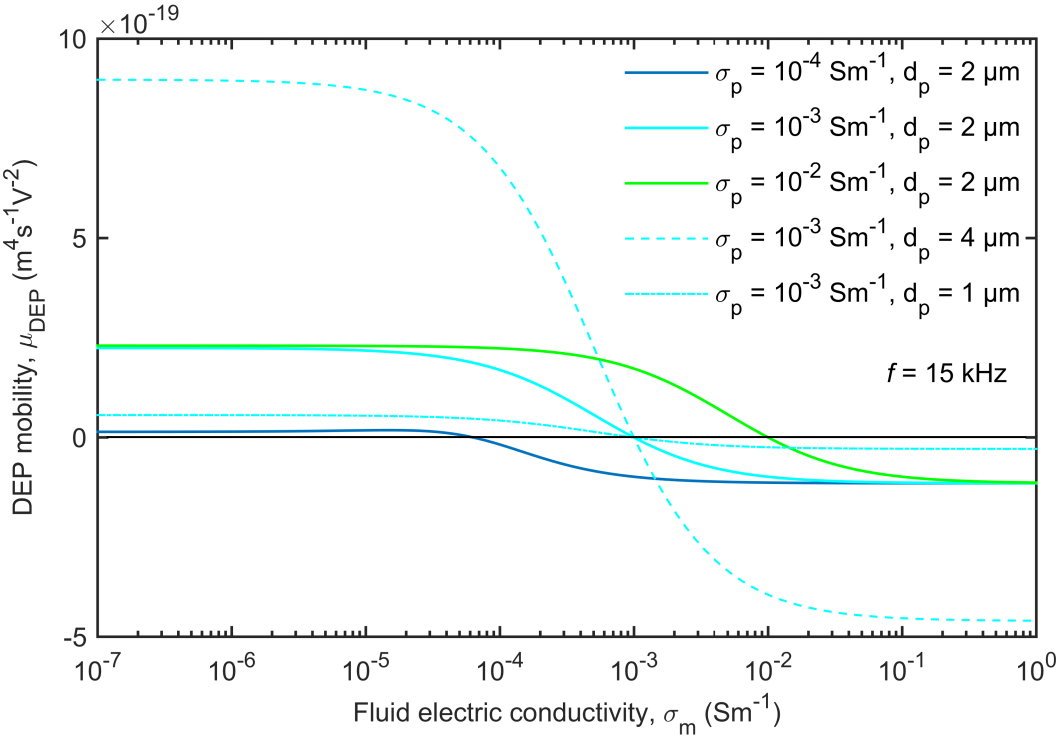

Figure 2.7: DEP mobility for particles of different diameter and effective conductivity as a function of fluid electric conductivity. Calculations were done at a sinusoidal electric field frequency of $f = 15$ kHz for an aqueous fluid ($\varepsilon_\mathrm{m} = 78 \times 8.853 \times 10^{-12}\,\mathrm{F\,m^{-1}}$) and a particle permittivity of $\varepsilon_\mathrm{p} = 2.3 \times 8.853 \times 10^{-12}\,\mathrm{F\,m^{-1}}$.

2.5.1 Particle interaction by DEP

Dipoles that are induced in particles by an electric field generate inter-particle DEP forces. These force can lead to agglomeration and chain formation of particles which is problematic in processes that aim for selective particle separation. It can result in separation of particles that were not intended to be separated and in target particles not being separated for two reasons: The behaviour of agglomerated particles is different than the behaviour of single particles. Further, these forces can lead to agglomeration of particles of different type.

A simple approach to estimate particle interaction due to the DEP force is to compare the DEP force acting between particles to the DEP force acting on the particle due to the applied electric field. The DEP force on a particle towards its closest neighbour particle can be expressed by $F_\mathrm{ip} = 6\pi\varepsilon_\mathrm{m} r^6 E^2 / s_\mathrm{cp}^4$ (Kang and Li, 2006). The ratio of inter-particle DEP force and DEP force due to the applied electric field is then given by,

$$\frac{F_\mathrm{ip}}{F_\mathrm{DEP}} \leq \frac{6\mathrm{Re}\left[\tilde{f}_\mathrm{CM}\right] r^3}{2 s_\mathrm{cp}^4} \frac{\mathbf{E}^2}{\nabla|\mathbf{E}|^2}, \tag{2.41}$$

with the particle concentration- (c-) dependent average distance to the closest particle

being $s_{cp} = (4\pi/(3c))^{1/3}$. It shows that ratio and thus the probability of agglomeration is a function of particle concentration c and particle radius r. It is scaling with $c^{-4/3}$ and r^3. Figure 2.8 shows the particle concentration as a function of the particle diameter for $F_{ip}/F_{DEP} = 1$ and $F_{ip}/F_{DEP} = 0.1$ ($E = 7.5\,\mathrm{kV\,m^{-1}}$ and $\nabla|\mathbf{E}|^2 = 1 \times 10^{13}\,\mathrm{V\,m^{-3}}$).

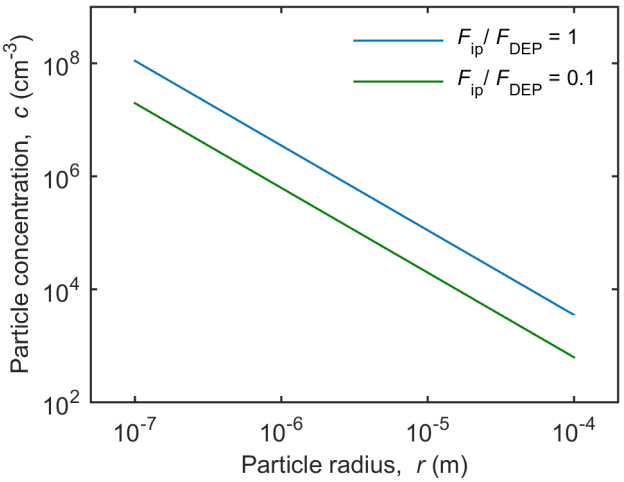

Figure 2.8: Particle concentration as a function of particle diameter for F_{ip}/F_{DEP} of 1 and 0.1. The electric field strength of this calculation is $E = 37.5\,\mathrm{kV\,m^{-1}}$ and $\nabla|\mathbf{E}|^2 = 1 \times 10^{13}\,\mathrm{V\,m^{-3}}$ representing common values of the DEP filtration experiments.

2.6 Other electrokinetic forces in DEP filtration devices

Dielectrophoresis is only one of many electrokinetic phenomena that influence particle motion. They are caused by applied electric fields and charges in electrochemical systems. In this section, some significant phenomena are described, among which are electrophoresis, electroosmosis, induced-charge electroosmosis, and electrothermal flow.

2.6.1 Electrophoresis

Electrophoresis describes the movement of particles with non-zero charge in an electric field. The force derives from the Coulomb force and is given by

$$\mathbf{F}_{EP} = Q\mathbf{E}. \tag{2.42}$$

In an AC electric field this force is oscillating. It falls to a time-average of zero if the electric field change along the oscillating electrophoretic displacement is negligible. In an electrolyte solution the actual mechanism behind electrophoresis is different but leads to the same effective force as given by Eq. (2.42). In an electrolyte solution the particle is

shielded by the electric DL and does not directly experience a Coulomb force (Sec. 2.4). However, the charges in the DL around the particle move according to the electric field. Since they are of opposite charge they move in the opposite direction as the unshielded particle would. Because the fluid bulk motion is zero and the fluid is viscous the particle is propelled while the fluid motion in the double layer equals zero. The effective force on the particle matches the above described Coulomb force. The velocity of the particle relative to the surrounding fluid is

$$\mathbf{v}_{\mathrm{EP}} = \frac{\mathbf{F}_{\mathrm{EP}}}{f_{\mathrm{D}}} = \frac{Q\mathbf{E}}{6\pi\mu r} \tag{2.43}$$

2.6.2 Electroosmosis

Electroosmosis (EO) describes the motion of fluids next to a charged surface in an electric field. It is caused by the motion of ions in the DL at the surface. Shear forces drag the surrounding fluid along resulting in an electroosmotic flux. The electroosmotic velocity tangential to the slip plane of the DL in an DC electric field is

$$v_{\mathrm{EO}} = -\frac{\varepsilon_{\mathrm{m}}\zeta}{\mu} E_{\parallel} \tag{2.44}$$

with the (DL-) tangential electric field component $E_{\parallel}$. As for electrophoresis the electroosmotic velocity time-average is zero in AC electric fields. EO pumping is a well established technique to move fluids in microstructures such as filters and microchannels.

2.6.3 Induced charge electroosmosis

The electric DL around particles and along surfaces builds primarily as a reaction to compensate the surface charge of solids. Both surface and DL charges are in many cases uniform across the surface (from a macroscopic point of view) so that the time-averaged motion due to electrophoresis and electroosmosis falls to zero in ac fields. However, additionally to the uniform DL a secondary non-uniform charge is induced in the DL when particles or solids are polarized (Sec. 2.4). This non-uniform part of the DL moves according to the surface tangential part of the electric field $E_{\parallel}$ and leads to a surface fluid flow which is called induced charge electroosmosis (ICEO) (Fig. 2.9). Around particles charges move from the poles towards the equator where they leave the particle (Fig. 2.9a). The ICEO flow at constrictions is schematically shown in Fig. 2.9b. Charges move along the solid surface towards the edge of the constriction where they leave the surface towards the constriction center. The flow that is approaching the center of the constriction from all directions splits to both sides (normal to the plane through the constriction). Although ICEO is strongest at surfaces of perfectly polarizable materials (where the induced charge

is strongest), it is also occurring at surfaces of other polarizable materials when there is sufficient time to charge the double layer ($f < f_{RC}$ (Eq. (2.34)) (Squires and Bazant, 2004) . The ICEO velocity along dielectric surfaces can be calculated by (Bazant, 2011)

$$v_{ICEO} = \frac{\varepsilon_s \lambda_D E^2}{\mu} \tag{2.45}$$

with the permittivity of the solid ε_s. Especially at sharp corners (where the electric field strength and thus the induced surface charge can locally be very large) ICEO flows can be significant and lead to jets and vortices (Zehavi et al., 2016, Thamida and Chang, 2002, Yossifon et al., 2006). Eq. (2.45) shows further, that the ICEO velocity is linearly increasing with the double layer thickness represented by λ_D which is dependent on the inversed square root of the ion concentration in the the fluid (Eq. 2.27), $c_m^{-0.5}$. ICEO flow is therefore stronger in solutions of low electrolyte concentration.

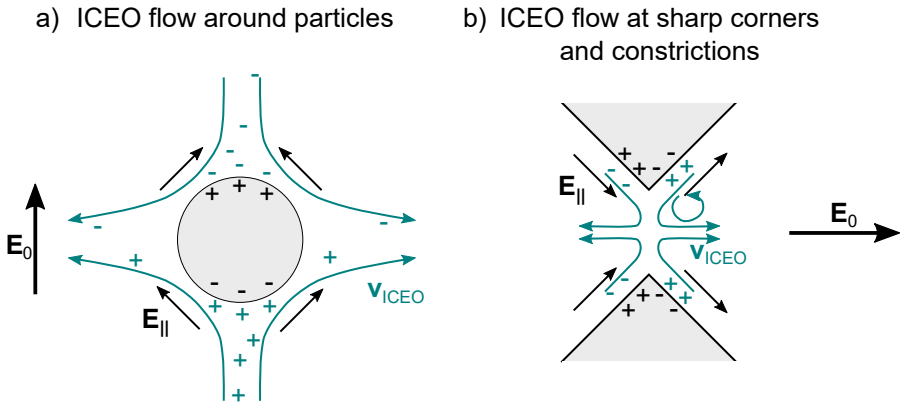

Figure 2.9: ICEO flow around particles and at sharp corners as they are found at constrictions in a microfluidic channels.

ICEO flow at constrictions was studied by Wang et al. (2017) in two-dimensional and three-dimensional microchannels. For a channel of 500 µm diameter and a constriction of 50 µm diameter and a electric field strength of $E_0 = 106\,\mathrm{V\,m^{-1}}$ they determined ICEO velocities of $100\,\mu\mathrm{m\,s^{-1}}$ and $1000\,\mu\mathrm{m\,s^{-1}}$ in 1 mM (electrical conductivity $\sigma_m = 147 \times 10^{-4}\ \mathrm{Sm^{-1}}$) and 0.01 mM ($\sigma_m = 1.5 \times 10^{-4}\ \mathrm{Sm^{-1}}$) KCl solutions.

Application for ICEO flows are for example mixing and pumping in microfluidic devices (Bazant and Squires, 2010, García-Sánchez et al., 2017).

2.6.4 Electrothermal flow

In an electrically conducting medium an electric field produces heat according to $q_{th} = \sigma_m |\mathbf{E}|^2$ (Joule heating: Eq. (2.25)). Since the electric field in DEP devices is inhomogeneous the generated heat in them is also non-uniform. These temperature gradients lead to

gradients in temperature dependent fluid properties among which are density, permittivity, and conductivity. The density gradient leads to natural convection where lighter parts of the liquid rise and denser parts fall. However, natural convection will not be topic in this thesis because it was found that natural convection in microsystems has typically a low impact compared to electrothermal forces (Ramos et al., 1998).

Electrothermal forces are caused where the electric field acts on gradients in permittivity and conductivity produced by non-uniform heating (Morgan and Green, 2003). For microfluidic systems heat transport by convection can usually be neglected because it is about factor 1000 smaller than transport by diffusion. In DC fields or AC field of sufficiently high frequency the temperature distribution can be further considered steady-state so that the temperature gradient can be calculated by (Morgan and Green, 2003)

$$k\nabla^2 T + \langle \sigma_\mathrm{m} |\mathbf{E}|^2 \rangle = 0\,. \tag{2.46}$$

The changes in permittivity and conductivity for aqueous suspensions at weak temperature gradients (commonly the case in microfluidic DEP devices) can be assumed to follow,

$$\varepsilon(T) = \varepsilon_0(1 + C_\varepsilon(T - T_0))\,, \qquad \sigma(T) = \sigma_0(1 + C_\sigma(T - T_0))\,, \tag{2.47}$$

with the temperature $T_0 = 20\,°\mathrm{C}$ and the conductivity and permittivity at T_0, σ_0 and ε_0. The factors for permittivity and conductivity changes are $C_\varepsilon \approx -0.46\%\mathrm{K}^{-1}$ and $C_\varepsilon \approx +2\%\mathrm{K}^{-1}$ (at $T_0 = 20\,°\mathrm{C}$) (Haynes, 2016). The time-averaged electrothermal force derives as (Castellanos, 1998, Morgan and Green, 2003)

$$\langle \mathbf{F}_\mathrm{ETH} \rangle = \frac{1}{2}\mathrm{Re}\left[\frac{\varepsilon_0\sigma_0(C_\varepsilon - C_\sigma)}{\sigma_0 + i\omega\varepsilon_0}(\nabla T \cdot \mathbf{E}_0)\mathbf{E}_0^* - \frac{\varepsilon_0 C_\varepsilon}{2}|\mathbf{E}_0|^2\nabla T\right], \tag{2.48}$$

with $\mathbf{E}_0^*$ the complex conjugate of the applied electric field. It shows that while ICEO forces increase with decreasing electric conductivity, electrothermal forces scale linearly with the electric conductivity. For a channel of 500 µm diameter and a constriction diameter of 50 µm and a electric field strength of $E_0 = 106\,\mathrm{V\,m^{-1}}$ Wang et al. (2017) simulated ETH velocities of $1540\,\mu\mathrm{m\,s^{-1}}$ in 1 mM KCl solutions (electrical conductivity $\sigma_\mathrm{m} = 147 \times 10^{-4}\ \mathrm{Sm^{-1}}$) and $15\,\mu\mathrm{m\,s^{-1}}$ in 0.01 mM ($\sigma_\mathrm{m} = 1.5 \times 10^{-4}\ \mathrm{Sm^{-1}}$) KCl solutions.

2.7 DEP-based particle separation techniques

After treating the basic theory of DEP and related phenomena , this section will turn towards DEP-based applications for particle separation. It will introduce the conventional concepts of DEP-based separation techniques and describe why they are attractive for many separation tasks. It will show that there is currently no DEP-based separation technique established that is capable to process throughputs of industrial scale. Consequently, DEP-based separation techniques are not applicable for many separation tasks that require these throughputs. To overcome the throughput problematic, this thesis suggests to use DEP filtration which is a form of particle trapping. DEP filtration is described in Chapter 4.

2.7.1 Basic principles of DEP-based particle separation

Dielectrophoresis can be used to trap particles, to selectively trap particles, and to sort particles. Particle trapping (Fig. 2.10a) allows to filter particles from a suspension and optionally to recover the filtered particles in concentrated form. Selective trapping (Fig. 2.10b) allows to retain and thus separate a specific target particle from other particles. Particle sorting (Fig. 2.10c) allows to separate particles according to their type in a continuous process without trapping them. All three processes are dependent on the particle DEP mobility μ_{DEP} that describes how a particle moves in an inhomogeneous electric field $\mathbf{E}$ ($v_{\mathrm{DEP}} = \mu_{\mathrm{DEP}} \nabla |\mathbf{E}|^2$), which is dependent on the particle size, shape, and material.

The DEP mobility can be of different absolute value and of different sign. Both can be used for particle trapping and sorting. The absolute value determines how fast a particle moves by DEP per $\mathrm{V^2\,m^{-3}}$. The sign of the DEP mobility and thus the direction of DEP particle motion is influenced by the particles polarizability which is expressed by the real part of the CM factor $\mathrm{Re}[\tilde{f}_{\mathrm{CM}}]$ (Sec. 2.4). Particles that are better polarizable than the surrounding fluid ($\mathrm{Re}[\tilde{f}_{\mathrm{CM}}] > 0$) have a positive μ_{DEP}. They experience positive DEP (pDEP) and are moved in the direction of $\nabla |\mathbf{E}|^2$. Particles that are less polarizable than the surrounding medium ($\mathrm{Re}[\tilde{f}_{\mathrm{CM}}] < 0$ and $\mu_{\mathrm{DEP}} < 0$) experience negative DEP (nDEP) and move against $\nabla |\mathbf{E}|^2$.

Following, the concepts of particle trapping and sorting by DEP is described.

Particle trapping by DEP

Particles are trapped when the DEP force restrains them from follow the fluid flow. This is the case when the particle DEP velocity is higher than the counteracting component of the fluid velocity. Particle trapping can be used to filter particles from a suspension. The trapped particles can be released from the traps by removing the electric field and thus the DEP force. The particles can be recovered in concentrated form. Selective particle

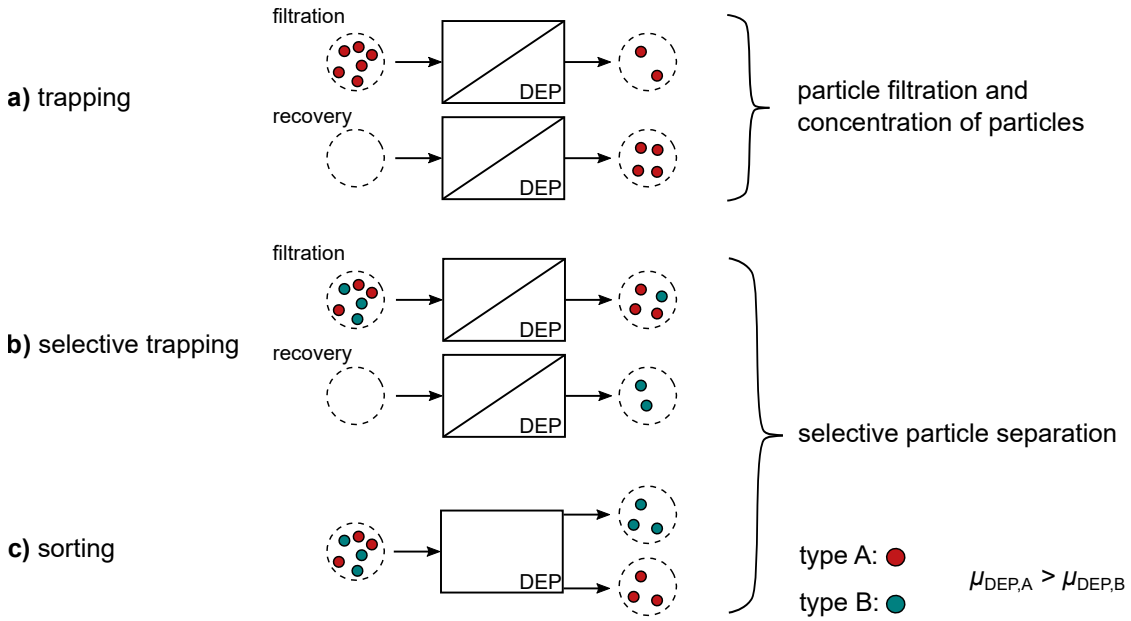

Figure 2.10: Basic principles of DEP-based particle separators. Particles can be trapped by DEP (a). This can be used in a first step to filter particles from a fluid and in an optional second step to recover the particles in concentrated form. Particle trapping can be selective when the difference in DEP mobilities μ_{DEP} is large enough (b). While particle trapping requires batch-wise operation, DEP can also be used to sort particles in a continuous process (c).

trapping is more challenging since only the target particles must be trapped while all other particles must not or vice versa. It can be achieved if the target particle's DEP mobility is sufficiently different from the DEP mobilities of the other particles. In the easiest case, the DEP mobility of the target particle is of different sign than the DEP mobility of the other particles.

DEP particle trapping requires zones where the DEP force to hold particles is stronger than the forces that carry the particles away. In this thesis, such zones will be called "trapping zones". Considering a purely DEP-driven trapping process, Eq. (2.36) shows that these trapping zones can either be at electric field maxima or minima. If particles are more polarizable than the surrounding fluid, they move along with $\nabla|\mathbf{E}|^2$ and are attracted towards the electric field maxima. If particles are less polarizable than the surrounding medium, they move against $\nabla|\mathbf{E}|^2$ and towards the electric field minimum. There are two common concepts that are used to generate the required inhomogeneous electric fields: electrode-based DEP and insulator-based DEP (iDEP). An exemplary scheme of both concepts is shown in Fig. 2.11 together with the zones of nDEP and pDEP trapping.

Electrode-based DEP devices typically use small electrode arrays (often in micrometer scale and below) to generate sufficiently high electric field gradients. Insulator-based DEP devices use external electrodes that apply a rather homogeneous electric field that is then disturbed by an insulating microstructure. (Micro-)electrode-based separators provide

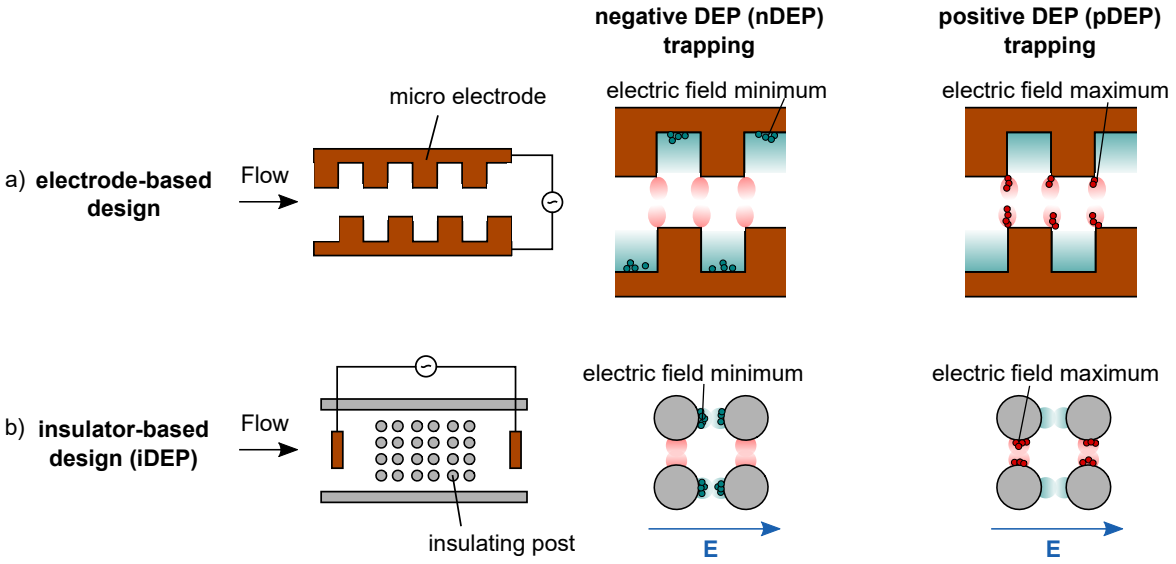

Figure 2.11: DEP particle trapping in an electrode-based (a) and an insulator-based DEP device (b). In the electrode-based design, the field inhomogeneities are generated by the microscale electrodes. In the insulator-based DEP device, the field is disturbed by the microscale insulator structure (represented here by cylindrical posts). The blue particles experience nDEP and are trapped at electric field minima (blue zones) when no other forces occur. The red particles experience pDEP and are attracted to the location where the electric field and the electric field gradient are highest (red zones). Note that position and shape of the zones of the electric field maxima and minima are shown schematically.

the advantage of generating high field gradients and thus selectivity at low to moderate voltage (typically about 10 V) but are expensive to produce which makes them unsuited for increased throughputs. Insulator-based DEP (iDEP) separators are less expensive in their production but require higher applied voltages to generate similar values for $\nabla|\mathbf{E}|^2$. Usually, this requires additional power amplifiers.

DEP-driven particle sorting

In combination with additional forces DEP, can further be used for particle sorting. Here, DEP is not used to trap particles but to move particles of different μ_{DEP} to different positions in the flow. Fig. 2.12 shows two examples how DEP in combination with gravitation is used to move particles of different properties to different stream lines. In both cases, the particle's vertical position is determined by the balance of DEP and gravitational forces. In Fig. 2.12a, this is used to sort the particles into different exits. In Fig. 2.12b, the different fluid velocities at different vertical position $v_{\mathrm{fluid}}(y)$ is used to collect the particles at the outlet at different times. Due to the laminar flow profile particles in the middle of the channel move faster through the channel than particles that are closer to the channel wall. This approach is called DEP field flow fractionation (DEPfff). It requires that all particles are entering the channel at about the same time. DEPfff is therefore a batchwise process.

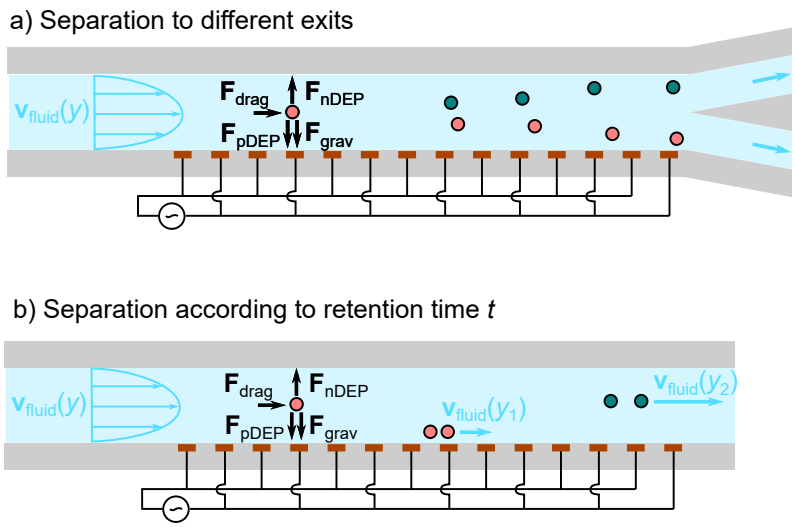

Figure 2.12: Two examples for DEP particle separation by utilizing a fluid flow and interdigitated arrays of electrodes that generate high electric field gradients at the bottom and lower gradient at the top of the channel. The force balance in vertical direction (y-axis) of DEP and gravitational force is used to move particles to different fluid stream lines that lead to separate exits (a) or different retention times (b) due to their different axial velocity $\mathbf{v}_{\text{fluid}}$.

2.7.2 Unique features and limitations of conventional DEP-based particle separators

The capability to use the particle polarizability as a separation criteria is a unique feature of DEP-based particle separation techniques. Because the particle polarizability is dependent on its size, shape, and material, it provides various possibilities for particle separation. Another aspects that makes DEP-based separation techniques particularly interesting is that they do not require to charge or label particles. Separation is possible without altering particle properties which is highly desired in many fields. It was thus found to be suited for analytical purposes and has attracted high interest for biological and medical separation tasks. The following examples showcase the selectivity and versatility of DEP-based particle separation in the field of biology: LaLonde et al. (2015) showed how target cells/particles were separated against millions of background particles. Separation of live and dead cells was already achieved 1966 by Pohl and Hawk (1966). Another field of application is the separation of blood cells according to type (such as circulating tumor cells from whole blood) for analysis (Srivastava et al., 2011, Gascoyne and Shim, 2014, Gascoyne et al., 2009, Pethig, 2017a). Proceeding to even smaller scales, DEP-based separation was also applied to sort DNA according to length (Kawabata and Washizu, 2001, Chou et al., 2002, Gan et al., 2013, Jones et al., 2017) or trap of protein molecules (Hölzel et al., 2005). This list could be extended by many more studies. However, it is not the aim of this thesis to focus on biological applications. Fine reviews about DEP-based separation technology already exist (Pethig, 2010, Hughes, 2016, Pethig, 2017b, Fernandez et al., 2017). Further, Lapizco-

Encinas (2019) summarized the recent development in the field of iDEP-based particle manipulation. A review on the use of DEP for the separation of non-biological particles was recently published by Pesch and Du (2020). Compared to DEP applications for biological purposes, applications for non-biological (technical) particles are very rare. The reason for this is the limited throughput of most currently applied DEP-based separation techniques. The following paragraph explains why there is a throughput limitation.

A characteristic that all DEP-based separators have in common is that they require a non-uniform electric field to move particles. $\nabla|\mathbf{E}|^2$ is crucial because both DEP force and DEP velocity are directly proportional to it. $\nabla|\mathbf{E}|^2$ can be increased by either increasing the applied electric voltage or decreasing the size of the structures. Decreasing the structure size is typically leading to smaller channels which limits the throughputs so that it becomes for many applications from an economic standpoint unattractive. However, increasing the voltage is often not an option because the separation processes need to be done in aqueous solutions (like it is the case for many applications in biology) with relatively high conductivities which require to use relatively low voltages to reduce the generated heat and avoid bubble generation or electrochemical reactions. Therefore, many DEP-based separators generate the required high electric field gradients by using small scale electrode structures that allow high selectivity but typically throughputs in the order of $\mathrm{mL\,h^{-1}}$. Examples are the the tooth design in Fig. 2.11 or the interdigitated array of electrodes in Fig. 2.12. Due to their expensive production, electrode-based separators are not suited for processing higher throughputs as they could, in principle, be achieved by numbering up and running thousands of microchannels in parallel. iDEP separators are less expensive to produce (isolating microstructures are less expensive to produce than microelectrodes). However, because most iDEP devices use nDEP to retain particles flow, velocities in them need to be chosen rather small to obtain a drag force low enough for the nDEP force to compete with. Therefore, the majority of iDEP devices are also not suited for increased throughput.

Literature indicates that DEP filtration is currently the only DEP-based separation technique that has shown to work for particle separation from a water based suspension at medium to high throughput. Despite its potential for increased throughput, DEP filtration has received minor attention in comparison to conventional DEP-based separation techniques that have been discussed above. This thesis focuses on investigating the possibilities of DEP filtration and gives an overview of this technique in Chapter 4.

Chapter 3

Theory: Particle trapping by depth filtration effects

This chapter will give an overview about depth filtration which can have a significant impact on DEP filtration processes (as will be shown throughout this thesis). The mechanisms that lead to particle trapping in a depth filtration process will be described. It will be shown how particles are captured (transported to the filter surface) and how they are retained at the filter surface by adhesion. It will also be described under which conditions adhesion forces lead to particle agglomeration, which is typically unwanted when aiming for selective particle separation. Further, it will be shown how particle retention efficiency is commonly modelled. At the end of this chapter, filter capacity and saturation will be described.

3.1 Particle capture mechanisms

Here, the major mechanisms that account for particles hitting the filter surface are described.

Inertial impaction between particles and filter occurs when a particle is not following the fluid stream lines due to its inertia. With increasing particle cross section, velocity and density particles do not change direction as sharply as the fluid flow. If a particle that moves towards an obstacle hits the obstacle or follows the flow around it depends on the dimension of the obstacle (typically its diameter) L, the inertia of the particle and the drag exerted by the fluid. This effect is characterized by the Stokes number. The Stokes number characterizes if particles follow the streamlines at obstacles. It is defined as

$$\mathrm{St} = \frac{d_\mathrm{p}^2 \rho_\mathrm{p} v_\mathrm{fluid}}{18 \mu L}, \tag{3.1}$$

with the particle diameter d_p, the particle volumetric mass density ρ_p, the fluid

velocity v_{fluid}, the fluid dynamic viscosity μ, and the characteristic length/diameter of the the obstacle L. The Stokes number describes the ratio between the characteristic time that a particle needs to change its motion according to the flow to the characteristic time that the fluid changes its direction. $\text{St} \ll 1$ means that particles are following the fluid stream lines well. Under these conditions, particles can follow the flow around an obstacle and avoid hitting it. $\text{St} \gg 1$ means that particles are slow to react to the fluid flow around an obstacle and are likely to hit obstacles.

Sedimentation and buoyancy become important when the density of the particle differs from that of the fluid. Particles move across flow streamlines by these effects and can settle onto the filter surface. The probability of deposition is characterised by the dimensionless term

$$\frac{d_{\text{p}}^2(\rho_{\text{p}} - \rho_{\text{m}})g}{18\mu v_{\text{fluid}}} \tag{3.2}$$

that describes the ratio between the Stokes settling velocity and the velocity of the fluid (Wakeman and Tarleton, 2005). If this value is significantly smaller than 1, sedimentation of particles can be assumed to be negligible.

Interception is taking place under laminar flow conditions (which are the most common conditions in small-scale filtration systems), when a particle, despite following the fluid flow, gets in contact to the filter. This is only the case when particles move along a fluid stream line that gets as close as one particle radius or closer to the filter surface. Interception is characterized by the ratio of particle diameter and filter hydraulic diameter $d_{\text{p}}/d_{\text{h}}$.

Straining occurs when a particle in the feed is larger than the pore or constriction through which it attempts to pass.

Diffusion of particles (Brownian motion) arises from random collision of molecules with particles. Especially small particles may acquire sufficient momentum from these collisions to move across streamlines. For particles in the vicinity of the filter surface Brownian motion can cause them to collide with the filter. The mechanism is characterized by the Peclet number defined as

$$\text{Pe} = \frac{d_{\text{p}} v}{D_{\text{BM}}} \tag{3.3}$$

that depends on the particle diffusion coefficient, $D_{\text{BM}} = (k_{\text{B}} T)/(6\pi a \mu)$ (Einstein, 1905), with the Boltzmann constant $k_{\text{B}} = 1.38 \times 10^{-23}$ and the temperature T. The Peclet number expresses the ratio of particle transport by advection and particle

diffusion. If Pe << 1, transport by advection is negligible in comparison to transport by particle diffusion. If Pe >> 1, it is the other way around.

3.2 Particle adhesion to the wall and interaction with each other

When particles get in contact to each other or to the filter surface, they experience additional short distance forces that can be repulsive or attractive. These short distance forces determine if particles are attracted or repelled from each other and thus if they agglomerate or are stably dispersed and also if particles adhere to surfaces like a filter surface (which leads to particle retention) or if they are repelled. The most commonly applied theory to predict these forces is the Derjaguin-Landau-Verwey-Overbeck (DLVO) theory. The DLVO theory combines both electrostatic DL and van der Waals interaction and describes the potential and the forces between charged surfaces that interact through a liquid medium. In the following, we do a short theoretical excursion on the DLVO theory.

3.2.1 Van der Waals attraction

All atoms and molecules contain charges and possess either permanent dipoles or are polarizable. When atoms or molecules approach each other they interact by these permanent or induced dipoles. This can lead to permanent chemical bindings of covalent, ionic or metallic nature or lead to particle corrosion (conversion to other materials). Further, it leads to a weaker form of particle interaction that is always present, the van der Waals forces. Van der Waals forces are caused by fluctuating polarizations (fluctuation due to temperature) of atoms and molecules in particles that are close to each other. Van der Waals forces are always attractive, since the dipoles will on average align in a way to minimize the potential energy so that they attract each other. The interaction energy is thus always negative and can be calculated by the Derjaguin approximation (Derjaguin, 1934) for different geometries. For two spherical particles of radii r_1 and r_2, it is given by

$$W_{\mathrm{vdW}}(y) = -\frac{A_{\mathrm{H}}}{6y}\frac{r_1 r_2}{r_1 + r_2}, \tag{3.4}$$

with y the shortest distance between the particle surfaces and the Hamaker coefficient $A_{\mathrm{H}} = \pi C \rho_1 \rho_2$ (tabulated by (Israelachvili, 2015)), where C is a constant for interaction energy that depends on the atom's/molecule's interaction. ρ_1 and ρ_2 are the number densities of atoms/molecules of the surfaces. The Hamaker coefficient describes the magnitude of van der Waals force between atoms or small molecules. It has the unit Joule.

If a spherical particle of radius r and a plain surface are considered, the interaction energy is given by

$$W_{\mathrm{vdW}}(y) = -\frac{A_{\mathrm{H}} r}{6y}. \tag{3.5}$$

Van der Waals forces are effective only up to several hundred Ångström. Above this limit, they decay quicker than with their typical proportionality of y^{-6}.

3.2.2 Double layer force

The electrostatic force between two surfaces is generated by the electric double layer which was introduced in Sec. 2.3.8. An expression for the repulsive free energy between two spheres was derived by Israelachvili (2015)

$$W_{\mathrm{el}}(y) = \frac{64\pi c_{\mathrm{ion}} k_{\mathrm{B}} T r \gamma^2}{\kappa^2} \exp(-\kappa y) \tag{3.6}$$

with the number density of ions in the bulk solution c_{ion} and $\gamma = \tanh\left(z q_{\mathrm{e}} \Phi_0 / 4 k_{\mathrm{B}} T\right)$, where the surface potential is Φ_0 and the valence of the ion z. The repulsive free energy per unit area between two planar surfaces is described by

$$W_{\mathrm{el}}(y) = \frac{64 c_{\mathrm{ion}} k_{\mathrm{B}} T \gamma^2}{\kappa} \exp(-\kappa y). \tag{3.7}$$

The total potential interaction energy of two particles coming close to each other is described by the sum of attraction and repulsion potential

$$W_{\mathrm{DLVO}} = W_{\mathrm{vdW}} + W_{\mathrm{el}} \tag{3.8}$$

with W_{vdW} and W_{el} after Eqs. (3.4) and (3.6). Fig. 3.1 shows qualitatively the interaction potential between two particles of equal surface charge as a function of the shortest distance between their surfaces. The potential shows two energy minima and one energy maximum (barrier). A negative interaction energy means that the particles give energy to the surroundings. This is a favorable state which means that the particles "like" to stay there: They attract each other. A positive interaction energy means an unfavorable state and repulsion. When two particles approach each other according to Fig. 3.1 they will first be attracted towards each other (secondary energy minimum). If they have sufficient kinetic energy to overcome the energy barrier, they can further reach the primary energy minimum. In this minimum, attraction is stronger than repulsion and particles are tightly bound. The DLVO does not account for the forces between the atomic electron orbits (represented by the dashed line), which are stronger than the vdW forces and prevent collapse.

The DL interaction potential is very dependent on the particle surface potential Φ_0 and the ion concentration in the surrounding liquid c_{ion}. If particles posses absolute zeta potentials of the same sign of 40 mV and above, a solution can be accounted as stable (Mandzy et al., 2005). In this case, the DL repulsion increases to a level that the secondary minimum is positive (repellent) and the barrier becomes usually too high for particles to pass. The ion concentration in the surrounding liquid affects the DL thickness and thus the range of electric forces between particles. The lower the ion concentration, the thicker the DL and the wider the range of electric forces, so that the secondary minimum might not exist. It is expected that this rule is also valid for the interaction between particle and wall: If particle and wall posses absolute zeta potentials of the same sign above 40 mV, particles do not adhere to the wall.

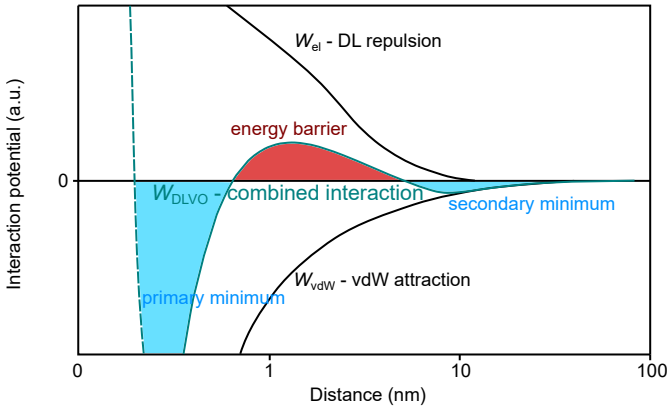

Figure 3.1: Interaction potential between spherical particles in solution as a function of their separation distance. Negative potentials cause attraction while positive cause repulsion.

3.3 Particle retention efficiency in depth filtration

As described, particle retention in depth filtration depends on the rate of particle collision due to the capture mechanisms described in Sec. 3.1 and particle adhesion due to short distance interactions with the filter (sec. 3.2). Particle capture (transport to the wall) can be determined from simulations. For short distance interaction between particles and filter, there is no method capable to predict the attachment efficiency that fully describes all impact factors (McDowell-Boyer et al., 1986, Molnar et al., 2019). This is why the attachment efficiency in depth filtration is still determined by an experimental fitting factor. Particle retention profiles in depth filtration can typically be described as an exponential function of the filter length because the concentration of retained colloids decreases exponentially with distance (Molnar et al., 2019). The basic equation that describes the

particle concentration as a function of the distance that a suspension has passed through a filter was proposed by Iwasaki et al. (1937) as

$$c(L) = c_0 \exp(-\lambda_0 L)\,, \tag{3.9}$$

where λ_0 is the filter coefficient, L the the distance along the direction of flow ($L = 0$ at the filter inlet) and c_0 the concentration at the filter inlet (McDowell-Boyer et al., 1986).

3.4 Capacity and saturation

A further aspect that influences the separation process of depth filtration is the filter saturation. Saturation is commonly defined as the ratio of filter volume that is filled by particles to the filter volume that can be filled with particles. The later is also called filter capacity and is given by the filters void volume minus a layer of half a particle radius thickness at the outside of the filter-fluid interface (because the particle center cannot get closer to the surface than half their diameter). The higher the saturation of a filter the lower the capacity to trap further particles. The influence on the trapping efficiency can be quite different. A saturated filter provides narrower flow paths resulting in increased trapping, but it can also lead to bigger clusters of particles breaking free from their trapping zones and leaving the filter.

Chapter 4

DEP filtration

The fundamentals of DEP and DEP-based particle separation were presented in Sec. 2.5 and Sec. 2.7, respectively. It was shown that DEP is a versatile tool for highly selective particle separation. It was further shown that conventional (microfluidic) DEP-based separation techniques are unsuited to process throughputs of preparative or industrial-scale as required for many separation tasks. To overcome the throughput problematic, this thesis suggests to use DEP filtration which is a form of DEP-based particle trapping.

This chapter gives an overview on DEP filtration. It describes the concept of DEP filtration and how DEP filtration can be applied to separate particles from liquids and selectively from each other. The few existing studies, which represent the state-of-the-art about this technique will be presented. Based on the state-of-the-art, the objectives of the thesis will be formulated and presented together with the thesis workflow.

4.1 The Concept of DEP filtration

DEP filtration is an insulator-based DEP (iDEP, Fig. 2.11b) particle trapping technique that uses DEP (usually pDEP) to trap particles in porous microstructures from mechanically pumped suspensions. As in any iDEP device, the electric field is produced by electrodes (e. g. plate electrodes) that can be several orders of magnitude further apart from each other (centimeter and above) than microelectrodes (Fig. 2.11a). The resulting homogeneous electric field is disturbed by placing a porous microstructure between the electrodes. The big difference of DEP filtration to “conventional” iDEP devices is that it does not require costly produced insulating structures but uses low cost and easy-to-scale-up porous microstructures, such as monoliths or packed beds. These microstructures provide numerous macro- and microscopic flow paths in parallel which are well suited for particle trapping. Each flow path can contain numerous trapping zones and is comparable to an iDEP microchannel. Due to the low costs and the easy scale-up DEP filtration has the potential to

increase the processable throughput of DEP-based separation techniques. A schematic of a DEP filtration device, showing an open-porous filter sandwiched between two electrodes and particles that are pumped through it, is shown in Fig. 4.1.

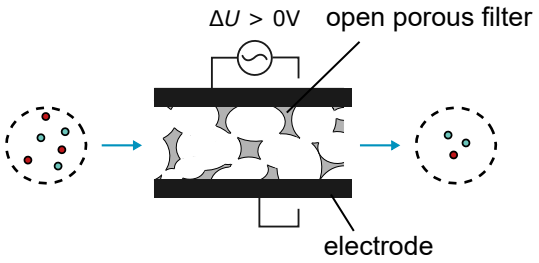

Figure 4.1: Schematic of a DEP filtration device.

Following the DEP mechanisms that cause DEP trapping in the porous filters will be described.

Particle trapping in DEP filtration

The basic principle of DEP-based particle trapping is explained in Sec. 2.7.1. Summarized: Particle motion is determined by the drag force (exerted by the fluid) and the DEP force. A particle is trapped by DEP, when the DEP force is strong enough to keep the particle from following the fluid flow.

Direction and strength of the DEP force is determined by the gradient of the electric field squared ($\nabla|\mathbf{E}|^2$). Hence, to derive the locations of DEP particle trapping it is required to have information about the characteristics of the electric field ($\mathbf{E}$) in a depth filter. In a porous depth filter the solid phase has typically a lower permittivity than the fluid. Under this assumption, the local maxima of electric field and $\nabla|\mathbf{E}|^2$ are located at constrictions of the fluid phase. The electric field has literally to squeeze through the constrictions. More precisely, the maxima are at the edges of the constrictions (Fig. 4.2a). The local minima of the electric field are typically located well distanced from constrictions at the filter surface where $\nabla|\mathbf{E}|^2$ is rather low (Fig. 4.2a).

Consequently, DEP forces (no matter if positive DEP (pDEP) or negative DEP (nDEP), see Sec. 2.5) are strongest at the electric field maxima. Particles that experience pDEP are attracted towards the edges of the constrictions (Fig. 4.2b). They are trapped at the wall, where the drag force is low but the DEP force is maximal. Accordingly pDEP trapping is strong. In contrast to that, particles that experience nDEP are attracted towards the electric field minima but it can be expected that the nDEP force at these locations is often not strong enough to compete against the drag force and trap particles (because $\nabla|\mathbf{E}|^2$ is low). More than being attracted towards the electric field minima they are repelled by the electric

field maxima. It is thus assumed that particles are rather trapped in front of constrictions than at electric field minima (Fig. 4.2c).

These different trapping mechanisms of pDEP and nDEP can result in very different particle separation efficiencies. nDEP trapping is expected to be less efficient to trap particles for the following reasons.

i) As evident from the negative bound of Re $[\tilde{f}_{\mathrm{CM}}]$ (expresses the particle polarizability, Sec. 2.4) of -0.5 compared to the positive bound 1, nDEP trapping can only be half as strong as pDEP trapping.

ii) nDEP trapped particles are not tightly trapped at the filter surface but in the moving fluid phase. They are therefore stronger affected by the fluid drag.

iii) While pDEP can already trap particles when the maximum of $\nabla|\mathbf{E}|^2$ is high enough to retain a particle, nDEP trapping is only taking place when $\nabla|\mathbf{E}|^2$ across the whole constriction is high enough to repel particles and stop particles from passing. Thus, nDEP is determined by the DEP force in the center of the constriction, which is by orders of magnitude smaller than the DEP force at the edge of the constriction (see Simulation of $\nabla|\mathbf{E}|^2$ in Sec. 6.2.1).

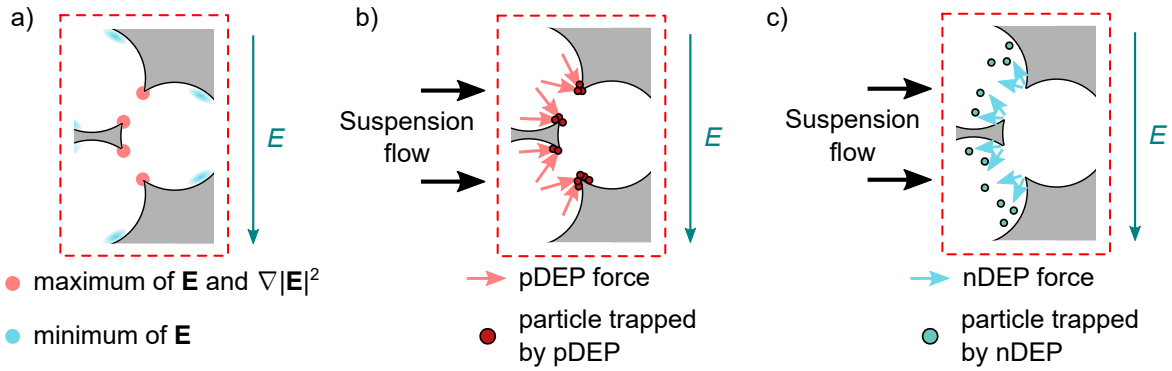

Figure 4.2: Schematic of maxima and minima of electric field and $\nabla|\mathbf{E}|^2$ in an open-porous filter (a). Shown is an exemplary section of the alumina-mullite filter that was used for experiments (grey). Further, the resulting DEP forces that lead to pDEP (b) and nDEP (c) particle trapping are shown.

4.2 Potential applications of DEP filtration

Following the above presented DEP trapping mechanisms, this section describes the theoretical applications of DEP filtration.

An overview of these possibilities is given in Fig.4.3. If no electric field is applied to the filter, particles can follow the fluid flow and pass the filter, which provides pores that are much bigger than the particle size (Fig.4.3a). When an electric field is applied, the field is locally disturbed by the porous filter resulting in a vast number of electric field maxima. Particles that are more polarizable (pDEP) than the surrounding medium (blue) are pulled towards the electric field maxima at the filter wall where they are trapped (Fig.4.3b). Particles, equal (no DEP) or less polarizable (nDEP) than the medium (red), are not affected or pushed away from the field maxima and thus pass through the filter because they remain in regions of dominant fluid flow. This allows to selectively trap particles from particle mixtures (Fig.4.3c). The trapped particles can be recovered when the electric field is switched off and particle adhesion forces are low enough allowing the particles to detach from the filter surface (Fig.4.3d).

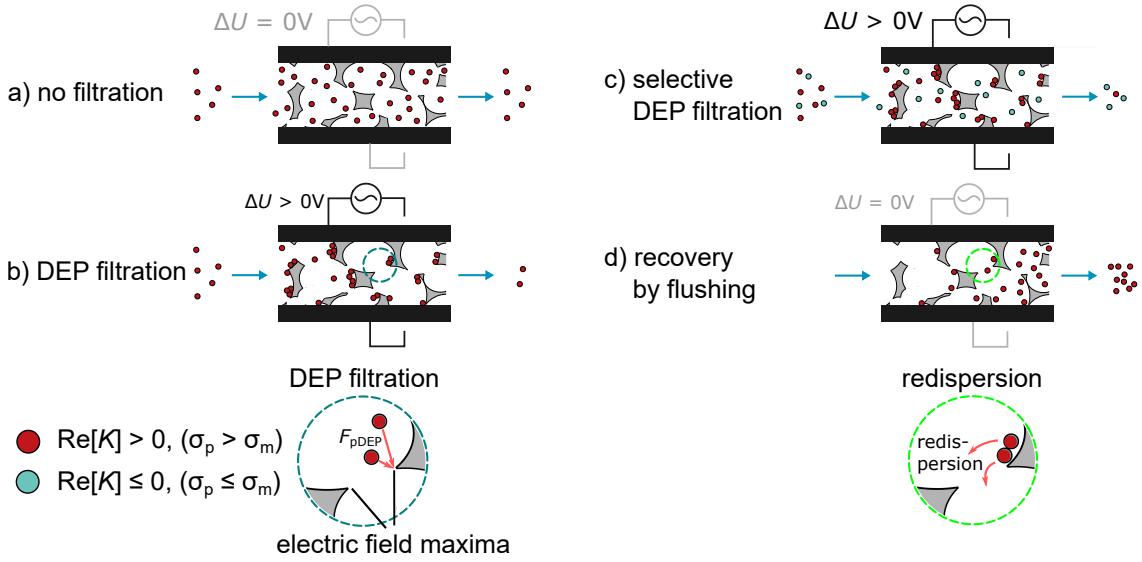

Figure 4.3: Schematic of the modes of DEP filtration. The Figure is reprinted with permission from (Lorenz et al., 2020) in modified form.

4.3 Research and studies on DEP filtration

The studies about DEP filtration are very few compared to research on other DEP-based separation techniques.

The first DEP filter was invented by Fritsche and Haniak (1975) and was later named Gulftronic separator (Fig 4.4a). The cylindrical shaped separator used a concentric electrode arrangement consisting of an inner rod electrode and an outer tube-shaped electrode. As a filter matrix, they employed glass beads in between the electrodes. The filter was used for several different applications in low conductive fluids. Some examples are the separation of fluid catalytic cracking catalyst fines from decanted oil, the removal of metallic fines from metal working fluids, and the separation of hydrogenation catalyst particles from vegetable oil.

Benguigui and Lin discussed this separator (Lin and Benguigui, 1982, Benguigui and Lin, 1982) and later developed a DEP filter themselves that separated PVC from kerosene isopropanol mixtures ($\sigma = 5 \times 10^{-7}\,\mathrm{S\,m^{-1}}$) in separators of industrial scale (Lin and Benguigui, 1985). At flow rates of $15\,\mathrm{mL\,min^{-1}}$, they removed up to 80% of the particles from the suspension. They used two electrodes with the geometry of concentric cylinders and filled the gap between the inner and outer electrode with $BaTiO_3$ beads of 2 mm to 6 mm diameter. The applied field strength was about $100\,\mathrm{kV\,m^{-1}}$. Sisson et al. (1995) applied DEP filtration in a packed bed of 1 mm glass spheres to separate silica nano particles (50 nm to 300 nm) from a low conductive tert-amyl alcohol suspension. They applied dc voltages of up to $800\,\mathrm{kV\,m^{-1}}$. Wakeman and Butt (2003) investigated DEP filtration in a similar device using 500 µm glass beads to separate air conditioning test dust and PVC particles from Tellus 37 oil achieving 0% to 60% separation at up to $180\,\mathrm{L\,h^{-1}}$. They found in experiments and modeling that the separation increases with the electric field strength, decreases with the fluid velocity and the fluid viscosity. They argued that the technique could be used in multi-step separation processes.

The applications described above have in common that they involve DEP filtration in very low conductive/insulating liquids. The reason for this was already mentioned in the last chapter. DEP filtration requires high voltages in order to generate forces that can compete with the fluid drag present in high throughput devices. In non-insulating liquids these voltages lead to currents and Joule heating as well as electrochemical reactions like electrolysis in water. Both can lead to formation of gas bubble in the filter that alter the filter characteristics (flow velocity, flow paths, pore size etc.) or destroy or change the involved particles. However, for many applications it is necessary to be able to use DEP filtration on aqueous suspensions to allow, for example, separating biological and medical samples like bacteria, algae, and cells (e. g. blood or circulating tumor cells (CTCs)). Further, separation

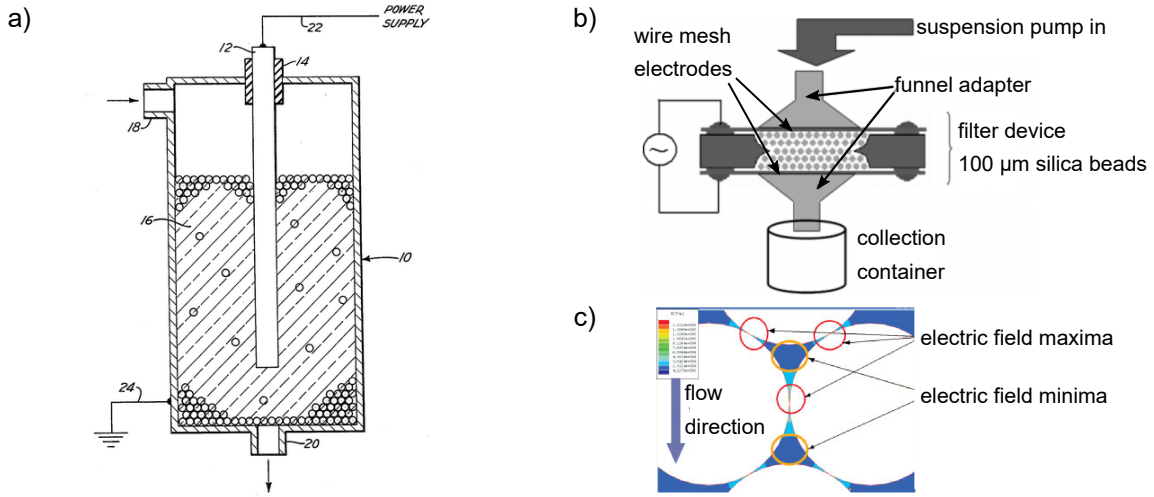

Figure 4.4: First developed DEP filtration apparatus (Gulftronic separator) to separate fluid catalytic cracking catalyst fines from decanted oil, metallic fines from metalworking fluids, and hydrogenation catalyst particles from vegetable oil (a) (Fritsche and Haniak, 1975). 3D DEP separation chip used for separation of yeast cells from water (b). Both filters use packed beds of spherical beads. The electric field distribution in a packed bed of beads is shown on the bottom right (c). (b) and (c) are reprinted with permission from (Iliescu et al., 2007a), copyright (2007) Elsevier.

in aqueous suspension has the advantage of being ecologically uncritical. The only studies that were found by the author about DEP filtration in aqueous suspensions were done at significantly decreased throughput. Suehiro et al. (2003) investigated DEP filtration of yeast cells from low conductive aqueous suspensions using a packed bed of glass beads with 200 µm diameter. They separated up to 99.999% at 1 mL min^{-1} with an ac voltage of 140 V_{PP} at 100 kHz. They further showed that they could separate viable from non-viable yeast cells achieving a remarkable purification factor of 1000. They state that their approach could be scaled up but remarked that the generated heat generated in bigger scale filters could be critical, especially when working with relatively high electrically conductive biological samples. They also mentioned that cell recovery was possible by "switching off" the filter. A second study of DEP filtration in an aqueous suspension was done by Iliescu et al. (2007a,b). They separated yeast cells from deionized water using a 7mm × 7mm × 1mm chamber (3D filter chip) filled with 100 µm glass beads and achieved separation efficiencies of up to 75% at 0.1 mL min^{-1} and a ac voltage of 200 V_{PP}. The third and last study about DEP filtration in aqueous suspensions was done at the group of Chemical Process Engineering (CVT) at the University of Bremen). They used a monolithic polymer foam of 20 µm to 160 µm pore size as filtration matrix sandwiched between two metal electrodes to separate very small layer-by-layer–produced particles (340 nm) from conducting aqueous suspensions (Pesch et al., 2014). They achieved separation efficiencies of 38% at throughputs of 1 mL min^{-1} applying 200 V_{RMS} voltage at 200 kHz.

Since then, the same group has done further theoretical studies on DEP filtration. They

aim to understand the physics and scaling behind the technique and derive guidelines to design DEP filtration devices that work also for aqueous suspensions. They calculated the polarization around single obstacles of different shape and evaluated the resulting electric fields with the aim to find suitable obstacle geometries for particle trapping (Pesch et al., 2016). They found that there is a trade-off between maximum field gradients and the coverage of the electric field gradient that is influenced by the sharpness of the insulating structure. Using insulating posts with sharp edges led to increased $\nabla|\mathbf{E}|^2$ maxima at these sharp edges but the gradient decreased much faster when moving away from these edges than in a filter with rounded insulating posts. In a second work, they focused on DEP particle trapping at single obstacles (polarizable posts) to derive dependencies on important process parameters like the electric field strength, post geometry, post dimension, particle size, and particle velocity (Pesch et al., 2017). This approach was further developed to simulate of particle trajectories in model filter structures (consisting of post arrays) and led to the derivation of design rules for DEP filtration. These were afterwards validated with experiments in Polydimethylsiloxane (PDMS) microchannels that contained the same model porous filter structures (Pesch, 2018). The separation efficiency by DEP in the model porous structures was found to follow $\eta = 1 - \exp(\bar{x}/C)$, a function of the variable $\bar{x} = (\Delta U)^2 Q^{-1} d_\mathrm{p}^2 \mathrm{Re}\left[\tilde{f}_\mathrm{CM}\right]$. $\bar{x}$ contains the applied voltage ΔU, the volumetric flow rate Q, the particle diameter d_p, and the real part of the complex CM factor $\mathrm{Re}\left[\tilde{f}_\mathrm{CM}\right]$. C is a fitting parameter.

4.4 Aims and approach of this thesis

Most of the above described studies solve specific separation problems. While they show that separation of particles from liquids is possible at increased throughputs, they do not provide an in-depth understanding of the technique. The studies of Pesch et al. were the first that aimed for general design rules for DEP filtration. To derive fundamental understanding, they used simplified two-dimensional models of porous filter structures. In simulations, they predicted how DEP particle retention scales with essential process parameters such as electric field strength, filter post geometry, particle size, and particle velocity (Pesch et al., 2016, 2017) (Pesch, 2018). However, validation of their predicted scaling has only been carried out in two-dimensional model structures. If they are applicable to real porous filters has still to be validated. The overview of the few existing studies on DEP filtration reveals that fundamental understanding of the process and its potential applications is missing. There are only a few studies that mention particle recovery, studies on selectivity are entirely missing.

This thesis aims to approach these open questions in a comprehensive experimental

study in real porous filters. It shall provide experimental data for validation of design rules and to determine the possibilities of selective particle separation. An overview of the outline and workflow of this thesis is presented in Fig. 4.5. A major task was the development of a DEP filtration concept and the realization of this concept in a DEP filtration device that allowed the experimental investigations. The description of the DEP filtration device is given at the end of this thesis in Chapter 5.

The trapping mechanisms in depth filters are theoretically evaluated in Chapter 6 to derive a basic understanding of the process. In this context depth filtration and DEP filtration effects are considered. In most DEP filtration processes, particle trapping by depth filtration is unintended because it traps non-target particles. This is problematic because it decreases the selectivity of DEP filtration processes. Investigating the impact of depth filtration is essential to understand how these effects can be reduced. Fluid flow and electric field simulations are used to calculate particle trajectories. In contrast to the previous investigations of Pesch et al. this evaluation will use 3-dimensional instead of 2-dimensional model structures. The model structure geometry was designed based on the real filter structures that were used for experiments. The aim is to provide a detailed simulation of DEP filtration in real (3-dimensional) filters that provides a basis to discuss experiments. The calculated particle trajectories will be used to predict how the particle separation efficiency depends on applied voltage, superficial fluid velocity, and filter pore diameter.

In Chapter 7, DEP filtration will be investigated in practice in real porous filters. The chapter derives design rules and understanding of the basic effects of DEP filtration. In a parametric study, the dependency of the separation efficiency on essential process parameters, such as, applied voltage, volumetric flow, filter pore diameter, and filter pore geometry will be investigated. It will be tested if the derived parametric dependencies (of Pesch et al. (2018) and the theoretical evaluations of Chapter 6) are applicable to describe the separation efficiency in real filters. Complementing the investigations, particle recovery and filter capacity will be investigated. Recovery of particles that were retained in the filter is important to clean the filter and maintain its properties. Recovery is crucial when the retained particles are precious, since it allows to collect them in concentrated form. The investigations on the filter capacity should give experimental data on the amount of particles that can be trapped in the filter until the filtration efficiency decreases.

The possibilities of selective particle separation are investigated in Chapter 8. A requirement for selective particle separation is that pDEP separates particles more efficiently than nDEP (Sec. 4.1, Fig. 4.2). This requirement is verified in this chapter using the electric conductivity of the fluid to adjust the particle polarizability and thereby control if a particle experiences pDEP or nDEP. Another aim is to selectively separate binary particle mixtures

that contain particles of different electric conductivity.

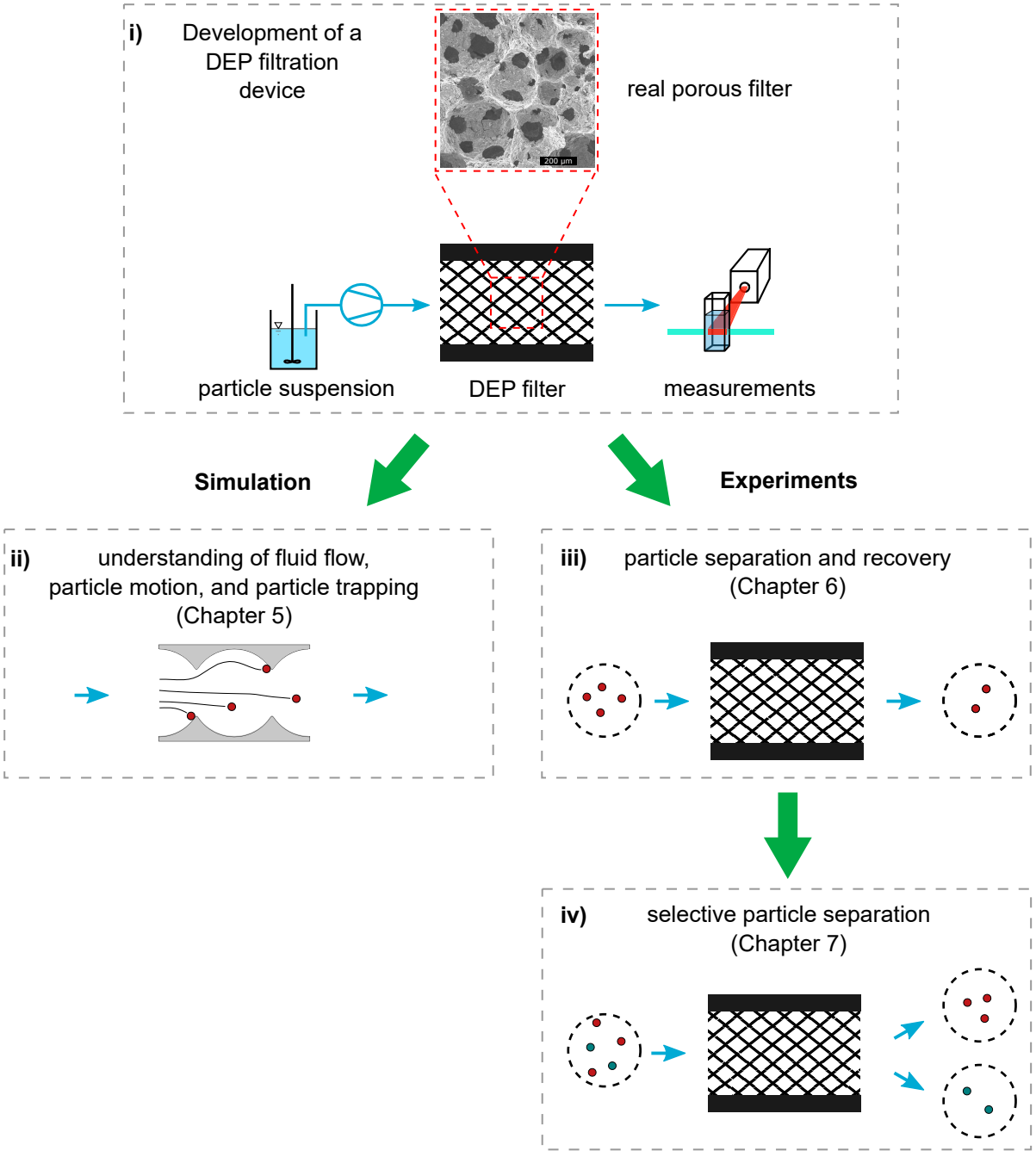

Figure 4.5: Graphical outline and workflow of this thesis.

Chapter 5

Methods and Materials

5.1 Experimental DEP filtration

This section describes the experimental setup and procedure. Some of the following parts were thoroughly described in: M. Lorenz, D. Malangré, F. Du, M. Baune, J. Thöming, and G. R. Pesch (2020). High-throughput dielectrophoretic filtration of sub-micron and micro particles in macroscopic porous materials. *Analytical and Bioanalytical Chemistry*, 412, 3903-3914. doi: 10.1007/s00216-020-02557-0. Some content of this publications will reappear in this chapter.

5.1.1 Filtration setup

A schematic of the experimental setup is shown in Figure 5.1a. The volumetric fluid flow through the DEP filter cell was driven by a peristaltic pump (REGLO Analog, Ismatec) and could be set to values between 1 and 11 $\mathrm{mL\,min^{-1}}$. A picture of the filter cell is shown in Figure 5.1b. It consists of a tapered inlet and outlet (to prevent particle accumulation) and the porous filter that is tightly sandwiched in between two stainless steel plate electrodes. A sinusoidal ac voltage was applied across the distance of 8 mm between the electrodes (using a TREK PZD700A power amplifier in combination with a Hameg HM8131 function generator) generating an electric field inside the filter medium perpendicular to the filtrate flow. The voltage was set between 150 $\mathrm{V_{RMS}}$ and 600 $\mathrm{V_{RMS}}$ at 1 kHz to 15 kHz resulting in an electric field strength between 18.75 $\mathrm{kV_{RMS}\,m^{-1}}$ and 75 $\mathrm{kV_{RMS}\,m^{-1}}$. The power required for DEP in the filter is significantly higher than the power required in most conventional microfluidic DEP devices (difference in dimension) which limited the output frequency of our current amplifier to 15 kHz to guarantee a sinusoidal voltage characteristic. The porous filter had a cross section of 8 mm × 29 mm. The filter depth in flow direction was 18 mm. The filter cell was designed to allow easy changes of the filter material. The

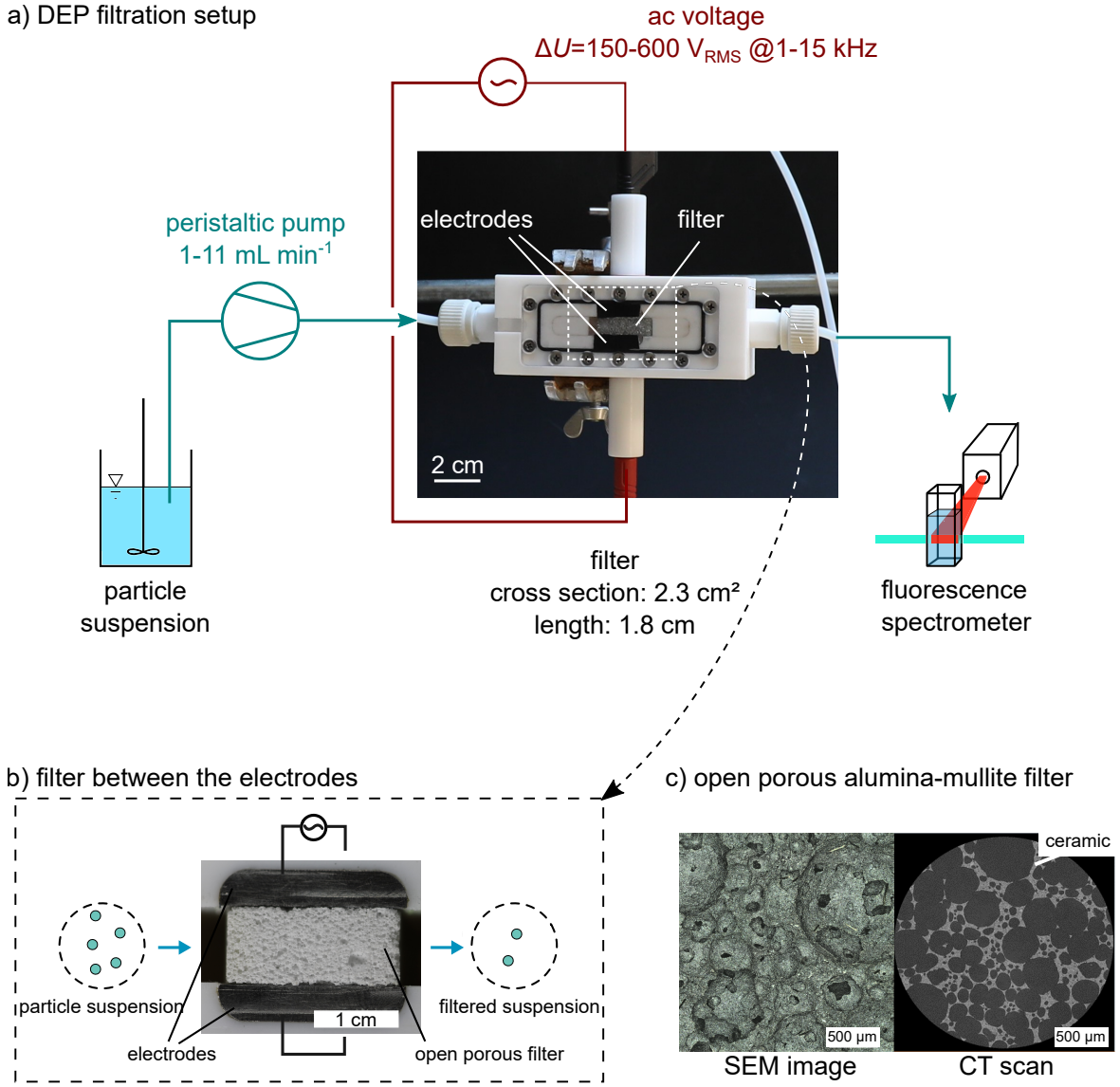

Figure 5.1: Scheme of the experimental setup with a picture of the filter cell (a). The particle suspension was constantly pumped with flow rates from 1 mL min^{-1} to 11 mL min^{-1} through the porous filter that is sandwiched in between two stainless steel electrodes. The electrodes that are placed parallel to each other with a distance of 8 mm were supplied with ac voltages of 150 V_{RMS} to 600 V_{RMS} at a frequency between 1 kHz and 15 kHz. The particle concentration at the outlet of the filter was measured by fluorescence spectroscopy. The filter has a width of 8 mm, a height of 29 mm, and a length (in flow direction) of 18 mm. A foamed alumina-mullite filter is shown enlarged in between the electrodes (b). An even closer look at the foamed alumina-mullite filter is shown in the scanning electron microscopy (SEM) image and computed tomography (CT) scan (c). (Lorenz et al., 2020)

different filters that were applied are described in Section 5.1.2. The particle concentration after the filter was determined by using a FluoroMax 4 fluorescence spectrometer (Horiba) and a quartz flow-through cuvette (176.762-QS, Hellma). This allowed to detect the fluorescence intensity signals of the filtrate online. In all experiments, the fluorescence intensity signal was linearly dependent on the particle concentration (as validated by preliminary experiments). This allowed highly accurate particle concentration measurements. The procedure of particle concentration measurements is described in Section 5.1.5. (Lorenz et al., 2020)

5.1.2 Filters

In this thesis, two kinds of filter materials were applied. The majority of experiments was performed using open porous, foamed alumina-mullite sponges. Additionally, packed beds of glass beads were used which provide a different pore geometry and surface charge.

Characterization of open porous, foamed alumina-mullite sponges

The applied open porous alumina-mullite ceramics were produced by direct foaming. Information about their fabrication is provided in Appendix B. Figure 5.1c shows two exemplary images of the pore structure (a SEM image and one slice from a CT scan). The structure shows predominantly spherical pores that are highly connected (highly open porous) by numerous pore windows with sharp thin edges. Filters with porosities of about 83% and four different structure sizes were used. Hydraulic pore diameter, volume-weighted median pore diameter, and area-weighted median pore window diameter were determined from computer tomography data by using MATLAB and the watershed algorithm implemented in the DIPimage package, version 2.9. A detailed description of the method is provided in Appendix C. The pore sizes including the isoelectric point (iep) of the material are listed in Table 5.1. The alumina-mullite ceramics have their iep between pH 4.9 (pure mullite (Hirata et al., 2016)) and 7 (pure α-alumina ((Hirata et al., 1991))).

Characterization of packed beds of glass beads

Packed beds of glass beads (fused quartz; 350 µm and 1 mm diameter) were used as porous filters. The packed beds had similar dimensions as the ceramic filters and were kept in fixed by two porous sintered glass filters (pore size 160 µm to 250 µm) that sealed the 8 mm × 29 mm gaps at the sides of fluid inflow and outflow for the glass beads. Information about the pore size are given in Table 5.1. The isoelectric point of the fused quartz lies at acidic pH values of $2-3.5$ (Kosmulski, 2001).

Table 5.1: Filter characterization. Hydraulic diameter D_h, volume-weighed median diameter $D_{p,3}$, and area-weighed median pore window diameter $D_{w,2}$ and iep of the filters.

Filter	D_h (µm)	$D_{p,3}$ (µm)	$D_{w,2}$ (µm)	iep at pH
maliS	222	320	178	4.9 – 7
maliM	255	394	178	4.9 – 7
maliL	429	617	226	4.9 – 7
maliXL	480	642	272	4.9 – 7
glass beads 350 µm	156			2 – 3.5
glass beads 1 mm	445			2 – 3.5

5.1.3 Particles and suspensions

All experiments, except the ones about electrical conductivity-selective particle separation, were done using the same type of particle suspension. **Suspension generation**: Particles were diluted in ultrapure water that had been degassed under reduced pressure (80 mbar). A small amount of Tween20 (0.01 vol%) was added to reduce particle adsorption to the filter. The electrical conductivity was adjusted with KCl to the desired value.

An overview of the particles with their concentrations, and zeta potential (at pH ≈ 6) are given in Table 5.2.

Table 5.2: Parameters of applied suspensions (particle diameter d_p, number and volumetric particle concentrations c and c_{vol}, zeta potential ζ, and isoelectric point (iep) of the particles). Sources: [1] (Wakamatsu and Numata, 1991, Menéndez et al., 1995), [2] (Kallay et al., 1987)

Particles	d_p	c (cm^{-3})	c_{vol} (vol%)	ζ at pH≈ 6 (mV)	iep at pH
PS carboxylated	500 nm	2.2×10^6	1.5×10^{-5}	< -20	< 3
PS carboxylated	1 µm	4.5×10^5	2.5×10^{-5}	< -20	< 3
PS carboxylated	2 µm	1.1×10^5	5×10^{-5}	< -20	< 3
PS carboxylated	4.5 µm	2×10^4	1×10^{-4}	< -20	< 3
Silica carboxylated	3 µm	4×10^5	5.7×10^{-6}		< 3
Graphite	3 µm	1.3×10^6	2×10^{-5}		2 – 5 [1]
Copper flakes	see text				9.8 [2]

The majority of experiments was done with monodisperse carboxylated polystyrene (PS) particles (Polysciences Fluoresbrite, YG Carboxylate Microspheres). Additionally, silica, graphite, and copper particles were used. The silica particles (Sicastar greenF labeled) were carboxylated and had a diameter of 3 µm. Graphite particles were taken from a graphite water dispersion (Graph Aqua, AMG Graphite GK) with an average diameter of about 3 µm (manufacturer's information). 50 µL of the graphite dispersion were diluted in 500 mL aqueous suspension. The copper particles (flakes) were present as a powder that was challenging to suspense in water. The suspension generation process was therefore altered from the process used for the other suspensions: They were first suspended in

a 1 vol% aqueous Tween20 solution, then shaken (by hand) and finally sonicated for 2 minutes. This suspension was then filled up with ultrapure water to contain the same amount of Tween20 (0.01 vol%) as the other particle suspensions. Again, the suspension conductivity was adjusted by adding KCl. The size distribution of the copper particles was not provided by the supplier. Microscope images (Fig. 5.2) that were taken with an upright epifluorescence microscope (Carl Zeiss Axio Scope.A1 Vario equipped with a Lumenera Infinity 3S-1URM camera) show a rather broad particle size distribution. The observed copper flake diameters are in the range of 1 µm to 100 µm. Despite the broad particle size distribution, the copper particles could be used for conductivity-selective particle separation experiments, since their conductivity is barely influenced by size.

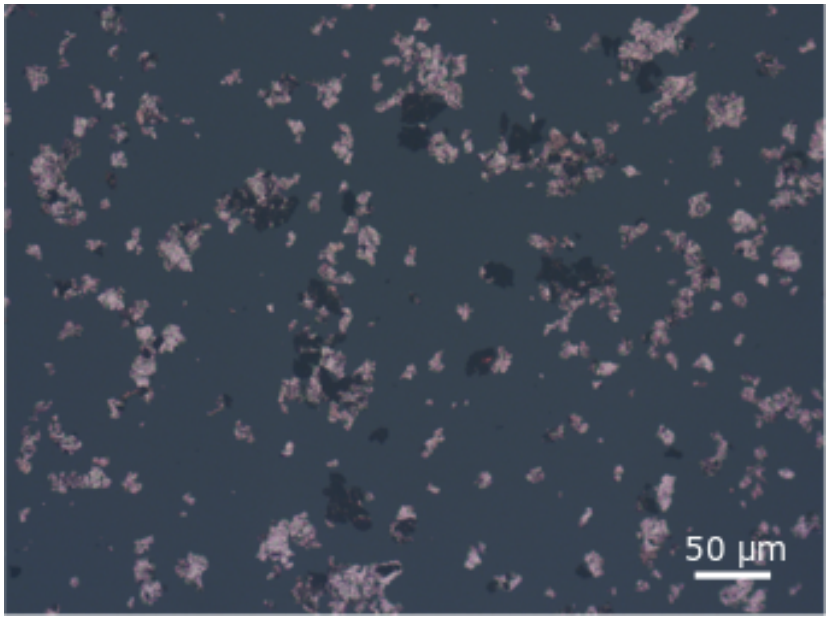

Figure 5.2: Microscopy image of copper flakes. The flakes appear very inhomogeneous in size and shape.

5.1.4 Particle electric conductivity

For DEP filtration and especially the investigations about particle conductivity-selective separation, it is important to determine the electric conductivity of the particles. In general, the particle conductivity can be assumed according to Eq. (2.33) as a function of its bulk conductivity σ_b, its surface conductance K_s, and its radius r.

Polystyrene is an electrically isolating material. Hence, the bulk conductivity of polystyrene particles is negligible. Their conductivity is only dependent on the double layer that exists at the interface between particle and its surrounding medium. At a medium conductivity below 10^{-2} S m^{-1} and a particle size equal or above 1 µm diameter, the PS particles conductivity is dominated by the Stern layer conductance which is mainly material dependent

(Ermolina and Morgan, 2005). With the surface conductance of PS particles which is usually about 1 nS (Arnold et al., 1987, Schwarz, 1962), the particle conductivity of a 4.5 µm particle is $\sigma_{p,PS} = 2K_s/a = 8.8 \times 10^{-4}\,\mathrm{S\,m^{-1}}$. However, quite different surface conductances between 0.2 nS and 2 nS have been reported for PS particles (Ermolina and Morgan, 2005, Arnold et al., 1987) resulting in a wide range of conductivities between $\sigma_{PS,4.5\mu m} = 1.7 \times 10^{-4}\,\mathrm{S\,m^{-1}}$ and $17 \times 10^{-4}\,\mathrm{S\,m^{-1}}$. The conductivities of the PS particles with diameter 500 nm, 1 µm, 2 µm, and 4.5 µm can be approximated in the same way (Tab. 5.3).

Table 5.3: Calculated values to predict the effective electric conductivities of PS and silica particles at frequencies below their relaxation frequency.

	min. conductivity ($1 \times 10^{-4}\,\mathrm{S\,m^{-1}}$)	max. conductivity ($1 \times 10^{-4}\,\mathrm{S\,m^{-1}}$)
$\sigma_{PS,0.5\mu m}$	15.3	153
$\sigma_{PS,1\mu m}$	7.7	77
$\sigma_{PS,2\mu m}$	3.8	38
$\sigma_{PS,4.5\mu m}$	1.7	17
$\sigma_{SiO2,3\mu m}$	20	40
$\sigma_{Graphite,3\mu m}$	3.3×10^6	3×10^9
σ_{Cu}		6×10^{11}

The conductivity of the silica particles is also determined by their surface conductance which is found to be in the range between 1.5 nS and 3 nS (Leroy et al., 2013). For the silica particles of 3 µm diameter this results in a particle conductivity between $20 \times 10^{-4}\,\mathrm{S\,m^{-1}}$ and $40 \times 10^{-4}\,\mathrm{S\,m^{-1}}$.

Graphite particles have much higher conductivities which are unaffected by the conductance of the double layer and only influenced by the conductivity of their bulk material graphite (at frequencies above the relaxation frequency of the electric double layer). Independent of their size, graphite particles have the conductivity of graphite which is in the range between $\sigma_{graphite} = 3.3 \times 10^2\,\mathrm{S\,m^{-1}}$ and $3 \times 10^5\,\mathrm{S\,m^{-1}}$ (Pierson, 1993).

The electric conductivity of the copper particles are also dominated by the bulk conductivity, which is $\sigma_{Cu} = 5.96 \times 10^7\,\mathrm{S\,m^{-1}}$ (Matula, 1979).

5.1.5 Experimental procedure

All experiments were done with filters that were used multiple times. To provide constant conditions for each experiment, the setup was flushed with ethanol prior to experiments, to clean the setup and wash out particles and air. Afterwards, the setup was flushed with degassed and deionized water to wash out the ethanol. Subsequently, the particle suspension was pumped into the setup. To guarantee a constant particle concentration at the inlet, the particle suspension was permanently stirred. Each measurement was

performed in three steps.

Start-up phase: The volumetric flow rate (Q) was set but no electric field was applied, and the particle concentration in the filtrate without DEP trapping was determined (c_0)(Figure 5.3). Since c_0 was determined at the filter outlet, it already contains the trapping due to mechanical trapping/depth filtration (see Sec. 5.1.6). $c_{\min}$ was therefore smaller than the particle concentration in the suspension that entered the filter c (see Tab. 5.2).

DEP trapping phase: The electric field was applied. In response, the particle concentration decreased until it reached a constant minimum ($c_{\min}$). $c_{\min}$ is reached with a delay because directly after switching on the electric field the measured filtrate only traveled parts of the filter and had a shorter retention time in it.

Recovery phase: The field was switched off, and the filter was flushed at the possible highest volumetric flow rate, $Q_{\text{rec}} = 11\,\text{mL}\,\text{min}^{-1}$, to increase shear forces to a maximum. Flushing was performed with the particle suspension. The particle concentration peaked and then fell slowly back to concentration of the start-up phase c_0. The time to reach this minimum concentration was independent of DEP-related parameters. It agreed with the particle retention time in the setup that was determined as the time between injecting a concentration jump at the filter inlet until a constant outlet concentration was reached.

Particle concentration measurements using particle fluorescence and reflection

The particle concentration after the filter was determined by using a FluoroMax 4 fluorescence spectrometer (Horiba) and a quartz flow-through cuvette (176.762-QS, Hellma). This allowed online detection of the fluorescence intensity signals from the filtrate. At the particle concentrations, that were used in this study, the fluorescence intensity signal is linearly dependent on the particle concentration (as validated by preliminary experiments, not shown), allowing highly accurate particle concentration measurements. The fluorescently labeled particles were excited at their excitation maximum and detected at their emission maximum. The concentration of the graphite and copper particles that were not labeled by a fluorescent dye was determined by detecting the reflection intensity (both are reflecting light much stronger than PS particles). To obtain a linear dependency between reflection intensity and particle concentration, the particle concentration was kept low so that the light extinction rate of the suspension was always below 0.1 (meaning at least 90% of the excitation light are going through the suspension). Calibration measurements showed that the reflection intensity was, up to this extinction rate, linearly dependent on the graphite

and copper particle concentration. The excitation and detection wavelength for reflection measurements was typically 600 nm. If not mentioned differently, the concentration measurements were done by using the wavelengths shown in Tab. 5.4. In measurements when particles of different type were involved, the wavelengths had to be adapted so that each emission/reflection signal was only dependent on the concentration of one particle type.

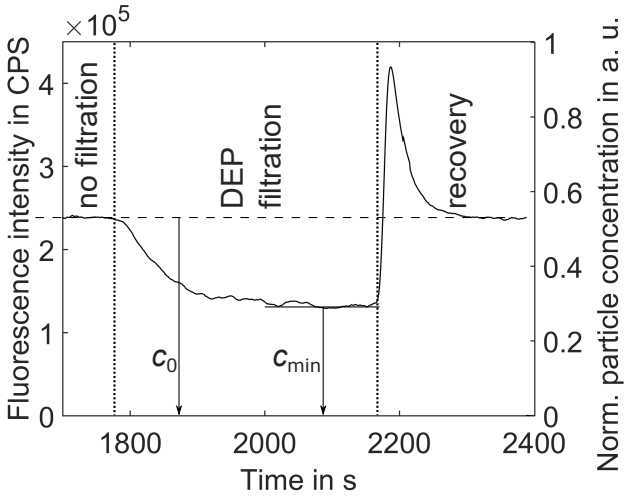

Figure 5.3: An exemplary plot of the fluorescence intensity in counts per second (CPS)/normalized particle concentration for one measurement cycle. The particle concentration at the outlet of the filter is measured by fluorescence spectroscopy. The fluorescence signal is linearly dependent on the particle concentration c, and the separation efficiency was defined as $\eta = (c_0 - c_{\min})/c_0$. Here, c_0 is the normalized particle concentration when no electric field is applied, and $c_{\min}$ is the minimum normalized concentration detected when the field is applied. In this example, the flow rate during recovery was 5.5 times as high as the flow rate during DEP filtration and the particle recovery rate R for this specific experiment was 82%.

Table 5.4: Excitation and emission wavelengths for the differently labeled fluorescent and reflecting particles that were used for particle concentration measurements.

Particles	excitation (nm)	emission (nm)
YG labeled PS particles (Fluorescbrite)	441	486
BB labeled PS particles (Fluorescbrite)	360	407
green-F labeled silica particles (Sicastar)	485	510
Graphite particles (not labeled)	600	600
Copper particles (not labeled)	600	600

5.1.6 Definition of characteristic measures

Depth filtration/mechanical separation efficiency

Particles are filtered from the fluid even without an electric field. They are transported to the inner surface of the filter by sedimentation, interception, inertia, and hydrodynamic

forces and immobilized at the inner surface due to electrostatic and van der Waals forces as well as wedging or straining (Johnson et al., 2010). These mechanical mechanisms are discussed in more detail in Section 3. For each filter, the mechanical separation efficiency η_{mech} was determined by measuring and comparing the particle concentration at the filter outlet c_{out} (with no electric field applied) to the concentration at the filter inlet c_{in}.

$$\eta_{\mathrm{mech}} = \frac{c_{\mathrm{in}} - c_{\mathrm{out}}}{c_{\mathrm{in}}} \tag{5.1}$$

Dielectrophoretic separation efficiency

The dielectrophoretic separation efficiency (η) was defined as the number of particles that was trapped in the filter by the electric field, normalized by the number of particles that would exit the filter without electric field,

$$\eta = \frac{c_0 - c_{\mathrm{min}}}{c_0}. \tag{5.2}$$

It is not dependent on mechanical trapping because $c_0 = c_{\mathrm{out}}$ already accounts for mechanical trapping effects.

Recovery rate

The particle recovery rate R describes the proportion of dielectrophoretically trapped particles that can be recovered when the electric field is switched off and the filter flushed. The amount of trapped particles was determined by multiplying the temporal integral between c_0 and filter outlet concentration over the time of DEP trapping A_{trap} (Fig. 7.6) with the applied volumetric flow rate Q_{trap}. The amount of recovered particles was calculated analogously for the time of recovery with the integral A_{rec} and the flow rate Q_{rec}. Thus, the particle recovery rate was calculated by

$$R = \frac{A_{\mathrm{rec}} Q_{\mathrm{rec}}}{A_{\mathrm{trap}} Q_{\mathrm{trap}}}. \tag{5.3}$$

The volumetric flow rate for recovering the particles from the filter Q_{rec} was always set to $11\,\mathrm{mL\,min^{-1}}$.

Filter capacity

In this study, the filter capacity is described by the number of particles that can be trapped in the filter until the separation efficiency decreases to 60.6% of the initial (i. e., maximum) trapping efficiency. This separation efficiency is reached after $\tau/2$, with the relaxation time (τ) after which the trapping efficiency decreases to 36.8% of the initial value.

5.2 Simulations of electric field and fluid flow in a model filter cell

Simulations were done with COMSOL Multiphysics® software to model the electric field, the fluid flow, and the fluid mixing in model filter cells.

5.2.1 Geometry of the model filter cell

The geometry of the three-dimensional model filter cell was kept as simple as possible. The cross section of the filter cell (axisymmetric around the dot-dash line) is exemplary shown in Figure 5.4. It covers in total a length of 2 pores (half a pore as entrance, a full pore in the middle, and half a pore as exit). Spherical pores with diameters $D_p = 150\,\mu m$, $300\,\mu m$, and $600\,\mu m$ and circular pore windows with diameters according to $D_w = 1/2 D_p$ were assumed. These model cell diameters are of the same size as the averaged diameters of the real filters (Tab. 5.1). To avoid an unrealistically sharp edge at the pore windows (that would lead to calculation issues because of a singularity), the edge was rounded to a $2\,\mu m$ radius. This led to an actual pore window diameter slightly bigger than $D_w = 1/2 D_p$.

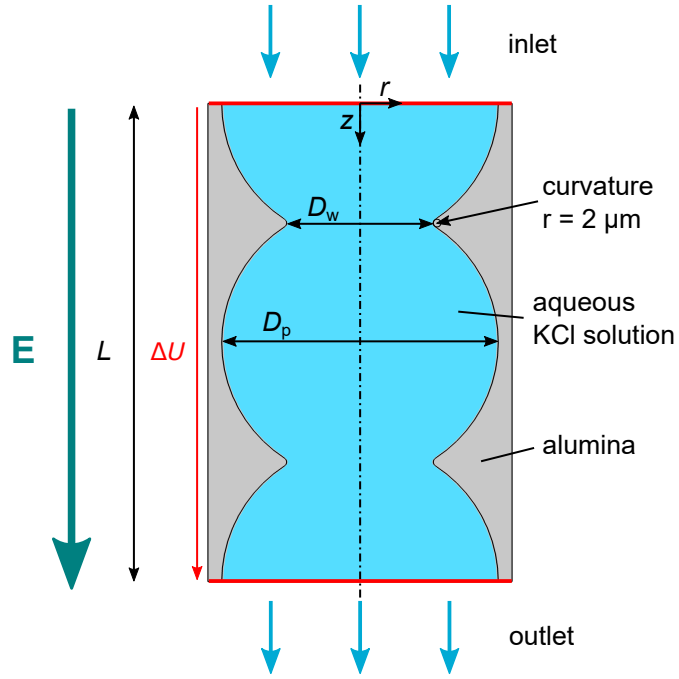

Figure 5.4: Model filter cell used for simulations (axial section, dot-dashed symmetry line).

5.2.2 Equations and boundary conditions

Because the model cell geometry is axisymmetric, the two-dimensional axisymmetric calculation models, provided by COMSOL Multiphysics®, were applied.

Electric field calculation

The electric field was calculated by using the *electric currents* physics package which are content of the ACDC module. Homogeneous materials and a charge-free space were assumed so that the Poisson equation (2.8) to calculate the electric potential simplifies to Laplace's equation, $\nabla^2 \Phi = 0$. Uniform potentials along the upper and lower boundary of the model cell (separated by the distance L) were assumed. The potential difference between both edges ΔU was chosen to generate the intended electric field strength. In order to match the applied electric field strength of the experiments, the potential difference was calculated by

$$\Delta U = E_{0,\mathrm{exp}} L,$$

with the applied electric field strength of the experiments $E_{0,\mathrm{exp}} = \Delta U_{\mathrm{exp}} / L_{\mathrm{filter}}$, where the applied voltage at the electrodes of the experimental filter cell is ΔU_{exp} and the distance between the electrodes is L_{filter}. The left and right boundaries for the simulations were chosen to be ideally isolating. The electric permittivities of the aqueous KCl suspension and alumina were assumed to be $\varepsilon_{\mathrm{water}} = 80.2$ and $\varepsilon_{\mathrm{Al_2O_3}} = 9.1$.

Fluid flow calculation

The fluid flow of the aqueous solution was calculated with COMSOLS *laminar flow* physics package of the microfluidics module. The fluid flow was determined by solving the Navier-Stokes equation for an incompressible fluid assuming a global pressure of $p = 1\,\mathrm{bar}$, laminar flow conditions, and a no slip boundary condition at the wall surface (velocity at the wall $v_{\mathrm{wall}} = 0\,\mathrm{m\,s^{-1}}$). Further, the velocity along the inlet boundary was assumed to be fully developed, while the boundary condition at the outlet was given by a pressure of $p_{\mathrm{out}} = 1\,\mathrm{bar}$. The flow direction through in- and outlet was assumed to be vertical/normal to the boundaries.

Induced-charge electroosmosis (ICEO) flow calculation

In addition to the pressure-driven fluid flow, the induced-charge electroosmotic flow was calculated following a model presented by Wang et al. (2017) based on a derivation by Zhao (2011). The induced wall potential can be determined in three steps.

i) Calculation of the electric field (see above).

ii) Calculation of the dimensionless parameter K_{ICEO} that governs the induced potential magnitude (Wang et al., 2017)

$$K_{\mathrm{ICEO}} = \tilde{\lambda}\tilde{r}_{\varepsilon} \frac{i\tilde{\omega}\tilde{r}_{\mathrm{t}} + 1}{i\tilde{\omega}\tilde{r}_{\mathrm{t}}(i\tilde{\omega}+1)^{3/2}}. \tag{5.4}$$

The dimensionless values are given as

$$\tilde{r}_\varepsilon = \frac{\varepsilon_{Al_2O_3}}{\varepsilon_{water}} \qquad \text{ratio wall to fluid permittivity}$$

$$\tilde{r}_t = \frac{\varepsilon_{Al_2O_3}}{\sigma_{Al_2O_3}} \frac{\sigma_{water}}{\varepsilon_{water}} \qquad \text{ratio wall to fluid relaxation times}$$

$$\tilde{\lambda} = \frac{\lambda_D}{D_p} \qquad \text{dimensionless Debye length}$$

$$\tilde{\omega} = \frac{f}{t_{water}^{-1}} = \frac{f\varepsilon_{water}}{\sigma_{water}} \qquad \text{dimensionless electric field frequency}$$

iii) Calculation of the dimensionless zeta potential. The potential jump from the solid wall (Φ_{wall}) to the fluid outside of the double layer (Φ_f) can be related to dimensional form (Zhao, 2011)

$$\tilde{\Phi}_{wall} + \tilde{K}_{ICEO} \nabla \tilde{\Phi}_{wall} \cdot \mathbf{n} = \tilde{\Phi}_f, \tag{5.5}$$

where the unit vector normal to the wall surface is $\mathbf{n}$. The dimensionless potentials are defined as $\tilde{\Phi} = \Phi/(E_0 D_p)$ with the global electric field strength at uniform channel cross section $E_0 = \Delta\Phi/L$ (here Δ is the difference not the Laplace operator!) and the pore diameter D_p. The zeta potential calculates as

$$\zeta = (\tilde{K}_{ICEO} \nabla \tilde{\Phi}_{wall} \cdot \mathbf{n}) E_0 D_p . \tag{5.6}$$

Subsequently, the ICEO velocity at the wall can be calculated with the ICEO mobility $\mu_{ICEO} = \varepsilon_{water}\zeta/\mu$ (dependent on the position at the wall) and the electric field tangential to the wall $E_{||}$.

$$v_{ICEO} = \mu_{ICEO} E_{||} \tag{5.7}$$

In the COMSOL model these values were implemented as wall boundary conditions in the laminar flow calculation.

Chapter 6

A theoretical evaluation of DEP filtration

Before turning towards the experimental investigations of this thesis, this chapter gives a theoretical and thus predictive evaluation of DEP filtration in depth filters. The aim is to give a detailed overview about the mechanisms that influence particle motion and trapping in the filter. It provides the basis to discuss the experiments of the next chapters.

The first section of this chapter assesses the relevance of depth filtration (mechanical) trapping mechanisms for DEP filtration. It discusses capture mechanisms that lead to particle transport to the filter surface and interaction of particles with the filter surface. The second section focuses on how particles are trapped by DEP in a depth filter. This section is not only describing mechanisms but simulation are used to calculate electric field (gradient) and fluid flow in a model filter cell, which are subsequently used to study particle motion and particle trapping.

6.1 Particle trapping by depth filtration effects

Depth filtration effects can cause significant particle trapping in DEP filtration processes. However, in most DEP filtration processes particle trapping by depth filtration is unintended because it also traps non-target particles. This is problematic because it reduces the selectivity of DEP filtration processes significantly. In this section, the influence of depth filtration is evaluated for the conditions that were applied in experiments. The depth filtration trapping rate is determined by the rate of particles hitting the filter wall and the probability that particles adhere permanently to the wall once they hit it. In the following subsections particle capture and adhesion are assessed.

6.1.1 Particle capture

The mechanisms that lead to particle capture (transport to the filter surface) were described in Sec. 3.1. In the following the the significance of these capture mechanisms is hypothesised.

Inertial impaction. Inertial impaction between particles and filter can occur when particles are incapable to follow the fluid stream lines due to their inertia. The maximum Stokes number (Eq. (3.1)) in the experiments of this thesis is $\mathrm{St} = 5 \times 10^{-4}$ (assuming spherical copper particles of diameter $d_\mathrm{p} = 4.5\,\mu\mathrm{m}$, with a density of $\rho_\mathrm{p,Cu} = 8960\,\mathrm{kg\,m^{-3}}$, a flow velocity of $v_\mathrm{fluid} = 1\,\mathrm{mm\,s^{-1}}$, and an obstacle dimension of $L = 100\,\mu\mathrm{m}$). For a Stokes number much smaller than 1 it can be assumed that inertial impaction has negligible influence on particle retention in the filter (Friedlander, 2000).

Sedimentation and buoyancy. In the experiments of this work the dimensionless number that characterizes the significance of sedimentation and buoyancy ($d_\mathrm{p}^2(\rho_\mathrm{p} - \rho_\mathrm{m})g)/(18\mu v_\mathrm{fluid})$ (Eq. (3.2)) is typically much smaller than 1 because the density of polystyrene particles ρ_p is almost the same as the density of water ρ_m. This indicates that sedimentation and buoyancy have low impact on the rate of mechanical particle capture in the filter. However, in structures that contain flow "dead zones" of very low flow velocities sedimentation can still be relevant.

For copper particles with a density of $\rho_\mathrm{p,Cu} = 8960\ \mathrm{kg\,m^{-3}}$ (used in Sec. 8.3.3) and a maximum diameter of $d_\mathrm{p} = 10\ \mu\mathrm{m}$ sedimentation is relevant. In this case the dimensionless number is close to 1, $(d_\mathrm{p}^2(\rho_\mathrm{p} - \rho_\mathrm{m})g)/(18\mu v_\mathrm{fluid}) = 0.6$ (with $\rho_\mathrm{m,water} = 1000\ \mathrm{kg\,m^{-3}}$, $\mu_\mathrm{water} = 10^{-3}\mathrm{kg\,m^{-1}s^{-1}}$, and the minimum average fluid velocity used in the filter $v_\mathrm{fluid} = 90\,\mu\mathrm{m\,s^{-1}}$).

Interception. Particles are intercepted when particles move along a fluid stream line that gets as close as one particle radius or closer to the filter surface. The common way to predict the relevance of interception is to determine the ratio of particle diameter and hydraulic diameter of the filter $d_\mathrm{p}/d_\mathrm{h}$. In this work this ratio is smaller than 2×10^{-2} (maximum particle diameter $d_\mathrm{p,max} = 4.5\,\mu\mathrm{m}$, minimum hydraulic pore diameter $d_\mathrm{h,min} = 222\ \mu\mathrm{m}$) so that interception is expected to be negligible. Only for the copper flakes, with diameters up to 50 µm, a significant amount of particles is assumed to touch the filter surface due to interception.

Straining. Straining occurs when a particle in the feed is larger than the pore or constriction through which it attempts to pass. The filters used in this study have

average pore window diameters (smallest constriction diameter between two connected pores) that are at least two orders of magnitude greater than the particle diameters, preventing straining.

Diffusion. Brownian motion can transport particles to the filter surface when they are in the vicinity of the filter surface. The transport mechanism is characterized by the Peclet number $\mathrm{Pe} = (d_\mathrm{p} v_\mathrm{fluid})/(D_\mathrm{BM})$ (Eq. (3.3)). In this work the Peclet number is mostly bigger than 10 (smallest particle diameter $d_\mathrm{p} = 500\,\mathrm{nm}$, smallest average fluid velocity $\bar{v}_\mathrm{fluid} = 90\,\mu\mathrm{m\,s}^{-1}$) indicating a low influence of particle diffusion.

6.1.2 Particle adhesion to the wall and particle agglomeration

Particle adhesion to the wall and to each other (agglomeration) substantially influence the particle trapping rate in a depth filter. The adhesion force depends on the charge in the double layers (DLs) of the involved surfaces (Sec. 3.2). Information about particle DL charge and filter DL charge are given in Tab. 5.2 and Tab. 5.1. The zeta potential was only determined for PS particles. The other particle DL charges are characterized by the isoelectric point (iep). If the suspensions pH value is equal to the iep, the particle double layer is neutral. If the suspensions pH value is below/above the iep, a particle possesses a positive/negative surface charge.

Most experiments of this work were done with PS particles in alumina-mullite filters at a pH value of 6. At a pH value of 6, PS particle possess a negative surface charge which prevents particle agglomeration. The iep of alumina-mullite is between pH 4.9 and pH 7. At pH 6 the zeta potential of the filter is expected to be close to zero, facilitating particle deposition. Adding the surfactant Tween20 to the suspension is expected to add negative charges to the filter surface, which decreases adhesion of particles. Silica and graphite particles have also negative surface charges at pH 6 so that they are expected to show a similar behaviour as PS particles. The combination of copper particles and a glass bead filter is expected to lead to strong particle adhesion to the filter. While copper has a positively charged DL, glass has a negatively charged DL.

6.2 Simulation of particle trapping conditions in a model porous filter cell

The aim of this section is to investigate the influence of key parameters (fluid throughput, applied electric field strength, filter pore size) on particle motion and trapping. To assess the trapping conditions in the DEP filter, fluid flow and $\nabla|\mathbf{E}|^2$ are simulated in a model filter cell. Subsequently, these simulations are used to calculate particle trajectories in the DEP filter. These calculated trajectories are used to determine the sensitivity towards key process parameters (fluid velocity, applied voltage, pore size) on the particle trapping efficiency.

The applied model filter cell is described in Sec. 5.2.1. It exhibits the key features of the ceramic filter which is used for the majority of the experiments on DEP filtration in this work. Thus, the simulations model allows to assess the trapping conditions in a small segment of the DEP filter. Models and boundary conditions used for simulations are described in Sec. 5.2. All parameters were chosen to be comparable to the experimental parameters.

6.2.1 Simulation of the gradient of the squared electric field

Studying the distribution of the gradient of the squared electric field ($\nabla|\mathbf{E}|^2$) in the filter is crucial because it shows where the DEP force on particles is strongest and to which direction particles move ($v_{\mathrm{DEP}} = \mu_{\mathrm{DEP}}\nabla|\mathbf{E}|^2$). Simulations of $\nabla|\mathbf{E}|^2$ for three different pore and pore window diameters (a, b, and c) and three different electric field strengths (d, e, and f) are shown in Fig. 6.1. Pore diameter and pore window diameter were scaled by the same factor so that the geometry remained the same, while the size of the entire structure changed.

The simulations show an increasing $\nabla|\mathbf{E}|^2$ with increasing voltage and decreasing structure size. The maxima of $\nabla|\mathbf{E}|^2$ are located at the edges of the pore windows and $\nabla|\mathbf{E}|^2$ decreases with increasing distance from the pore window (constriction) edges. The minima of $\nabla|\mathbf{E}|^2$ are in the center of the pores. To quantify the scaling of $\nabla|\mathbf{E}|^2$ with structure size and applied voltage its volume-average of (in the void volume) $\overline{\nabla|\mathbf{E}|^2}$ was calculated. It is shown on the bottom of each graph. $\nabla|\mathbf{E}|^2$ increases proportional to the applied electric field strength squared. Further, $\nabla|\mathbf{E}|^2$ is almost proportional to the inverse of the structure size. Fig. 6.1a, b, and c show a minor deviation from this scaling. It is caused by the rounding of the constrictions, which were kept constant in agreement with experimental filters (the edge rounding radius is material dependent).

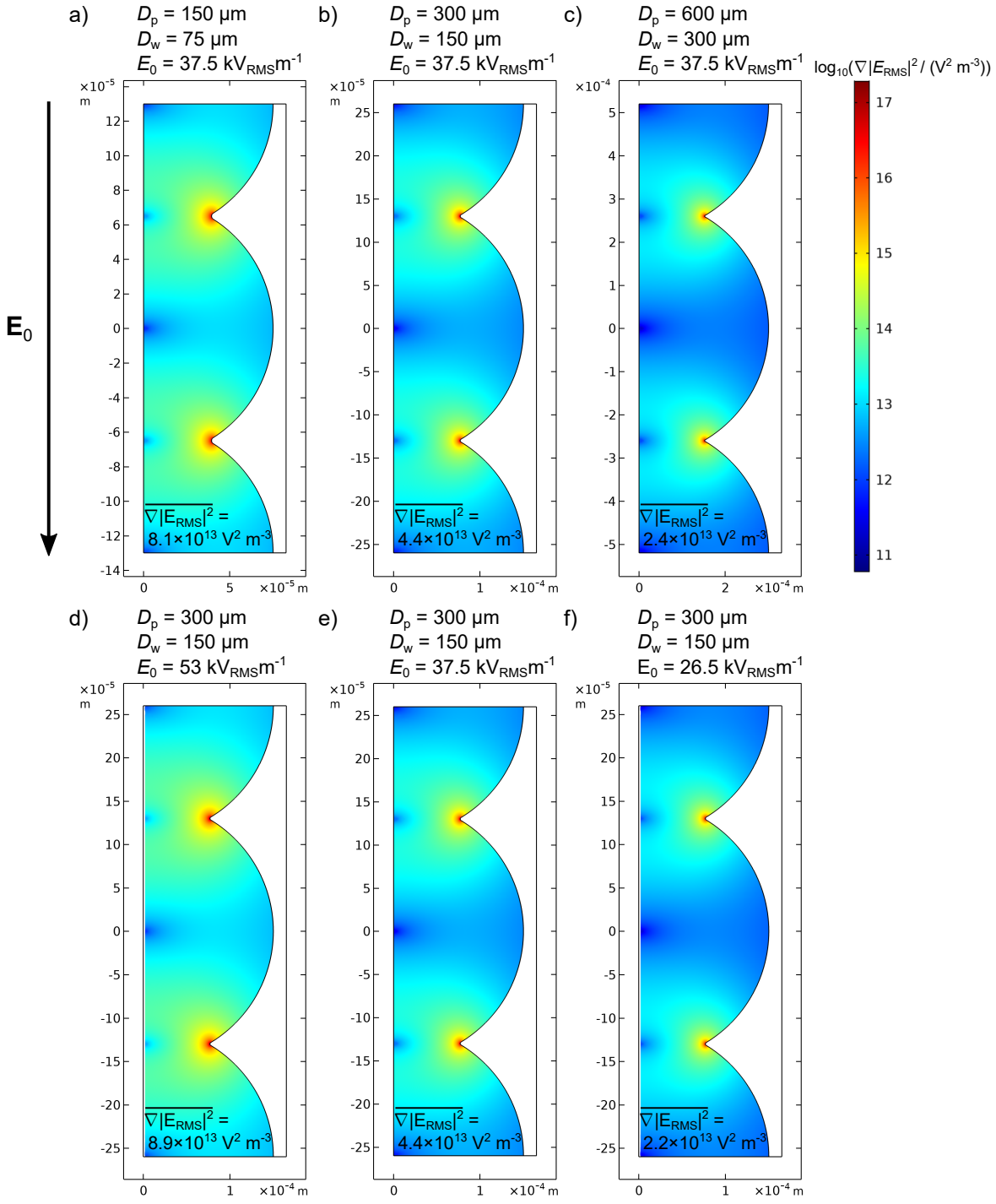

Figure 6.1: Distribution of $\nabla|\mathbf{E}|^2$ in the model filter cell. The applied electric field strengths were $E_0 = 53\,\mathrm{kV_{RMS}\,m^{-1}}$, $E_0 = 37.5\,\mathrm{kV_{RMS}\,m^{-1}}$, and $E_0 = 26.5\,\mathrm{kV_{RMS}\,m^{-1}}$, matching the field strengths applied in experiments.

6.2.2 Simulation of the fluid flow

The second force crucial for particle motion in the filter is the drag force exerted by the fluid. It depends on the fluid velocity in the filter which is studied in this section. Pressure-driven and induced charge electroosmosis (ICEO)-driven fluid flows are simulated. Pressure-driven fluid flow accounts for the flow that is caused by the pump. ICEO-driven fluid flow is produced at the interface of filter and fluid due to an inhomogeneous electric field (see Sec. 2.6.3). Electrothermal flow is neglected because it has a comparably low influence on low conductive fluids.

Pressure-driven fluid flow

Simulations of the fluid flow were computed for the minimum and the maximum fluid velocities used in experiments. The minimum and maximum superficial fluid velocities were calculated as $90\,\mu m\,s^{-1}$ and $810\,\mu m\,s^{-1}$, respectively. They were derived from the minimum and maximum volumetric flow rates ($1\,mL\,min^{-1}$ and $9\,mL\,min^{-1}$), considering a porosity of 0.8 and a filter cross section of 8 mm × 29 mm.

For fluid flow simulations it is important to know if the flow is laminar or turbulent beforehand, since these conditions determine the simulation model. The flow conditions of a fluid are characterized by the dimensionless Reynolds number which gives the ration between inertial force and viscous shear force,

$$\mathrm{Re} = \frac{\rho\, v_{\mathrm{fluid}}\, L}{\mu}. \tag{6.1}$$

Here, the density, the dynamic viscosity, and the average velocity of the fluid are given by ρ, μ, and v_{fluid}, respectively. L is the characteristic length of the channel or structure that the flow is passing. For a porous structure it is common to use the hydraulic diameter d_{h} as the characteristic length scale. As a working rule the Reynolds number in microfluidic devices is well below 1000 and thus laminar (above 1000 the flow starts to transit from laminar flow to turbulent). The highest Reynolds number of the experiments of this thesis is approximated as $\mathrm{Re}_{\mathrm{max}} = 5.5 \times 10^{-1}$ (with $v_{\mathrm{fluid,max}} = 1\,mm\,s^{-1}$ and $d_{\mathrm{h,max}} = 480\,\mu m$). Consequently, the the flow conditions are always laminar (Darcy flow).

The fluid velocity distribution in the porous structure with a pore diameter of $300\,\mu m$ and a pore window diameter of $150\,\mu m$ for the flow velocity extremes are shown in Fig. 6.2. The white lines represent fluid stream lines that start at 10 equally distanced positions at the inlet. Fluid velocity decreases with increasing distance from the center. In axial direction it shows maxima at the pore windows where the “channel” cross section in flow direction is smallest. The lowest fluid velocities are in the regions towards the filter wall where the pores are widest.

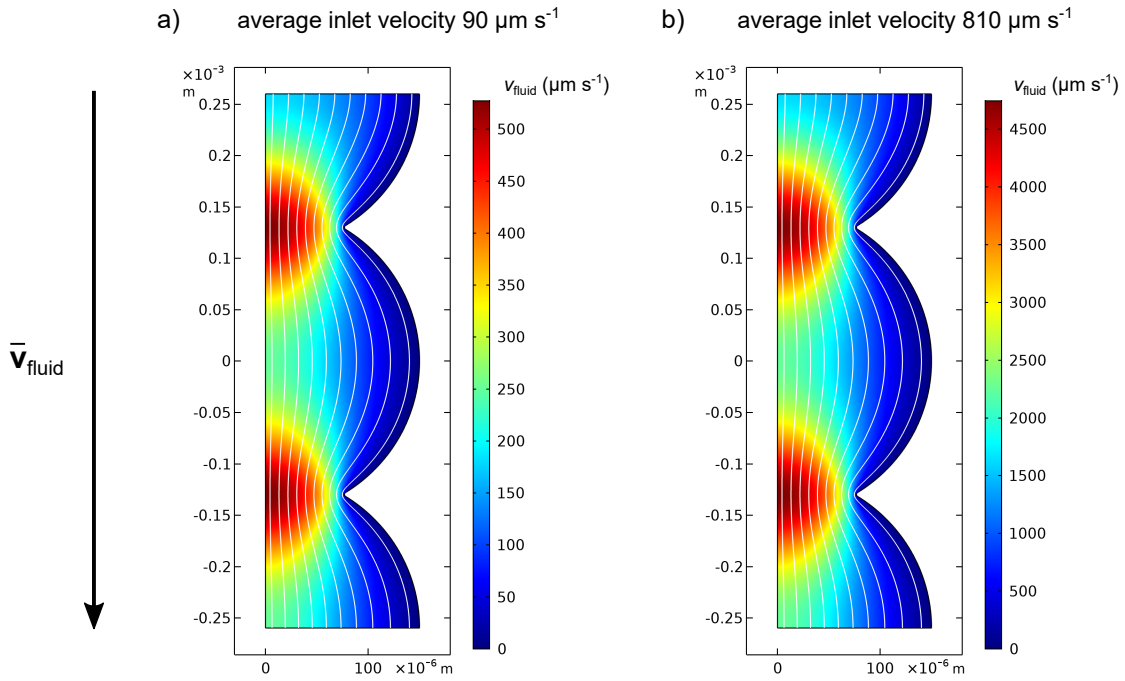

Figure 6.2: Distribution of the fluid velocity (v_{fluid}) in the model filter cell of 300 µm pore diameter and 150 µm pore window diameter. The fluid flow is directed from top to bottom. The average inlet velocity ($\bar{\mathbf{v}}_{\text{fluid}}$) of the developed velocity profile at the inlet are 90 µm s^{-1} and 810 µm s^{-1}

ICEO-driven fluid flow

Wang et al. (2017) showed that the flow in porous microstructures can be strongly influenced by induced-charge electroosmosis (Sec. 2.6.3) especially at sharp edges, narrow constrictions, and low ionic concentrations. For DEP filtration these conditions apply. In the ceramic filter structures sharp edges are found at the pore windows where an ICEO flow towards the pore center is produced. In Fig. 6.3 the simulated ICEO velocities are shown for different structure sizes and applied electric field strengths. The maximum ICEO velocities occur at the edges of the pore windows where the flow is directed towards the center of the pore window (indicated by the arrows). In the pore center the ICEO-driven flow approaches from all sides and divides in vertical direction. It leads to vorticies which are visualised by the white arrows that show direction and dimension (arrow length) of ICEO-driven fluid velocity. The ICEO-driven flow velocities are proportional to the applied electric field strength squared. The volume-averaged ICEO-driven flow velocities at $E_0 = 18.75\,\mathrm{kV_{RMS}\,m^{-1}}$, $E_0 = 37.5\,\mathrm{kV_{RMS}\,m^{-1}}$, and $E_0 = 75\,\mathrm{kV_{RMS}\,m^{-1}}$ and otherwise constant parameters are $1.9\,\mu\mathrm{m\,s^{-1}}$, $7.7\,\mu\mathrm{m\,s^{-1}}$, and $31.0\,\mu\mathrm{m\,s^{-1}}$ (Fig. 6.3 a-c). The impact of pore diameter and pore window diameter on the ICEO-driven velocity is comparably small. This shows from the volume-averaged ICEO-driven flow velocities, which are $9.4\,\mu\mathrm{m\,s^{-1}}$, $7.7\,\mu\mathrm{m\,s^{-1}}$, and $6.3\,\mu\mathrm{m\,s^{-1}}$ in pores of 600 µm, 300 µm, and 150 µm, respectively (Fig. 6.3 d-f). The difference in ICEO-driven velocities for these cases, arise from the fact that the constriction ratio (maximum pore cross section divided by the pore window cross section) in the model filter geometry was effectively higher with increasing structure size. When the edge rounding diameter was scaled with the rest of the filter structure size instead, the volume-averaged ICEO-driven velocities was independent of the structure size.

The simulations indicate that ICEO-driven velocities are usually smaller than the pressure-driven velocities used in this work ($90\,\mu\mathrm{m\,s^{-1}}$ to $810\,\mu\mathrm{m\,s^{-1}}$). However, at electric field strengths of $75\,\mathrm{kV_{RMS}\,m^{-1}}$ they can be of the same order of magnitude.

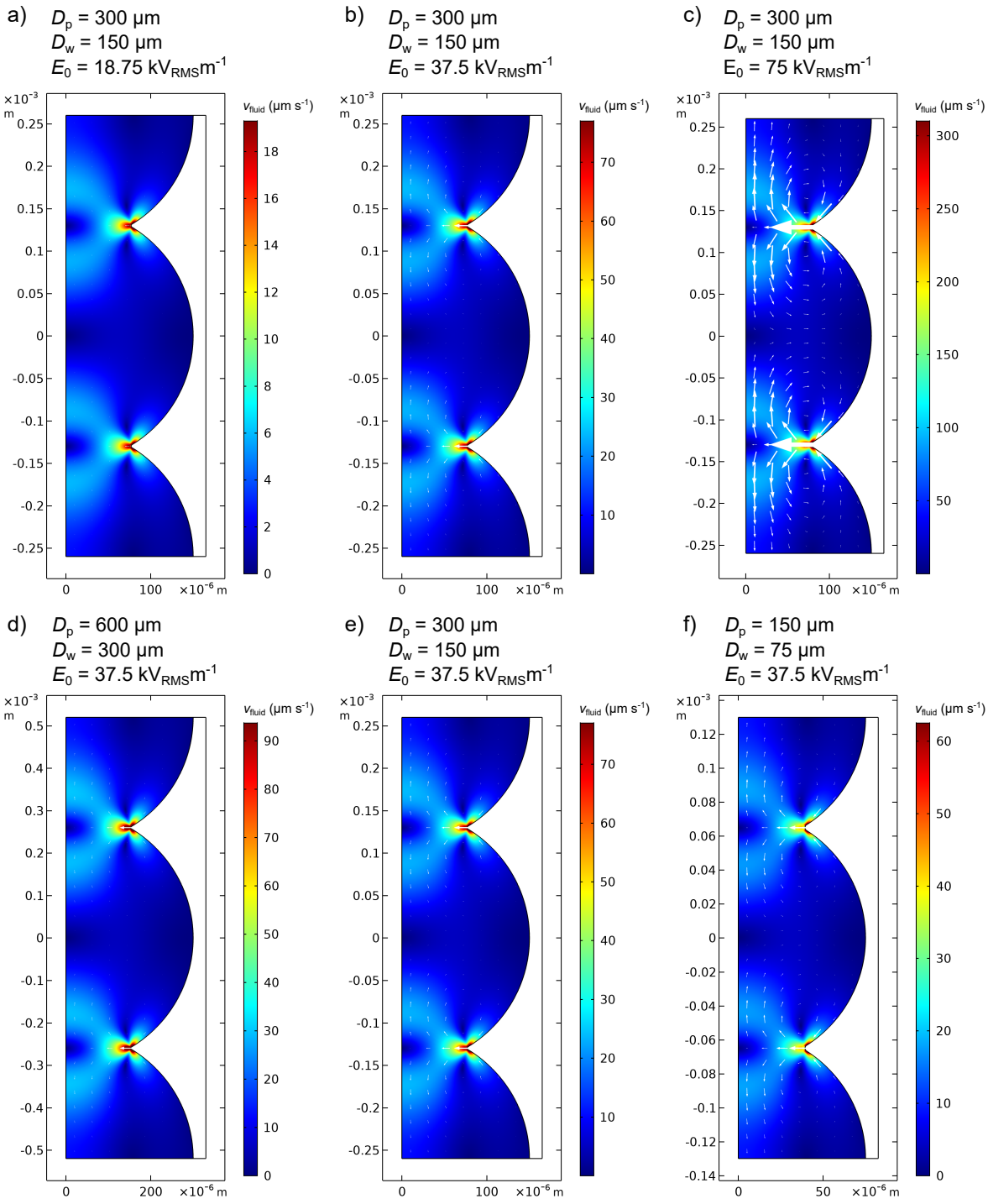

Figure 6.3: Simulated distribution of ICEO velocity (ICEO-driven only!) in model filter cells. Electric field strengths of $E_0 = 18.75\,\mathrm{kV_{RMS}\,m^{-1}}$, $E_0 = 37.5\,\mathrm{kV_{RMS}\,m^{-1}}$, and $E_0 = 75\,\mathrm{kV_{RMS}\,m^{-1}}$ (a-c) and different structure sizes (d-f) were applied. The arrows visualize the direction and magnitude of the ICEO velocity. Some arrows are very small so that they might not be visible. The fluid electric conductivity for all calculations was $\sigma_m = 2 \times 10^{-4}\,\mathrm{S\,m}$.

Pressure-driven and ICEO-driven fluid flow combined

Figure 6.4 shows a simulation that combines pressure-driven and ICEO-driven fluid flow and the resulting stream lines (at a pore diameter of $D_p = 300\,\mu m$ and a pore window diameter of $D_w = 150\,\mu m$). The average fluid velocity at the inlet is $\bar{v}_{fluid} = 90\,\mu m\,s^{-1}$ and the applied electric field strengths are $0\,kV_{RMS}\,m^{-1}$, $37.5\,kV_{RMS}\,m^{-1}$, and $75\,kV_{RMS}\,m^{-1}$. The flow velocities are very similar to the velocities of a purely pressure-driven flow (Fig. 6.2). At $75\,kV_{RMS}\,m^{-1}$, ICEO pushes the stream lines noticeable towards the center of the pore window. This leads to an increased fluid velocity in the center of the flow and a region of very low flow velocities behind the pore window.

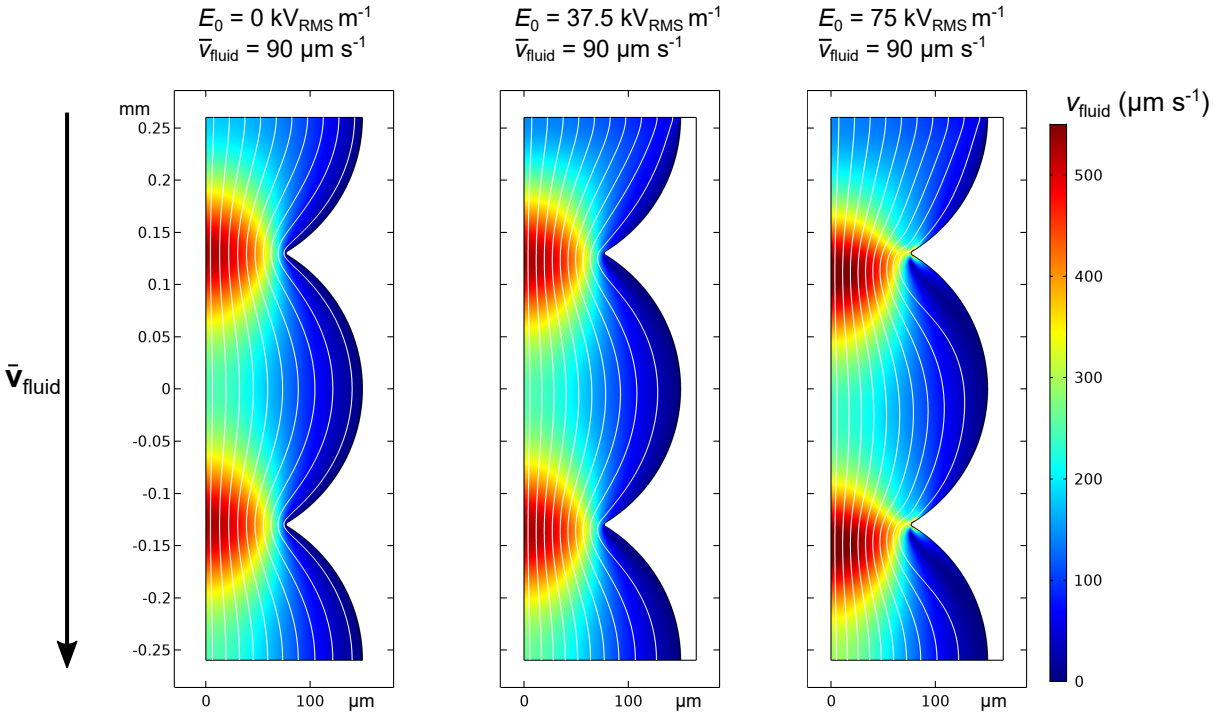

Figure 6.4: Fluid velocity and stream lines considering pressure-driven and ICEO-driven flow.

6.2.3 Simulation of particle trapping in DEP filtration

In this section, electric field and fluid flow simulations are used to calculate particle trajectories in a DEP filter. These trajectories will show how particles move through the pores and how they are trapped. The calculations are further used to predict the scaling of the particle trapping efficiency η with key parameters (applied voltage, fluid velocity, and pore diameter).

Particle motion is mainly influenced by the drag force exerted by the fluid and DEP force. Particle inertia is negligible, since the particle Stokes number is always much smaller than 1 (Sec. 3.1) meaning that the particles instantly reach their terminal velocity. Therefore, the particle velocity ($\mathbf{v}_\mathrm{p}$) can in good approximation be calculated as sum of fluid and DEP velocity,

$$\mathbf{v}_\mathrm{p} = \mathbf{v}_\mathrm{fluid} + \mathbf{v}_\mathrm{DEP}\,. \tag{6.2}$$

The fluid velocity $\mathbf{v}_\mathrm{fluid}$ was determined by considering pressure-driven and ICEO-driven flow (Sec. 6.2.2). The particle DEP velocity was calculated with Eq. (2.38) as $\mathbf{v}_\mathrm{DEP} = \mu_\mathrm{DEP}\nabla|\mathbf{E}|^2$. As model particles PS particles with 4.5 µm diameter were used. Assuming a CM factor of $f_\mathrm{CM} = 0.3$, the DEP mobility calculates as $\mu_\mathrm{DEP,PS4.5\mu m} = 1.66 \times 10^{-18}\,\mathrm{m^4 V^{-2} s^{-1}}$.

Figure 6.5 shows 10 particle trajectories (black lines) in model filter cells of different pore diameter and pore window diameter at different average fluid velocities $\bar{v}_\mathrm{fluid}$ and different electric field strengths E_0. The trajectories start at the inlet (top) at equidistant radial positions. Further, the graphics show the spatially resolved ratio of $v_\mathrm{DEP}/v_\mathrm{fluid}$. This ratio indicates whether fluid flow or DEP has a stronger impact on particle motion. The red line represents the border at that the velocities match $v_\mathrm{DEP}/v_\mathrm{fluid} = 1$. Towards the center of the flow the fluid flow has a stronger impact on particle motion. Towards the wall the DEP velocity has a stronger impact on particle motion.

The ratio $v_\mathrm{DEP}/v_\mathrm{fluid}$ increases with increasing electric field strength and decreasing structure size. This means that the impact of DEP (which is leading to trapping) increases. Accordingly, with an increased ratio of $v_\mathrm{DEP}/v_\mathrm{fluid}$ more particles are trapped.

As described (Sec. 4.1) the trapping locations are at the edges of pore windows (only for particles that experience pDEP). This is because the DEP force attracts particles towards these edges. It further shows, that particles that enter the zones of $v_\mathrm{DEP}/v_\mathrm{fluid} > 1$ are trapped.

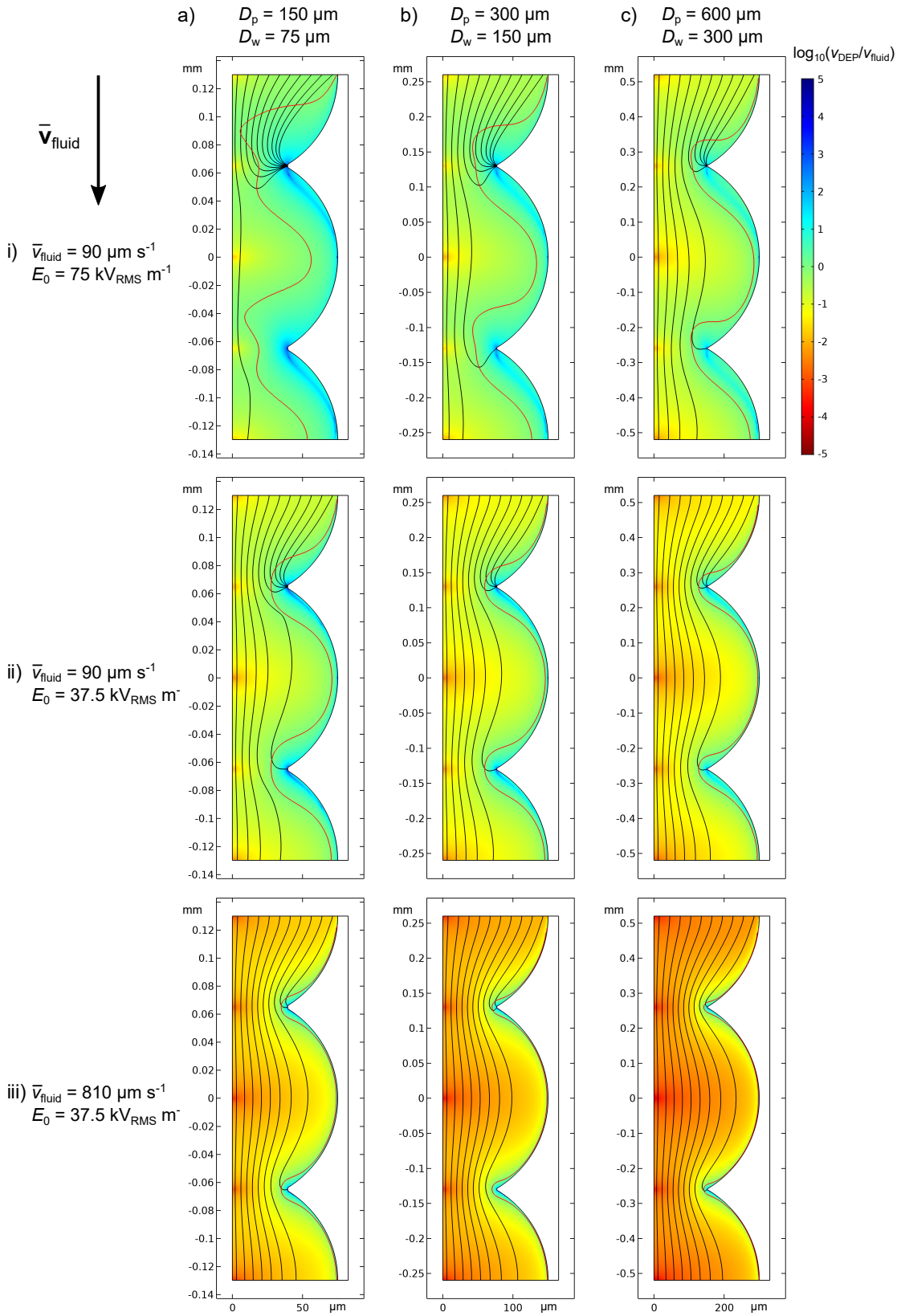

Figure 6.5: Particle trajectories (black lines) (PS particles, 4.5 µm diameter) in model filter cells of different dimension (D_p, D_w) at varied mean fluid flow velocities $\bar{v}_{fluid}$ and electric field strengths E_0. The fluid flow is directed downwards. The colour map shows the spatially resolved velocity ratio that particles experience due to DEP and fluid flow. The red lines shows where this velocity ratio is $v_{DEP}/v_{fluid} = 1$.

6.2.4 Simulated separation efficiency

Further, the simulated particle trajectories of Fig. 6.5 were used to investigate the impact of process parameters on the separation efficiency (percentage of trapped particles). Each particle trajectory divides the total amount of particles in two fractions: an inside fraction (towards the center of the flow) and an outside fraction (towards the wall). When travelling along the trajectory the fractions inside and outside of the particle trajectory remain constant because particle trajectories never cross each other under laminar flow conditions in a continuous electric field. Based on this model, the percentage of trapped particles must be at least the fraction of particles on the outside of the trapped particle trajectories. Further, the percentage of trapped particles can be at most the fraction on the inside of the untrapped trajectories. Tab. 6.1 shows the calculated separation efficiencies dependent on the number of trapped particle trajectories. The calculation to determine these minimum and maximum separation efficiencies is described in the Appendix A.

n	separation efficiency, η (-)
1	0.070 ± 0.040
2	0.166 ± 0.056
3	0.288 ± 0.066
4	0.424 ± 0.070
5	0.561 ± 0.068
6	0.691 ± 0.062
7	0.805 ± 0.052
8	0.896 ± 0.039
9	0.959 ± 0.024
10	0.992 ± 0.008

Table 6.1: Separation efficiency dependent on the number of trapped particle trajectories in simulations n. The calculation path is shown in Appendix A.

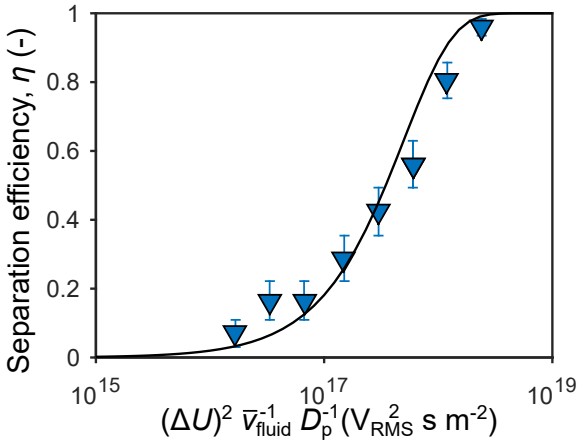

Figure 6.6: Separation efficiency after the first pore window as a function of $\bar{x} = (\Delta U)^2 \bar{v}_{\text{fluid}}^{-1} D_{\text{p}}^{-1}$ for the simulations shown in Fig. 6.5 using Tab. 6.1. The black line shows the fit $\eta(\bar{x}) = 1 - \exp(\bar{x}/C)$, with $C = -5 \times 10^{17}\,\text{V}_{\text{RMS}}^2\,\text{s}\,\text{m}^{-2}$.

Fig. 6.6 shows the separation efficiencies of the simulations shown in Fig. 6.5 after the first pore window (!) as a function of $\bar{x} = (\Delta U)^2 \bar{v}_{\text{fluid}}^{-1} D_{\text{p}}^{-1}$. The black line shows a fit according to (Pesch, 2018)

$$\eta(\bar{x}) = 1 - \exp\left(\frac{\bar{x}}{C}\right), \tag{6.3}$$

with the fitting parameter $C = -5 \times 10^{17}\,\text{V}_{\text{RMS}}^2\,\text{s}\,\text{m}^{-2}$. The good match of calculated separation efficiency and fit shows that separation efficiency can be described as a function of $\bar{x}$ and each of its containing parameters: the applied voltage difference squared $(\Delta U)^2$, the reciprocal of the average fluid velocity $\bar{v}_{\text{fluid}}^{-1}$, and the reciprocal of the pore diameter

D_p^{-1}. D_p stands representative for the pore structure dimension s, since the model pore geometry was scaled as a whole.

The approach to describe the separation efficiency of DEP filtration as a function of a parameter $\bar{x}$ was formerly used by Pesch (2018). While his porous structures were very different (two-dimensional arrays of insulating posts) from the ones used here, the same dependency on applied voltage and average fluid velocity was found: $\bar{x} \propto (\Delta U)^2 \bar{v}_{\text{fluid}}^{-1}$, with $\bar{v}_{\text{fluid}}$ being linearly dependent on the volumetric fluid flow (Q).

Chapter 7

Design and functionality of DEP filtration

The theoretical evaluation in the previous chapter and the studies of Pesch et al. (Pesch et al., 2017, 2018) (Pesch, 2018) give a profound theoretical understanding of the DEP filtration process. They predict the influence of important process and filter structure parameters on the particle separation efficiency in DEP filtration applications. Nevertheless, without experimental validation, these predictions remain hypothetical.

In this chapter the functionality of DEP filtration is investigated in practice. This is the first experimental study that aims for general understanding which can be applied to design future DEP filtration-based separators. The first section investigates the separation efficiency as a function of process parameters (flow rate, applied voltage, and filter pore diameter). In the second section, the influence of the filter structure geometry on the separation efficiency is investigated by comparing two filters with almost inverse structures. In the last two chapters the capacity of DEP filters and the possibility to recover retained particles is investigated.

All experiments of this chapter are done with suspensions of monodisperse polystyrene (PS) particles of 500 nm diameter. As a filter structure open porous alumina-mullite foams are used. Only in Sec. 7.2, alternative filters (packed bed of glass beads) are used to study the influence of the filter pore geometry. Experimental setup, procedure and all relevant measures are described in Sec. 5.1. The content of this section is based on M. Lorenz, D. Malangré, F. Du, M. Baune, J. Thöming, and G. R. Pesch (2020). High-throughput dielectrophoretic filtration of sub-micron and micro particles in macroscopic porous materials. *Analytical Bioanalytical Chemistry*, 412, 3903-3914. doi: 10.1007/s00216-020-02557-0

7.1 Separation efficiency as a function of process parameters

This section investigates how the DEP separation efficiency scales as a function on key parameters. All experiments of this parametric study were carried out with fluorescent 500 nm polystyrene beads. The fluid electric conductivity was $\sigma_m = 1.7 \times 10^{-4}\,\mathrm{S\,m^{-1}}$ and the frequency $f = 1\,\mathrm{kHz}$. Under these conditions all particles showed positive DEP (Eq. (2.33)). Mechanical trapping of the 500 nm PS particles was low ($\approx 2\%$) for all applied flow rates between 1 and 11 $\mathrm{mL\,min^{-1}}$. Consequently, the impact of mechanical trapping was low in comparison to DEP-driven trapping.

7.1.1 Influence of flow rate and applied potential

DEP separation efficiency decreases with increasing volumetric flow rate and decreasing applied voltage (Fig. 7.1) at otherwise constant conditions. A particle is trapped when it is pulled into a trapping zone (i.e., an electric field maximum) which is defined as a region where the DEP force dominates over the drag force exerted by the fluid onto the particle. The probability that a particle is trapped (expressed by the separation efficiency) is therefore assumed to be dependent on the ratio of these competing forces. The DEP force (Eq. (2.36)) that correlates with the applied voltage squared $(\Delta U)^2$ and the drag force that correlates with the fluid velocity v_{fluid} and thus the volumetric flow rate Q. Therefore, the ratio of DEP force to drag force is proportional to $F_{\mathrm{DEP}}/F_{\mathrm{drag}} \propto (\Delta U)^2 Q^{-1}$.

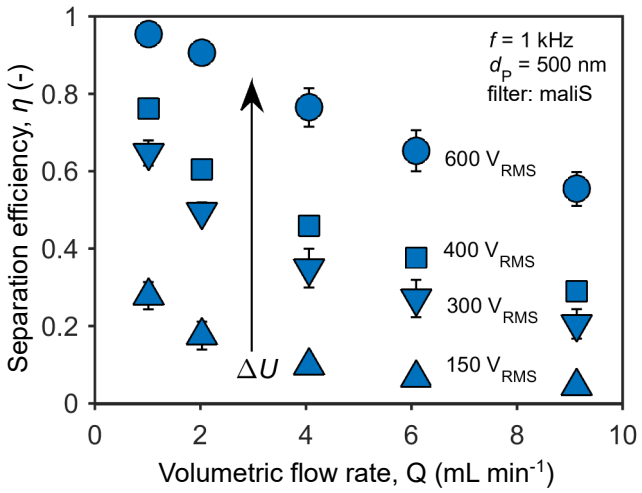

Figure 7.1: Separation efficiency as a function of the volumetric flow rate and the applied voltage. Each data point represents the average of three measurements. The corresponding standard deviations are given by the error bars. This figure was reprinted with permission from (Lorenz et al., 2020).

7.1.2 Influence of the the filter structure size

In order to study the influence of the structure size it is important to define what structure size means. In an inhomogeneous structure such as the foamed alumina-mullite filters this is complicated because the geometric characteristics of a ceramic filter structure scale differently. It can be distinguished in macroscopic and microscopic structure. The macroscopic structure can be described by pore diameter, pore window diameter, and hydraulic diameter. In the alumina-mullite filters, these diameters scale almost linearly with each other (see Tab. 5.1) indicating that the whole macroscopic structure scales by the same factor. One of these diameters is enough to correlate the separation efficiency to the macroscopic structure. The microscopic structure describes the surface roughness and the sharpness of edges, for example, at pore windows. The macroscopic structure is expected to have an impact on fluid flow, electric field gradient, and adhesion forces in a thin layer close to the filter surface. Estimating that this layers thickness is similar to the dimension of the surface roughness, it is expected that the microscopic structure has a much smaller impact on the separation efficiency than the macroscopic structure. That the exact shape of a field disturbing obstacle is rather irrelevant for the separation efficiency was found by Pesch et al. (2017). They showed that $\nabla|\mathbf{E}|^2$ around an obstacle is stronger influenced by its size and alignment than its surface shape. Therefore, this investigation will focus on the impact of the macroscopic filter size.

Here, the hydraulic pore diameter (d_h) is used as the characteristic structural size, because it provides comparability between filter structures. Experiments show that the separation efficiency increases with decreasing hydraulic pore diameter, when all other parameters are kept constant (Fig. 7.2). This meets expectations because the average DEP

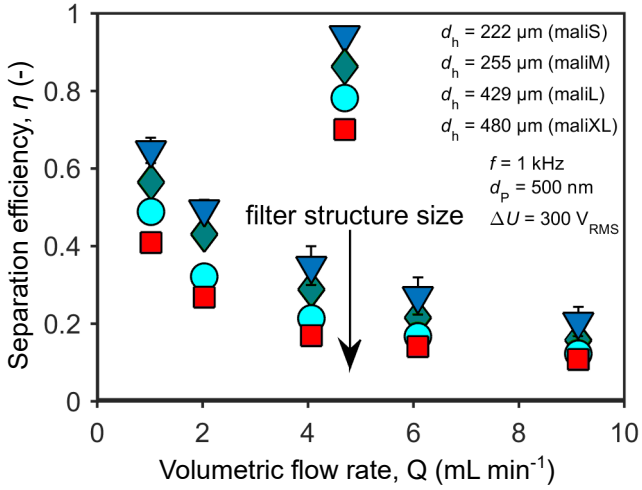

Figure 7.2: Separation efficiency as a function of the filter structure size. Each data point represents the average of three measurements. The corresponding standard deviations are given by the error bars. This figure was reprinted with permission from (Lorenz et al., 2020).

force acting on each particle is assumed to be inversely proportional to the hydraulic diameter: Under the assumption that the whole structure scales equally, the simulations of Sec. 6.2.1 (and (Lorenz et al., 2020), ESM, section C) show that the volume averaged $\nabla|\mathbf{E}_{\mathrm{RMS}}|^2$ in the filter void volume is inversely dependent on the structural size. Thus, for particles that are randomly distributed in the filter (which can be assumed for the tortuous flow paths in a randomized porous structure), the effective average DEP force $\bar{F}_{\mathrm{DEP}}$ is inversely proportional to the filter's structural size, $\bar{F}_{\mathrm{DEP}} \propto d_{\mathrm{h}}^{-1}$.

7.1.3 Scaling parameter in porous filters

The simulations of Sec. 6.2.4 predict that the separation efficiency is a function of $\bar{x} = (\Delta U)^2 \bar{v}_{\mathrm{fluid}}^{-1} d_{\mathrm{h}}^{-1}$ (Fig. 6.6). With the volumetric flow rate Q being directly proportional to the superficial fluid velocity $\bar{v}_{\mathrm{fluid}}$, $\bar{x}$ can be assumed as $\bar{x} = (\Delta U)^2 Q^{-1} d_{\mathrm{h}}^{-1}$. In order to test if the separation efficiency is indeed a function of $\bar{x}$, the separation efficiency of the finest filter (maliS) and the coarsest filter (maliXL) are plotted against $\bar{x} = (\Delta U)^2 Q^{-1} d_{\mathrm{h}}^{-1}$ (Fig. 7.3). They collapse onto one line. The function $\eta = 1 - \exp(\bar{x}/C)$, with the fitting coefficient $C = -4.43 \times 10^{15}\,\mathrm{V}_{\mathrm{RMS}}^2\mathrm{hm}^{-4}$, results in a good fit (black line), validating that the separation efficiency indeed scales with the applied voltage squared ($(\Delta U)^2$), the inverse of the volumetric flow rate (Q^{-1}), and the inverse of the hydraulic diameter of the filter (d_{h}^{-1}). These parameters can be used to control particle retention in a DEP filtration process.

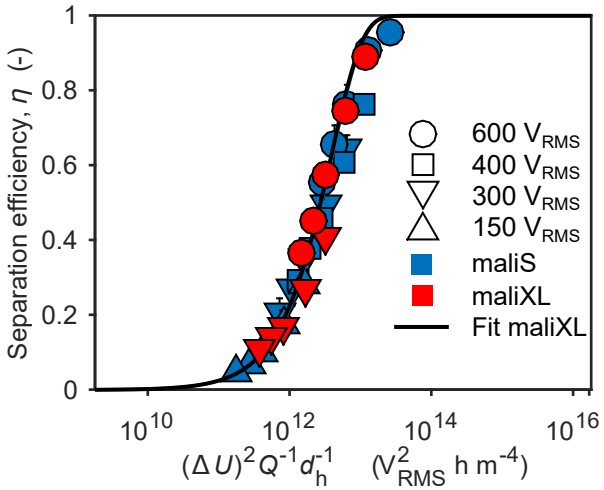

Figure 7.3: Separation efficiency (η) as a function of $\bar{x} = (\Delta U)^2 Q^{-1} d_{\mathrm{h}}^{-1}$ for the finest (maliS) and the coarsest ceramic filters (maliXL), varied voltage ($\Delta U = 150\,\mathrm{V}_{\mathrm{RMS}}$ to $600\,\mathrm{V}_{\mathrm{RMS}}$), and varied volumetric flow rate ($Q = 1\,\mathrm{mL\,min}^{-1}$ to $9\,\mathrm{mL\,min}^{-1}$). The results for the filter structure maliS (blue) are the ones shown in Fig. 7.1. Fitting was done using $\eta = 1 - \exp(\bar{x}/C)$ resulting in $C = -4.43 \times 10^{15}\,\mathrm{V}_{\mathrm{RMS}}^2\mathrm{hm}^{-4}$. The electric field frequency during experiments was $f = 1$ kHz.

$\bar{x}$ can also be used as an indication how well a the geometrical aspects of a filter are suited to achieve high separation efficiencies. In the following sections, $\bar{x}$ is used to

compare DEP filtration in foamed alumina-mullite filters to DEP filtration in packed beds of glass beads and microchannels.

7.2 Separation efficiency in foamed structures and packed beds

Here, the separation efficiencies in porous alumina-mullite filters and packed bed of glass beads are compared. Packed beds of glass beads were used for nearly all reported DEP filtration studies on DEP filtration (Fritsche and Haniak, 1975, Benguigui and Lin, 1982, Lin and Benguigui, 1982, Suehiro et al., 2003, Sisson et al., 1995, Wakeman and Butt, 2003). The comparison will show which filter geometry is better suited to achieve high separation efficiencies.

Comparison of the pore geometries of both filters shows that they provide almost inverse pore geometries. While the alumina-mullite foams have spherical pores (structure is shown in Fig. 5.1c), the pores in a packed bed are the remaining void volume around spherical glass beads. The pores in alumina-mullite foams are convex. The pores in a packed bed of glass beads are concave. For good comparability, the size of the glass beads was chosen to result in similar hydraulic pore diameters: Glass beads of two different diameters were used, $d_{\mathrm{sphere}} = 350\,\mu\mathrm{m}$ and $d_{\mathrm{sphere}} = 1\,\mathrm{mm}$. The hydraulic pore diameters for the packed bed of uniform spheres calculates as $d_{\mathrm{h}} = 2/3 \times d_{\mathrm{sphere}}\Phi/(1-\Phi)$, which results in $d_{\mathrm{h}} = 156\,\mu\mathrm{m}$ and $d_{\mathrm{h}} = 446\,\mu\mathrm{m}$ when assuming porosities of $\Phi = 0.4$ (standard value for packed uniform spheres).

When plotting the separation efficiencies in packed beds of glass beads as a function of $\bar{x} = (\Delta U)^2 Q^{-1} d_{\mathrm{h}}^{-1}$ they are clearly collapsing onto a different line than the separation efficiencies of the foamed alumina-mullite filters (Fig. 7.4). The fit of the separation efficiencies of the packed bed filters is shifted by about one order of magnitude to the right. Consequently, in the foamed alumina-mullite filter, $\bar{x}$ (which could be interpreted as the cost for operating the process) can be an order of magnitude lower than that in the packed bed of glass beads, to achieve the same separation efficiency. In other words, in the foamed filter, the same separation efficiencies are achieved at the same applied electric field strength and hydraulic pore diameter but at a 10-fold higher volumetric flow rate. A difference by factor two can be related to the different fluid velocity in the packed beds (at constant Q). Since the packed beds are half as porous as the foamed structures, the superficial fluid velocity in them is increased by factor two. However, even when accounting for the different fluid velocity the separation efficiency in the foamed filters is notably higher.

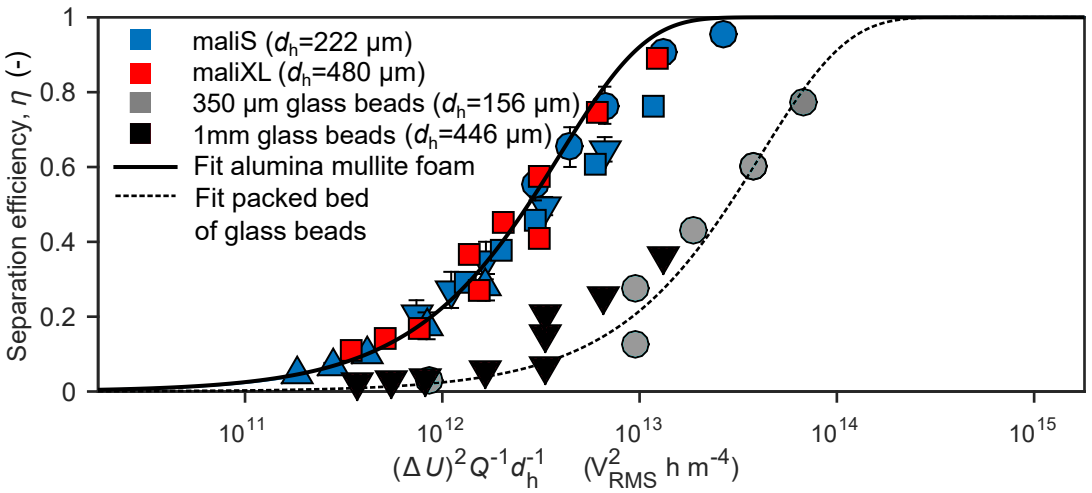

Figure 7.4: Comparison of the separation efficiency (η) as a function of $\bar{x} = (\Delta U)^2 Q^{-1} d_h^{-1}$ in foamed alumina-mullite filters (already shown in Fig. 7.3) and packed beds of 350 µm and 1 mm glass beads. Applied voltage and volumetric flow rate were varied: ΔU = 150-600 V_{RMS}, Q = 1-9 mLmin^{-1}. Fitting for the separation efficiency of the glass beads was done by using $\eta = 1 - \exp(\bar{x}/C)$, with the fitting constant $C = -8.2 \times 10^{14}$ $V^2_{RMS} h^{-1} m^{-4}$. The electric field frequency during experiments was f = 1 kHz.

It is reasonable that the separation efficiency in foamed filters is essentially increased by the pore windows (constrictions that lead from one pore to another pore). The particles inevitably have to pass the pore windows and thus the regions where DEP forces are highest (Fig. 7.5a). In a packed bed of spheres, the pore diameters are changing slower (Fig. 7.5b). Sharp constriction that are comparable to the pore windows of a foamed structure are missing. Further, the majority of the suspension follows the paths of lowest flow resistance which are the regions where the pore path is widest and the DEP force is lowest.

Figure 7.5: Schematic comparison of the geometry of foamed alumina-mullite filters (a) and backed beds of glass beads (b).

7.3 Filter capacity

At long filtration times, particles accumulate in the filter. The filter void volume becomes filled with particles. In depth filtration processes this can lead to filter clogging and the filter must be cleaned (e. g., by backflushing) to recondition its properties. In DEP filtration clogging is not expected to be a problem because the particles are much smaller than the pores and it takes more retained particles to fill the pathways through the filter. However, with increasing number of retained particles the particle trapping zones are filled. It is expected that this leads to a decreased particle separation efficiency because the free space in the zones which are suited for particle trapping is decreasing. In this section, the dependence of the separation efficiency on the number of retained particles is investigated with the aim to determine the capacity of the DEP filter to retain particles.

To investigate the filter capacity, the retention of 500 nm PS particles was investigated at a fluid electric conductivity of $1.5 \times 10^{-4}\,\mathrm{S\,m^{-1}}$. To trap a sufficient number of particles for capacity investigations, DEP filtration was applied for a much longer time and with increased particle concentration ($c_0 = 3.7 \times 10^7\ \mathrm{mL^{-1}}$) compared to previous experiments.

Particle concentration in the suspension at the filter outlet over a period of 45 min is shown in Fig. 7.6. The figure shows three different phases: Before $t = 0\,\mathrm{s}$ the suspension is passing the filter without applied electric field. Between $t = 0\,\mathrm{s}$ and $t = 2500\,\mathrm{s}$ the electric field is applied and particles are retained by DEP filtration. The last phase shows the recovery phase when the electric field is switched off. Here, only the duration of DEP filtration will be considered. The concentration of particles exiting the filter increases (and thus, the separation efficiency decreases) during DEP separation with an increasing number of particles already retained in the filter. About 2.55×10^9 particles (corresponding to 0.048‰ of the filter void volume) could be trapped until the separation efficiency decreased to 60.6% of the initial (i. e., maximum) separation efficiency. The function $c(t) = c_0 - (c_{\mathrm{start}} - c_0)(1 - \exp(-t/\tau))$, with $c_{\mathrm{start}} = c_0 + (c_{\mathrm{min}} - c_0)/(1 - \exp(-t_{\mathrm{min}}/\tau))$, τ the time period until separation efficiency decreases to 60.6% of its initial value, and t_{min}, the time when the particle concentration reaches its minimum, describes the particle concentration well.

The results agree with the prediction that the separation efficiency of the filter decreases with an increasing number of particles occupying trapping zones. Of course, these particles also affect the electric field in the filter, but the electric field change is expected to be small for two reasons. Firstly, the dielectric properties of accumulated particles in suspension are assumed to be similar to the properties of the suspension. Secondly, the regions that are occupied by accumulated particles are small in comparison to the total pore volume. Even at the increased particle concentration of the long-term experiment, the total volume

of retained particle was about a factor of 10^4 smaller than the porous volume of the filter. This further indicates, that clogging of the filter is unproblematic.

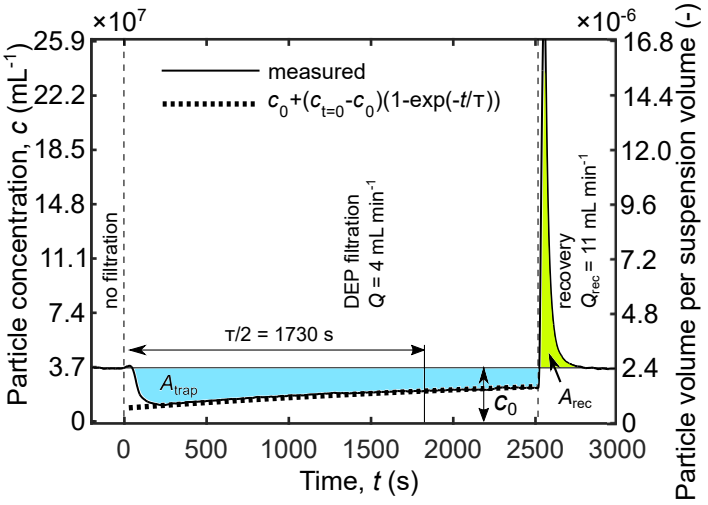

Figure 7.6: Long-term filtration experiments to determine filter capacity and particle recovery. Shown is the concentration of 500-nm PS particles in the suspension at the filter outlet during DEP filtration and subsequent particle recovery. The particle concentration in the suspension entering the filter is $c_0 = 3.7 \times 10^7\,\mathrm{mL}^{-1}$, corresponding to a particle to suspension volume fraction of 2.4×10^{-6} (see right axis). The areas A_{trap} (blue) and A_{rec} (green) multiplied by the related flow rates during that times are proportional to the numbers of particles that were trapped and recovered. The volumetric flow (Q) during DEP filtration was $4\,\mathrm{mL\,min}^{-1}$ and was increased to $11\,\mathrm{mL\,min}^{-1}$ during recovery. The half characteristic relaxation time $\tau/2$ calculates as 1730 s.

7.4 Particle recovery

In theory, the recovery of retained particles is one of the strengths of DEP filtration. When applied correctly, the particles are expected to be recoverable from the filter by simply switching off the electric field and flushing the filter. In this section, particle recovery is investigated in practice.

In the three long-term experiments, according to the one that is presented in Fig. 7.6, it was found that 65% to 75% of the formerly trapped particles could be recovered immediately after switching of the electric field by flushing with the same suspension at $11\,\mathrm{mL\,min}^{-1}$. When considering all experiments of this thesis that were carried out in the alumina-mullite foamed filters, the recovery rate was always between 40% and 100%. These large deviations in recovery rate show that the process is very sensitive to the filtration conditions. It depends on the interaction between filter and particles due to electrostatic and van der Waals forces that are influenced by the suspension (pH value and ionic strength), and the particle and filter surface (zeta potential, roughness, loading with already trapped particles, etc.). Investigation of these dependencies is beyond the scope of this thesis. To

investigate the impact of particle and filter surface charge, the long-term experiments were repeated at a fluid pH value of 8.5 (by adding KOH). A pH value of 8.5 is above the isoelectric points of PS and mullite, which are characterized by isoelectric points at pH < 3 and pH = 7 (see Tab. 5.1), respectively. This leads to negative zeta potentials of particle and filter surfaces and repulsive electrostatic forces between them. As a consequence, the recovery rates increased substantially to values between 86% and 92%. The importance of the pH value was also observed regarding the mechanical retention of particles. When no electric field was applied, it was found that the mechanical trapping of 4.5 µm PS particles was 8% at pH = 5.7 while it decreased to < 2% at pH = 8.5. The experiments show that the majority of the particles can be recovered in a very concentrated form simply by flushing the filter and adjusting the pH value. Potentially, particle recovery could further be improved when the DEP force is inverted for recovery so that particles experience nDEP and are repelled from pDEP trapping zones. According to $\tilde{f}_{\mathrm{CM}}(\omega)$ Eq. (2.29), for particles of lower relative permittivity (ε_{p}) than the suspension (ε_{m}) (which is the case for most particles in aqueous suspension due to water's high relative permittivity of 80), nDEP can be applied by increasing the electric field frequency above the Maxwell-Wagner relaxation frequency ω_{MW} (Eq. (2.30)).

Chapter 8

Selective particle separation by DEP filtration

This chapter aims to make the transition from pure particle retention to selective-separation of particles. It is a topic on that no studies have been reported yet. In principle, there are two approaches how DEP filtration can be utilized to separate particles.

Separation by DEP of different magnitude but same direction

In this case particles are attracted to the same positions in the filter. Selective particle trapping can only be achieved when the conditions are finely tuned. The DEP force has to be sufficient to trap one type of the particles and too low to trap the other type. Since the conditions in a heterogeneous filter structure are heterogeneous, it is expected that sharp separation of particles with similar properties is very challenging. Although this separation process could be very useful, it requires more fundamental studies to provide understanding, which could subsequently be used for experimental investigations. This is beyond the scope of this thesis and remains an open task for future investigations.

Separation by pDEP and nDEP

The concept of pDEP- and nDEP-driven particle trapping in DEP filtration and how they are expected to result in different separation efficiencies was described in Sec. 4.1 and schematically shown in Fig. 4.2. In short, the concept can be summarized as: Particles that experience pDEP are attracted towards the edges that frame the pore windows. They are tightly trapped, at the filter surface where the DEP force is strongest and the fluid drag force rather low (no fluid velocity at the filter surface). Particles that experience nDEP are pushed away from the pore windows. The primary reason for these particles to be retained is that they are unable to pass the pores windows. It is expected that nDEP particle trapping is less effective than pDEP

particle trapping. The primary reason for this is that the nDEP force has to compete against significant drag forces to trap a particle, whereas pDEP trapped particles experience only low drag forces. More reasons are described in Sec. 4.1.

In this chapter, the second approach is used to investigate how particles of different electric conductivity can be separated from each other. Experimental setup, procedure and all relevant measures are described in Sec. 5.1.

8.1 Separation efficiency as a function of the fluid electric conductivity

Before investigating selective separation of particles from mixed particle suspension, it has to be tested if different separation efficiencies by pDEP and nDEP are possible in practice. Therefore, this section investigates the separation of particle suspensions that contain only one type of particles at a time. The process parameters are changed in a way that these particles are initially better polarizable than the surrounding medium and later less polarizable than the surrounding medium.

Most DEP-based devices use the electric field frequency to control the particles polarizability (which is characterized by the Clausius-Mossotti (CM) factor, $\tilde{f}_{\mathrm{CM}}$, (Eq. (2.29))) and thus if a particle shows pDEP or nDEP. Commonly particles have relaxation frequencies (frequency at that interfacial polarization cannot follow the oscillation of the field anymore) between 10^5 Hz and 10^7 Hz. While such frequencies are easily applicable in microchannels when the required voltages and currents are rather low, more powerful and essentially more expensive amplifiers are required for DEP filtration. Here a different way is used to adjust the particle polarizability described by $\mathrm{Re}\left[\tilde{f}_{\mathrm{CM}}\right]$. At frequencies below the Maxwell-Wagner relaxation frequency $\mathrm{Re}\left[\tilde{f}_{\mathrm{CM}}\right]$ is a function of the particle conductivity (σ_{p}) and the fluid conductivity (σ_{m}) (Eq. (2.31)): $\mathrm{Re}\left[\tilde{f}_{\mathrm{CM}}\right] = (\sigma_{\mathrm{p}} - \sigma_{\mathrm{m}})/(\sigma_{\mathrm{p}} + 2\sigma_{\mathrm{m}})$. Thus $\mathrm{Re}\left[\tilde{f}_{\mathrm{CM}}\right]$ can be adjusted by changing σ_{m} (see Fig. 2.5). When, $\sigma_{\mathrm{p}} > \sigma_{\mathrm{m}}$, the particle is better polarizable and shows pDEP ($\mathrm{Re}\left[\tilde{f}_{\mathrm{CM}}\right] > 0$). By raising σ_{m} above σ_{p} the particle becomes less polarizable and shows nDEP ($\mathrm{Re}\left[\tilde{f}_{\mathrm{CM}}\right] < 0$).

The fluid electric conductivity was increased by adding KCl to the suspension. The lowest fluid electric conductivity used was $\sigma_{\mathrm{m}} = 1.2 \times 10^{-4}\,\mathrm{S\,m^{-1}}$ (lowest electric conductivity that was reproducible with the available equipment). The maximum fluid electric conductivity used was $50 \times 10^{-4}\,\mathrm{S\,m^{-1}}$. Higher fluid conductivities were neglected because the DEP filtration process changed significantly at higher fluid conductivities. This was ascribed to the increased Joule heating, which can cause boiling and bubble formation in the filter.

Polystyrene particles

The separation efficiency of polystyrene (PS) particles with 1.0 µm, 2.0 µm, and 4.5 µm diameter as a function of the fluids electric conductivity is shown in Fig. 8.1a. For all particle diameters the highest separation efficiency occurs at the lowest fluid electric conductivities ($\sigma_m = 1.2 \times 10^{-4}\,\mathrm{S\,m^{-1}}$). The separation efficiencies of the 2 µm and 4.5 µm particles are at this point already showing a downslope. The 1 µm particles show a downslope beginning at about $3 \times 10^{-4}\,\mathrm{S\,m^{-1}}$. All curves have a minimum trapping efficiency. This minimum shifts to higher conductivities with decreasing particle diameters. While the minimum is quite distinct for the 4.5 µm particles, it is harder to identify for the smaller particles. After the minima, the separation efficiencies increase slightly until they remain mostly constant.

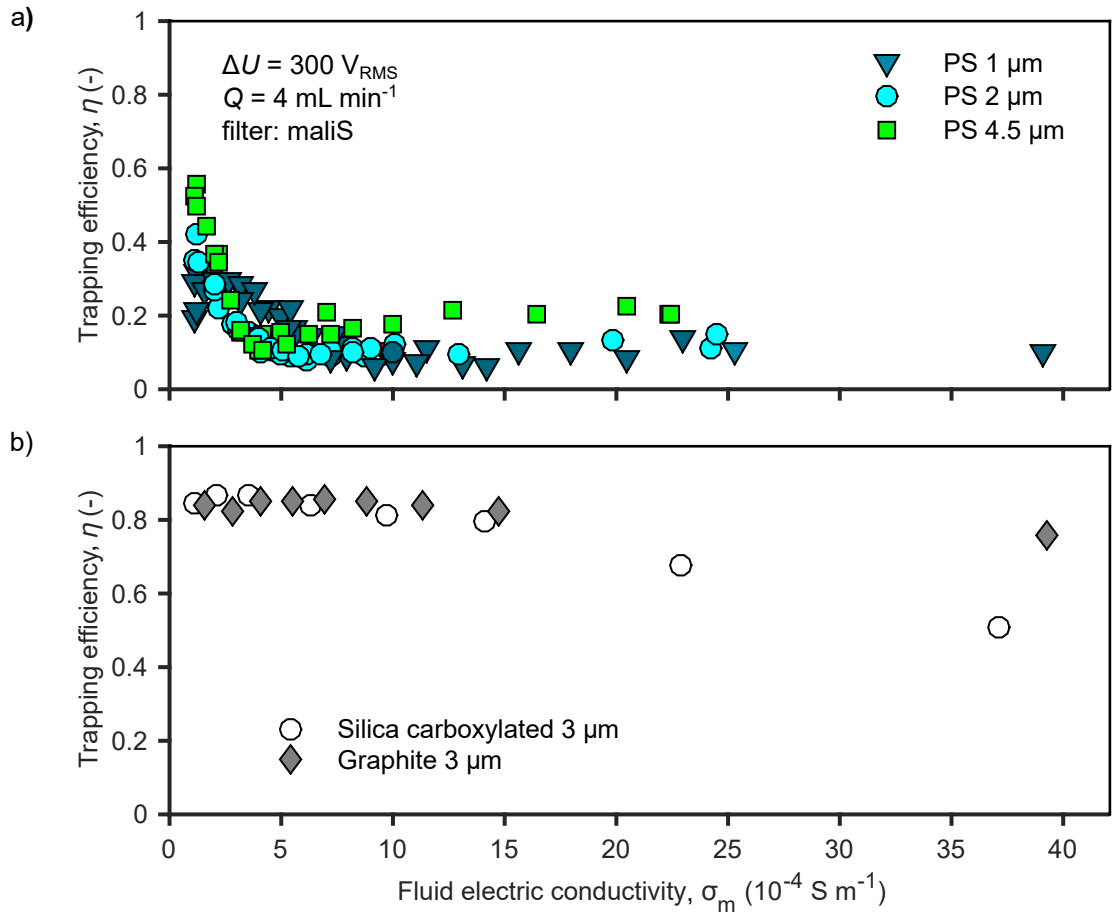

Figure 8.1: Particle separation efficiency as a function of the fluid electric conductivity PS particles of different size (a) and silica and graphite particles of 3 µm diameter (b).

The results agree very well with the above described concept of pDEP and nDEP particle separation. At low fluid electric conductivity particles are more conductive than the surrounding fluid and are thus trapped by pDEP. At high fluid electric conductivities

particles are less conductive than the surrounding fluid and are trapped by the weaker nDEP trapping mechanism. When σ_p and σ_m are equal or similar the particle is not or only weakly polarized and separation efficiency reaches a minimum. According to this theory, the effective particle electric conductivities of the particles shown in Fig. 8.1a should be $\sigma_{PS,1\mu m} \approx 10 \times 10^{-4}\ Sm^{-1}$, $\sigma_{PS,2\mu m} \approx 6 \times 10^{-4}\ Sm^{-1}$, and $\sigma_{PS,4.5\mu m} \approx 4.2 \times 10^{-4}\ Sm^{-1}$. Comparison of these values to the expected minimum and maximum values of the particle electric conductivity (Tab. 5.3) shows, that they fall in a very reasonable range.

The agreement between theory and experimental results becomes even more evident when particle separation efficiency and particle polarizability are plotted together, as functions of σ_m. They are supposed to show a very similar trend, because the particle polarizability is directly proportional to the DEP force. Fig. 8.2 shows such a plot for the 4.5 µm-PS particles. The calculation of the polarizability was done according to Eq. (2.31), with $\sigma_{PS,4.5\mu m} = 4.2 \times 10^{-4}\ Sm^{-1}$. $\mathrm{Re}\left[\tilde{f}_{CM}\right]$ is rescaled by taking the absolute of $\mathrm{Re}\left[\tilde{f}_{CM}\right]$ and by rescaling all negative values by a factor of 0.6. Employing such a (purely observational) rescaling factor for the negative part of $\mathrm{Re}\left[\tilde{f}_{CM}\right]$ is justified as the prediction is that nDEP trapping is always less efficient (by an unknown factor) compared to pDEP trapping. Separation efficiency and modified particle polarizability match remarkably well.

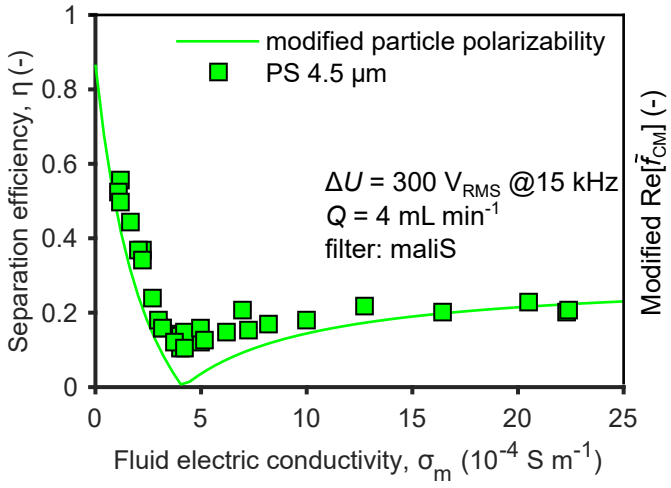

Figure 8.2: Comparison of the separation efficiency and the particle polarizability of a 4.5 µm PS particle as a function of the fluid electric conductivity. The data points are the same as the experimental data shown in Fig. 8.1. The line represents the particle polarizability ($\mathrm{Re}\left[\tilde{f}_{CM}\right]$) for a particle with a conductivity of $4.2 \times 10^{-4}\ Sm^{-1}$. It shows the absolute value of $\mathrm{Re}\left[\tilde{f}_{CM}\right]$ after Eq. (2.29) with the modification that negative values for $\mathrm{Re}\left[\tilde{f}_{CM}\right]$ were multiplied by a fitting factor of 0.6.

Two more comments on the investigations: Firstly, the fact that the minimum separation efficiency is not zero can be explained by multiple reasons. A certain fraction of particles is separated due to depth filtration effects. However, compared to pure depth fil-

tration the trapping is still high. This could be due to an increased amount of flow vortices that are caused by electric field effects. Particle can be trapped by such vortices (Green and Yossifon, 2013). Another explanation could be that the particles have slightly different electric conductivities so that a fraction of particles is always affected by DEP. Secondly, the results of Fig. 8.1a show further that $\sigma_m = 1.2 \times 10^{-4}\,\mathrm{S\,m^{-1}}$ was barely low enough to achieve pDEP trapping. It can be expected that the separation efficiency is even higher at decreased σ_m when particle polarization ($\mathrm{Re}\left[\tilde{f}_{CM}\right]$) reaches its maximum value.

Silica particles

The separation efficiency of carboxylated silica particles (3 µm diameter) is slightly decreasing with increasing fluid electric conductivity (Fig. 8.1b). The high separation efficiency (which only slowly decreases with increasing σ_m) indicates that silica particles experience pDEP for all σ_m that were applied. As shown in Tab. 5.3 the effective conductivity of (non-functionalized) amorphous silica particles with 3 µm diameter is expected to be in the range between $20 \times 10^{-4}\,\mathrm{S\,m^{-1}}$ and $40 \times 10^{-4}\,\mathrm{S\,m^{-1}}$. The experimental data indicate that the conductivity is even higher than $40 \times 10^{-4}\,\mathrm{S\,m^{-1}}$. An explanation could be an increased surface charge due to carboxylation.

Graphite particles

The separation efficiency of graphite particles is almost independent of the change in fluid electric conductivity (Fig. 8.1b). The separation efficiency remains at about 80% over the whole range between $1 \times 10^{-4}\,\mathrm{S\,m^{-1}}$ and $40 \times 10^{-4}\,\mathrm{S\,m^{-1}}$. The constantly high trapping efficiency was expected because the electric conductivity of graphite particles is well above any fluids electric conductivity so that the particles experience always pDEP.

The above described results show that separation of monodisperse particles from a fluid is essentially influenced by the particle and fluid electric conductivity. pDEP trapping is clearly more efficient to retain particles in the filter as nDEP while the least amount of trapping was found when the effective particle conductivity matched the fluid conductivity.

8.2 Electric conductivity selective particle separation

In this section, the different efficiencies of pDEP and nDEP particle trapping are used to separate particle mixtures from each other according to the particles' electric conductivity.

8.2.1 Separation of mixed suspensions – Separation of PS from graphite particles

The separation of graphite and PS is very suitable to understand the applicability of σ_p-selective particle separation. Graphite particles have the advantage of following the fluid flow rather well, due to their low density compared to most other highly conductive particles (metallic particles). The mixed suspension of PS (4.5 µm) and graphite (median diameter 3 µm) particles was prepared in the same way as the monodisperse suspensions but it contained both particle types, each at the same concentration as they were used in the monodisperse suspensions. The separation efficiencies of PS and graphite particles from a mixed-particle suspension are shown in Fig. 8.3 as a function of σ_m. Further shown are the separation efficiencies of the same particles from monodisperse particle suspensions, according to Fig. 8.1.

Initially, the separation efficiency of particle mixtures (filled circles) will be discussed. A comparison to the separation of the monodisperse suspensions will be done at the end of this subsection. At low σ_m, the separation efficiency is for both particle types at about 90% so that no selective separation is achieved. With increasing fluid electric conductivity, the separation efficiency of the PS particles drops beneath 20% at about $9 \times 10^{-4}\,\mathrm{S\,m^{-1}}$, until it rises again to about 30% above $15 \times 10^{-4}\,\mathrm{S\,m^{-1}}$. The graphite particles are trapped over the whole range with about 80% efficiency. It is noticeable that the trapping efficiency follows the trend of the PS particles but the changes are significantly smaller.

These results show that electric conductivity selective particle separation can be achieved with DEP filtration. As a measure to describe the selectivity of the separation process a new measure is introduced: The purification factor G. It describes the factor by which the number ratio of particles has changed during filtration. It can be defined for particles that penetrate the filter (filtrate), G_f, and particles that are retained in the filter, G_r. The purification factor for the particles that exit the filter is defined as

$$G_f = \frac{1-\eta_{PS}}{1-\eta_{graphite}}. \tag{8.1}$$

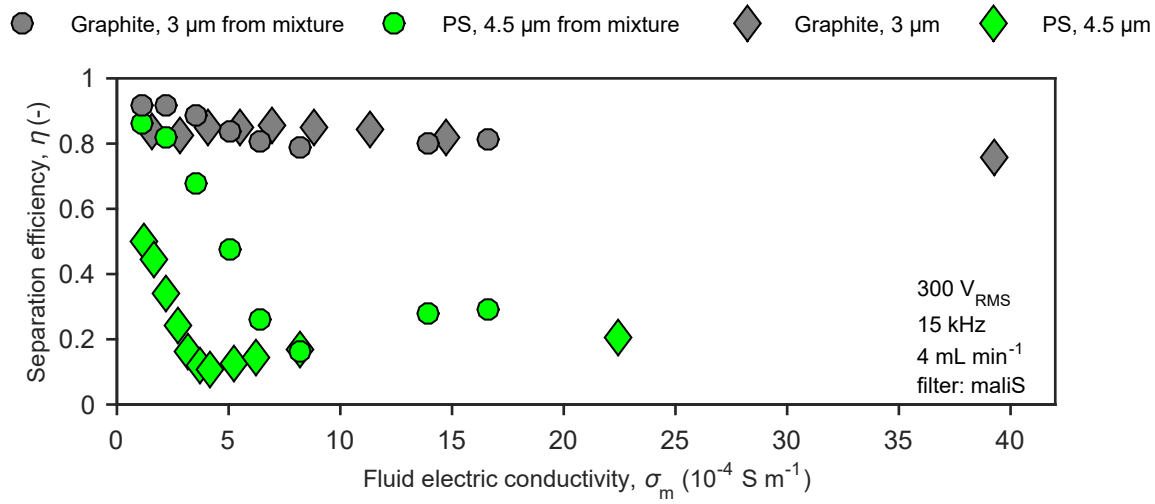

Figure 8.3: Separation efficiency of graphite (3 µm) and PS particles (4.5 µm) from a particle mixture as a function of the fluid electric conductivity. Additionally, shown are the separation efficiencies of the monodisperse cases for the same particles that were already shown in Fig. 8.3.

The highest purification factor in the filtrate G_f is achieved at about $\sigma_m = 8 \times 10^{-4}\,\mathrm{S\,m^{-1}}$,

$$G_f = \frac{1-\eta_{PS}}{1-\eta_{graphite}} = \frac{0.835}{0.213} = 3.9\,.$$

This means that the ratio of PS to graphite particles in suspension is, after filtration by factor 3.9, higher than before. The purification factor for the particles retained in the filter is defined as

$$G_r = \frac{\eta_{graphite}}{\eta_{PS}}\,. \tag{8.2}$$

G_r reaches its maximum of 4.8 also at a fluid conductivity of $8 \times 10^{-4}\,\mathrm{S\,m^{-1}}$. At lower fluid electric conductivities, where all particles are expected to show pDEP, particles are not separated from each other (purification ratios fall to 1). At higher fluid electric conductivities (when PS particles show nDEP and graphite particles pDEP) G_f falls to about 2.4 and G_r falls to 2.8. The separation efficiencies appear to stay constant when σ_m is further increased (for both the monodisperse and the mixed particle experiments). It is therefore expected that these purification factors can be achieved for further increased σ_m until additional mechanisms, such as electrothermal flow, become relevant. From an engineering point, this is an important result. It shows that selectivity can be achieved over a broad range of σ_m and not only at $\sigma_m = \sigma_p$ where particles show no polarization. It shows that DEP filtration can be used to separate particle mixtures even when the effective electric conductivity of the particles is quite diverse (due to different sizes, material, morphology etc.) in a step by step process. In each separation step σ_m can be adjusted to separate a more from a less conductive particle fraction.

Another important measure to characterize the separation process is the yield. The

yield describes for each involved particles species i the particle number ratio before and after filtration. It can be defined for particles retained in the filter and in the filtrate. The yield of retained particles defines as $Y_{r,i} = \eta$. The yield of particles in the filtrate is defined as $Y_{f,i} = 1 - \eta$.

To illustrate the potential separation performance of the DEP filtration process Tab. 8.1 and Tab. 8.2 show PS and graphite particle yields and the corresponding purification factors after 1 to 10 separation cycles (at $\sigma_m = 8 \times 10^{-4}\,\mathrm{S\,m^{-1}}$). It shows that extremely high purification ratios can be achieved after few filtration cycles. Of course, purification comes always on cost of the particle yield. However, obtaining 16.5% of the initial number of target particles but in a millionfold purified form after ten separation cycles could be very useful for many separation tasks.

Table 8.1: Yield of PS ($Y_{f,PS}$) and graphite particles ($Y_{f,graphite}$) and the resulting purification factor in the filtrate (G_f) after 1 to 10 separation cycles (n). The yield describes the particle concentration ratio in the filtrate before and after n cycles of filtration.

n	$Y_{f,PS} = (1-\eta_{PS})^n$	$Y_{f,graphite} = (1-\eta_{graphite})^n$	G_f
1	0.835	0.213	3.9
2	0.7	0.045	15.4
3	0.58	0.01	60
5	0.41	4.3×10^{-3}	926
10	0.165	0.9×10^{-7}	8.57×10^{5}

Table 8.2: Yield of PS ($Y_{r,PS}$) and graphite particles ($Y_{r,graphite}$) and the resulting purification factor of particles retained in the filter (G_r) after 1 to 10 separation cycles (n). The yield describes the particle concentration ratio in the filter before and after n cycles of filtration.

n	$Y_{r,PS} = \eta_{r,PS}^n$	$Y_{graphite} = \eta_{graphite}^n$	G_r
1	0.165	0.787	4.8
2	0.027	0.62	22.8
3	0.0045	0.49	109
5	1.2×10^{-3}	0.3	2469
10	1.5×10^{-8}	0.09	6×10^{6}

Comparison of the separation efficiencies achieved for mixed and monodisperse suspensions.
Three essential observations were made when comparing the separation efficiencies for mixed and monodisperse suspensions (Fig. 8.3).

i) The separation efficiency curves of PS particles are clearly different. The curve measured for mixed suspensions is clearly shifted to higher σ_m.

ii) The separation curves of the graphite particles show also differences, but these are not as pronounced. Graphite particles from a mixed suspension show a slightly increased trapping efficiency at low σ_m until trapping decreases.

iii) When comparing the separation curves of PS and graphite particles from a mixed suspension, it strikes that the graphite curve shows the same trends as the PS curve but at a much higher level.

It is assumed that the difference between separation from a monodisperse and mixed particle suspension is a result of graphite particles attaching to the surfaces of PS particles. The graphite particles used have a particle size distribution. The fraction of small graphite particles in the suspension can attach to the PS particles and increase their effective conductivity. This theory would explain the shift of the separation efficiency curve to higher fluid conductivities. Further, it could also explain the similar trend of the separation curves that were measured for the mixed suspension: A decreased PS particle separation efficiency leads to a decreased separation efficiency of surface-bound graphite particles. This is an important mechanisms that needs to be understood from further experiments. In microchannels, it was shown that particle agglomeration can be significantly reduced by pH adjustment, reducing electrostatic attraction between particles (Weirauch et al., 2019). Further investigations about the interaction of particles in DEP filtration are critical when aiming to separate particle mixtures with broad particle size distributions e. g. recovery of valuable metals from electronic waste.

8.3 Towards more complex separation tasks

Working towards the separation of precious metals from electronic waste dust, another and more complex separation task that was tested was the separation of PS from copper (Cu) particles. Cu particles with a flake geometry and a broad size distribution were used so that they provided good model particles for precious metal flakes in electronic waste dust. The handling of the Cu particles is more challenging than the filtration of graphite. While the dielectrophoresis-driven separation was not an issue, the main challenge was finding a way

to minimize particle retention by depth filtration effects. Cu particles have a much higher density (ρ_{Cu} = 9000 kg m^{-3}) than water and do not follow the fluid flow well. They tend to sediment much stronger so that they are already separated by depth filtration effects. Especially at low flow velocities they were hardly following the flow. In the experiments in foamed alumina-mullite filters, 60% to 90% of the copper particles were trapped by depth filtration without an applied electric field. Such strong separation is impracticable for DEP filtration since it requires substantially different trapping efficiencies without and with an electric field applied. In this section, it will be evaluated how filter geometry and material influence particle separation and how they can be designed to allow separation of heterogeneous particle mixtures by DEP filtration.

8.3.1 Geometrical aspects

The strong mechanical trapping reveals a weakness of foamed filter geometries for DEP filtration: Dense particles that do not follow the flow but sediment are likely to be trapped in a foamed filter. Due to the concave solid surfaces in the foamed filter, these particles will sediment to the bottom of the pore and remain there (Fig. 8.4a). For this reason, the foamed alumina-mullite filter was replaced by a packed bed of spheres. In a packed bed of spheres, all solid surfaces are convex. There are almost no areas in which particles can be trapped due to sedimentation. When the flow is directed with the gravity field, both gravity and the flow will transport particles through the filter (Fig. 8.4b). Under these conditions, particle trapping should be negligible if the short-distance electrostatic forces between particle and surface are repellent.

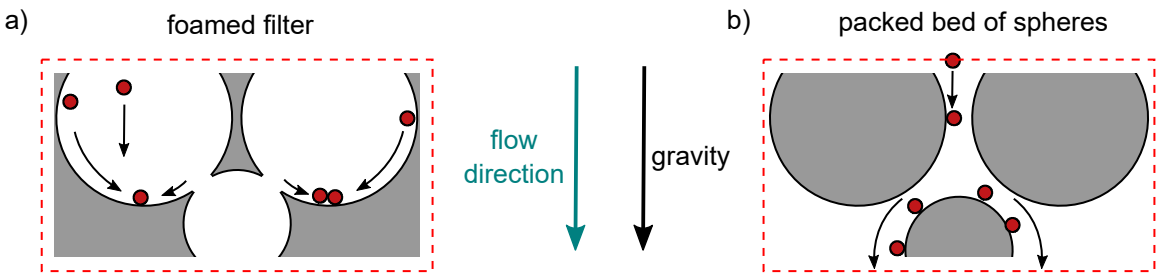

Figure 8.4: Schematic of the behaviour of sedimenting particles in a section of a foamed filter (a) and (its inverse structure) a packed bed of spheres (b). While sedimentation can lead to severe particle retention in the foamed filter (at local gravitational potential energy minima), particles will slide down the convex surfaces of a packed bed of spheres when the electrostatic forces between particle and surface are repellent (their are no gravitational potential energy minima).

8.3.2 Material aspects – particle adhesion

The filter material is another aspect that has a considerable impact on mechanical particle retention in the filter. Although the mechanical trapping efficiency of Cu particles reduced to almost zero in the packed bed of glass spheres at highest flow rate (11 mL min^{-1}), mechanical trapping was still significant at lower flow rates. Further, the recoverable fraction of particles from the filter after DEP filtration was almost zero. Both observations indicate that particles adhere to the filter surface and stop moving (at reduced flow velocity and during DEP filtration "close contact" is expected). Particle adhesion to the filter surface is essentially influenced by electrostatic forces and thus the surface charge of particles and filter.

The isoelectric point (iep) of Cu particles is at a pH value of 9.8. Accordingly, they have a positive zeta potential during experiments (pH≈ 6). Therefore, the Cu particles tend to adhere strongly to the very negatively charged glass surface (iep at pH< 3). It is impossible to change the pH value of the suspension to values above or below the ieps of copper and glass considering that the electric conductivity of the suspension needs to stay low to avoid strong Joule heating. A solution could be to replace the glass spheres by a material that possesses a higher iep close to copper: For example, α-alumina (iep at pH≈ 7 (Hirata et al., 1991)). Another option could be to adjust the pH value of the fluid that is used during particle recovery as it was already discussed in Sec. 7.4.

8.3.3 Separation of PS from copper particles in a packed bed of glass spheres

The considerations on geometry and material are applied in this section to separate a mixture of Cu flakes and 4.5 µm PS particles. A packed bed of glass spheres of 1 mm diameter was used as filter. Fig. 8.5 shows the separation efficiencies for Cu flakes and PS particles as a function of the fluid electric conductivity at volumetric flow of 11 mL min^{-1} and an ac voltage of $\Delta U = 300\,\mathrm{V_{RMS}}$ at 15 kHz.

The separation efficiencies shows similar characteristics as the ones of PS and graphite particles (Fig. 8.5). The separation efficiency for the copper particles is at about 90% over the whole range of fluid conductivities from 1.2 to $15 \times 10^{-4}\,\mathrm{S\,m^{-1}}$. The separation efficiency of the PS particles falls with increasing fluid electric conductivity. However, compared to the results of Fig. 8.5 the separation efficiency does not grow above $5 \times 10^{-4}\,\mathrm{S\,m^{-1}}$. It remains at the same level or decreases. This can be explained by the increased fluid velocity in the filter. Further, the author expects that $\nabla|\mathbf{E}|^2$ is lower in packed beds than in the foamed alumina-mullite structures. Thus DEP force and DEP-driven particle retention could be lower. However, this assumption needs to be tested by $\nabla|\mathbf{E}|^2$ simulations.

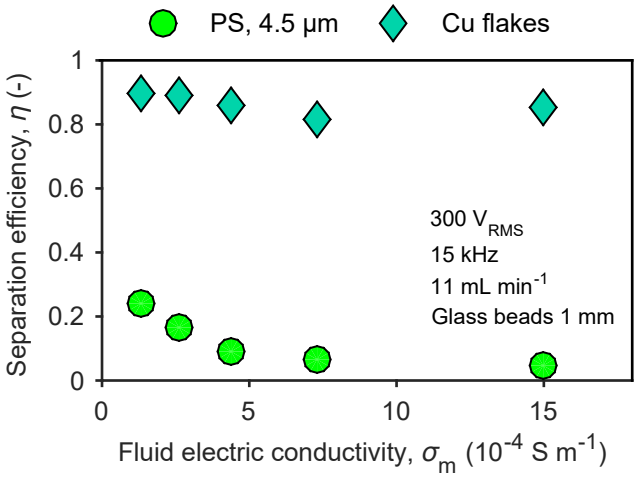

Figure 8.5: Separation of copper flakes and PS particles as a function of the fluid electric conductivity in a packed bed of glass spheres (1 mm diameter). Separation was done at a flow rate of 11 mL min^{-1} and a voltage of 300 V_{RMS} at 15 kHz.

The separation experiments of Cu flakes and PS particles reach even higher purification factors than the once achieved for graphite-PS separation. The purification factor lies at about 18 at $\sigma_m = 15 \times 10^{-4}$ S m^{-1}. The increased purification factor can be connected to the increased volumetric flow rate and the size of the copper flakes. The increased fluid flow rate is expected to diminish nDEP trapping more than pDEP trapping. Since the copper flakes (flake diameter $\approx$ 50 µm) are much bigger than the graphite particles ($d_p = 3$µm), they are even at high flow rates more efficiently trapped ($\mathbf{F}_{DEP} \propto$ particle volume) than the graphite particles at lower flow rates. However, the retained Cu flakes were not recoverable by simply flushing the filter after DEP filtration. This is ascribed to the strong adhesion of Cu flakes to glass beads that was described in Sec. 8.3.2. The glass spheres had to be removed from the setup to recover the copper from their surfaces. Future experiments could show how much recovery can be increased by changing the filter material and the pH value of the fluid.

Chapter 9

Conclusion and outlook

Separation of micron and sub-micron particles from liquids and from each other according to their properties is a challenging but essential task for applications in many industrial fields. Despite the variety of existing particle separation techniques, many separation tasks remain unsolved and new separation techniques are required to solve them.

Dielectrophoresis (DEP) describes the motion of polarizable particles in inhomogeneous electric fields. It can be used for highly selective particle separation according to their size, material, and morphology, without changing the particle properties. Most DEP-based particle separation techniques use microfluidic channels that are unsuited to process industrial-scale throughputs. The reason for this is that the DEP force scales with the gradient of the squared electric field, $\nabla|\mathbf{E}|^2$. The unit of this gradient is $\mathrm{V^2\,m^{-3}}$, showing that high electric voltages and small structures are required for high gradients. $\nabla|\mathbf{E}|^2$ is high at interfaces of materials with different dielectric properties, but quickly decreases with increasing distance from these interfaces. An alternative approach that can potentially solve the throughput limitation is a technique called DEP filtration. This technique uses open-porous filters that provide numerous tortuous flow paths, which are suited for high throughputs. The electric field is distorted at the filter surface so that high electric field gradients are generated providing good conditions for DEP particle retention. The few existing studies on DEP filtration solve very specific separation tasks, but are not suited to provide a general understanding of the physical phenomena of DEP filtration. However, such understanding is required to improve the technique and develop new applications.

This work investigates DEP filtration in a comprehensive experimental study to gain fundamental understanding. In a first step, a DEP filtration setup to conduct experiments was conceptualized and built. In the developed filter cell, almost 100% particle separation efficiency was achieved using 500 nm polystyrene particles and throughputs of $9\,\mathrm{mL\,min^{-1}}$ (filter cross section: $2\,\mathrm{cm^2}$). In a parametric study, the dependency of the separation efficiency on the applied voltage (ΔU), volumetric throughput (Q), and hydraulic pore

diameter (d_h) was investigated. The separation efficiency can be described as a function of a single variable $\bar{x} = (\Delta U)^2 Q^{-1} d_h^{-1}$. This dependence was validated for different filter structures in experiments and simulations, and can be regarded as a design guideline for DEP filtration applications. Another topic was to investigate the influence of the filter pore geometry. It was shown that separation efficiency in foamed filter structures was significantly higher than in packed beds of glass beads. The reason is that in a foamed structures, particles have to penetrate many sharp channel constrictions, at which $\nabla|\mathbf{E}|^2$ and consequently the DEP force is high. In packed beds of glass beads, these sharp constrictions are missing and hence DEP forces are much smaller.

Furthermore, the possibilities of selective particle separation by DEP filtration were investigated. It was shown that the separation efficiency of DEP filtration processes can be controlled by adjusting the fluids polarizability with respect to the particle polarizability. This effect was studied for the first time experimentally and successfully applied for separation of particles with different polarizability. It showed that particles could be separated from each other by adjusting the electric conductivity (and thus its polarizability) of the fluid to a value between the electric conductivities (polarizabilities) of the particles.

Recovery of trapped particles from the filter is important. It was shown that particle recovery is possible by switching-off the electric field and flushing the filter. In this context, the influence of the pH value of the fluid was investigated. It showed that particle recovery could significantly be increased when particle and filter carried net surface charges of same sign, which can be ascribed to decreased particle adhesion to the wall. However, particle recovery was not the focus of this thesis and will need further investigations. Potentially, particle recovery could further be improved when the DEP force is inverted for recovery so that particles experience nDEP and are repelled from pDEP trapping zones.

The approach of adjusting the fluid electric conductivity to achieve selective particle separation has a crucial limitation because it requires that the fluid is more electrically conductive than one of the involved particle types. This works only when at least one of the particles has a low conductivity. If the particles are too conductive, separation is impossible because the induced thermal energy (by Joule heating) increases linearly with the fluid conductivity, which is problematic when the involved particles are heat sensitive (e. g. biological cells). Further, Joule heating can result in boiling and bubbles, which can change the process and its selectivity significantly. An alternative approach, for upcoming investigations, would be to use the electric field frequency instead of the fluid electric conductivity to control the polarizability of the particles. For most particles the cross-over frequency (frequency at which the particle polarization changes) is in the range between 0.1 MHz and 10 MHz. In microfluidic DEP-based applications these frequencies can be applied easily and it is the most common way to control the particle polarizability.

High-throughput applications require significantly more electric power and thus more expensive power amplifiers, which were not available in this thesis. However, proving that frequency-controlled selective particle separation is possible would significantly increase the versatility of DEP filtration.

The development of DEP filtration techniques is in its early stage and needs further investigations before its full potential can be used. However, DEP filtration provides unique properties which can be used for a variety of existing separation processes or to make new and complex separation processes possible, such as material- and morphology-selective separation that have been achieved in microfluidic devices. Further, DEP filtration could potentially substitute existing but expensive separation processes. The features that were found in this study show that DEP filtration could be used as a stand-alone technique or as an additional (preparative) tool in combination with other separation techniques. Low costs and remarkable process simplicity make DEP filtration attractive for more research and development of test devices.

Appendix A

Particle fractions on the inside and outside of particle trajectories

Here it is described how the simulated particle trajectories (in Sec. 6.2.4) divide the total number of particles into two fractions: one towards the center of the flow and one towards the wall. In the following these fractions will be termed as inside and outside fraction.

It is assumed that particles are homogeneously dispersed in suspension when they enter the simulation cell. With this assumption, the particle flux at the inlet of the filter cell is proportional to the suspension flux. This means, that at any radial position on the inlet surface r_{traj}, the volumetric flow fraction towards the inside of this position ($r < r_{\mathrm{traj}}$) is equal to the fraction of particles towards the inside of this position. The same is valid for the volumetric and particle fraction at the outside of this position ($r > r_{\mathrm{traj}}$). It is therefore sufficient to determine the inside and outside fraction of the volumetric flow in order to determine the respective inside and outside particle number fractions.

The suspension flux through the inlet is equal to the the suspension velocity normal to the inlet surface, $v_{\mathrm{fluid,z}}$. The total volumetric flow through the inlet surface can be calculated by integrating $v_{\mathrm{fluid,z}}$ over the inlet cross section A_{inlet}. In cylinder coordinates this writes as:

$$Q_{\mathrm{total}} = \int_{r=0}^{r=R} v_{\mathrm{fluid,z}} 2\pi r \mathrm{d}r\,, \tag{A.1}$$

with the radial coordinate r and the pore radius $R = D_{\mathrm{p}}/2$. In the fluid flow simulations of Sec. 6 a hyperbolic velocity profile was used as boundary condition at the inlet. The velocity profile as a function of r can be written as $v_{\mathrm{fluid,z}} = C(R^2 - r^2)$, with the radius independent term C. Eq. (A.1) can then be solved as, $Q_{\mathrm{total}} = C(1/4R^4)$. The volumetric flow towards the inside of a the radial position r_{traj} can then be calculated as

$$Q_{\mathrm{inside}}(r_{\mathrm{traj}}) = \int_{r=0}^{r=r_{\mathrm{traj}}} v_{\mathrm{fluid,z}} 2\pi r \mathrm{d}r = C\left(\frac{1}{2}R^2 r_{\mathrm{traj}}^2 - \frac{1}{4}r_{\mathrm{traj}}^4\right). \tag{A.2}$$

Dividing this term by the the total flow through the inlet Q_{total} gives the inside fraction as $Q_{\text{inside}}/Q_{\text{total}}$. Since inside and outside fraction sum up to 1, the outside fraction can be determined by, $Q_{\text{outside}} = Q_{\text{total}} - Q_{\text{inside}}$.

This calculation was used to determine the minimum and maximum particle separation efficiencies in Tab. 6.1.

Appendix B

Fabrication of open porous alumina-mullite filters

The open porous ceramics were produced via direct foaming of a highly loaded particulate alumina-mullite suspension. After frothing the ceramic slurry by incorporation of air the foam can be cast in various forms and self-solidifies while drying. The dried green foam samples are reaction sintered at 1650°C to obtain their ceramic properties. After cooling down the porous ceramics can be easily sawed and shaped to any form with conventional tools.

The low air content in the foam, in contrast to polyhedral foams, caused the bubble like structure and the perfectly spherical cell geometry. Cell opening (window formation) in the foam took place in the first stadium of drying after a certain amount of water is evaporated and before the structure becomes rigid.

Pore and pore window sizes are influenced by process parameters and the initial recipe of the slurry. The duration of foaming and the rotational speed of the impeller while frothing have a strong impact on the cell size. Other Parameters like the air to suspension ratio of the foam and the solid load in the suspension as well as the grain size and form of the particles that are used influence the stability of the foam and also affect the size of the pore windows. Porous ceramic foams with no interconnected pores (closed cell foams that are impermeable) as well as highly interconnected pores (open cell foams with a high permeability) and everything in between can be manufactured with our production method.

The successful usage of these porous ceramic foams as a filter material shows that there are far more applications than the initial one, sound absorption under high temperature.

The production procedure and the ceramic foams are patented (Deutsche Patentanmeldung Nr. 10 2018 106 260.5). (Lorenz et al., 2020) ESM Section A.

Appendix C

Pore diameter and pore window diameter from CT data

CT image stacks (920 to 1016 images of 1004×1024 pixel) of the alumina filter structures were obtained with a CT scanner phoenix v|tome|x m research edition (General Electric) funded by MAPEX (Center for Materials and Processes, University of Bremen, Germany). All structures were scanned with 6 µm voxel edge length so that the observed volume had was a cube with 6 mm edge length and contained at least 4300 pores and 5600 pore windows. The image stacks (exemplary image from the stack in Figure S1a) were subsequently binarized (filter material = 0, porous volume = 1) with ImageJ by using the ImageJ integrated median filter with a radius of 2 pixels and removing noise and very small pores of 3 pixels in diameter (ImageJ, Process, Noise, Remove Outliners…) (Figure S1b). Subsequently the DIPimage package version 2.9 was used in MATLAB to generate a 3d structure from the stack data and segregate the resulting porous volume into pores by using the watershed algorithm on the Euclidian distance transformed image stack (Figure S1c). We accounted only for pores that were completely present in the observed volume (pores connected to the frame of the image stack were removed). For each pore we calculated the volume equivalent sphere diameter and determined the volume weighed median pore diameter $d_{p,3}$ representative for the pore size distribution. The area equivalent pore window diameter of each surface that separated two pores (black lines between pores in Figure S1c) was also determined. Subsequently the area weighed median diameter of the pore window diameter $d_{w,2}$ distribution was calculated. The hydraulic pore diameter was calculated by $d_h = 4V/S$, with the total surface area of the ceramic S and the void volume V.

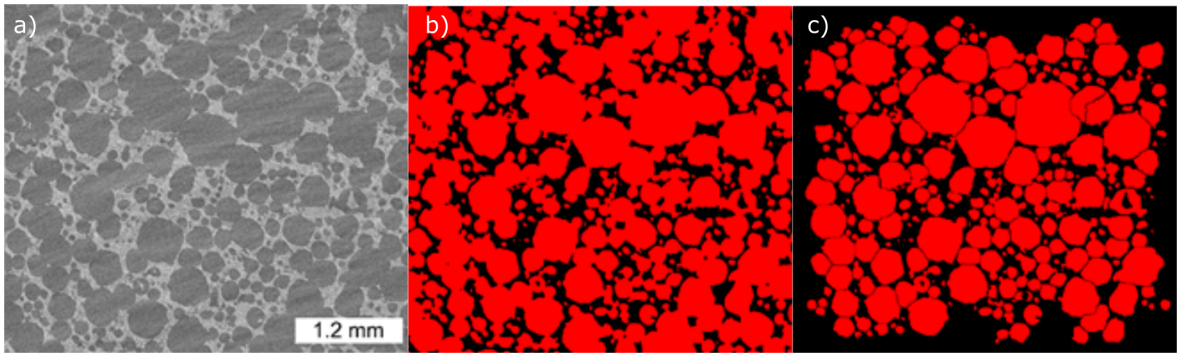

Figure C.1: The images show exemplary the progression from CT images to distinguished spherical pores for the ceramic maliM. We started with the unprocessed CT image (8-bit) (a). The image was then smoothened and binarized into solid and porous regions (b). Segmentation into spherical pores was done by cutting the pores at constrictions (3d watershed algorithm) (c).

Bibliography

Arnold, W. M., Schwan, H. P., and Zimmermann, U. (1987). Surface conductance and other properties of latex particles measured by electrorotation. *The Journal of Physical Chemistry*, 91(19):5093–5098.

Bazant, M. Z. (2011). Induced-Charge Electrokinetic Phenomena. In *Electrokinetics and Electrohydrodynamics in Microsystems*, pages 221–297. Springer Vienna, Vienna.

Bazant, M. Z. and Squires, T. M. (2010). Induced-charge electrokinetic phenomena. *Current Opinion in Colloid & Interface Science*, 15(3):203–213.

Bazant, M. Z., Thornton, K., and Ajdari, A. (2004). Diffuse-charge dynamics in electrochemical systems. *Physical Review E*, 70(2):021506.

Benguigui, L. and Lin, I. J. (1982). Dielectrophoretic Filtration of Nonconductive Liquids. *Separation Science and Technology*, 17(8):1003–1017.

Castellanos, A. (1998). *Electrohydrodynamics*, volume 380. Springer Vienna, Vienna.

Chou, C.-F., Tegenfeldt, J. O., Bakajin, O., Chan, S. S., Cox, E. C., Darnton, N., Duke, T., and Austin, R. H. (2002). Electrodeless Dielectrophoresis of Single- and Double-Stranded DNA. *Biophysical Journal*, 83(4):2170–2179.

Chow, R. S. and Takamura, K. (1988). Effects of surface roughness (hairiness) of latex particles on their electrokinetic potentials. *Journal of Colloid And Interface Science*, 125(1):226–236.

Derjaguin, B. V. (1934). Friction and adhesion. IV. The theory of adhesion of small particles. *Kolloid Zeits*, 69:155–164.

Einstein, A. (1905). Über die von der molekularkinetischen Theorie der Wärme geforderte Bewegung von in ruhenden Flüssigkeiten suspendierten Teilchen. *Annalen der Physik*, 14:549–560.

Ermolin, M. S. and Fedotov, P. S. (2016). Separation and characterization of environmental nano- and submicron particles. *Reviews in Analytical Chemistry*, 35(4):185–199.

Ermolina, I. and Morgan, H. (2005). The electrokinetic properties of latex particles: comparison of electrophoresis and dielectrophoresis. *Journal of Colloid and Interface Science*, 285(1):419–428.

Fernandez, R. E., Rohani, A., Farmehini, V., and Swami, N. S. (2017). Review: Microbial analysis in dielectrophoretic microfluidic systems. *Analytica Chimica Acta*, 966:11–33.

Friedlander, S. K. (2000). *Smoke, Dust, and Haze: Fundamentals of Aerosol Dynamics*. Topics in chemical engineering. Oxford University Press, New York.

Fritsche, G. R. and Haniak, L. W. (1975). US Patent 3,928,158.

Gan, L., Chao, T.-C., Camacho-Alanis, F., and Ros, A. (2013). Six-Helix Bundle and Triangle DNA Origami Insulator-Based Dielectrophoresis. *Analytical Chemistry*, 85(23):11427–11434.

García-Sánchez, P., Loucaides, N. G., and Ramos, A. (2017). Pumping of electrolytes by electrical forces induced on the diffusion layer: A weakly nonlinear analysis. *Physical Review E*, 95(2):022802.

Gascoyne, P. R. C., Noshari, J., Anderson, T. J., and Becker, F. F. (2009). Isolation of rare cells from cell mixtures by dielectrophoresis. *ELECTROPHORESIS*, 30(8):1388–1398.

Gascoyne, P. R. C. and Shim, S. (2014). Isolation of Circulating Tumor Cells by Dielectrophoresis. *Cancers*, 6(1):545–579.

Green, Y. and Yossifon, G. (2013). Dynamical trapping of colloids at the stagnation points of electro-osmotic vortices of the second kind. *Physical Review E*, 87(3):033005.

Grosse, C. and Shilov, V. N. (1996). Theory of the Low-Frequency Electrorotation of Polystyrene Particles in Electrolyte Solution. *The Journal of Physical Chemistry*, 100(5):1771–1778.

Haynes, W. M. (2016). *CRC Handbook of Chemistry and Physics (Internet Version)*. CRC Press, London, 97 edition.

Hirata, Y., Itoh, S., Shimonosono, T., and Sameshima, S. (2016). Theoretical and experimental analyses of Young's modulus and thermal expansion coefficient of the alumina-mullite system. *Ceramics International*, 42(15):17067–17073.

Hirata, Y., Matsushita, S., Ishihara, Y., and Katsuki, H. (1991). Colloidal Processing and Mechanical Properties of Whisker-Reinforced Mullite Matrix Composites. *Journal of the American Ceramic Society*, 74(10):2438–2442.

Hölzel, R., Calander, N., Chiragwandi, Z., Willander, M., and Bier, F. F. (2005). Trapping Single Molecules by Dielectrophoresis. *Physical Review Letters*, 95(12):128102.

Honegger, T., Berton, K., Picard, E., and Peyrade, D. (2011). Determination of Clausius–Mossotti factors and surface capacitances for colloidal particles. *Applied Physics Letters*, 98(18):181906.

Hughes, M. P. (2016). Fifty years of dielectrophoretic cell separation technology. *Biomicrofluidics*, 10(3):032801.

Hughes, M. P., Morgan, H., and Rixon, F. J. (2002). Measuring the dielectric properties of herpes simplex virus type 1 virions with dielectrophoresis. *Biochimica et Biophysica Acta - General Subjects*, 1571(1):1–8.

Iliescu, C., Xu, G., Loe, F. C., Ong, P. L., and Tay, F. E. H. (2007a). A 3-D dielectrophoretic filter chip. *ELECTROPHORESIS*, 28(7):1107–1114.

Iliescu, C., Xu, G. L., Ong, P. L., and Leck, K. J. (2007b). Dielectrophoretic separation of biological samples in a 3D filtering chip. *Journal of Micromechanics and Microengineering*, 17(7):S128–S136.

Israelachvili, J. N. (2015). *Intermolecular and surface forces*. Academic press.

Iwasaki, T., Slade, J. J., and Stanley, W. E. (1937). Some notes on sand filtration [with discussion]. *Journal (American Water Works Association)*, 29(10):1591–1602.

Johnson, W. P., Pazmino, E., and Ma, H. (2010). Direct observations of colloid retention in granular media in the presence of energy barriers, and implications for inferred mechanisms from indirect observations. *Water Research*, 44(4):1158–1169.

Jones, P. V., Salmon, G. L., and Ros, A. (2017). Continuous Separation of DNA Molecules by Size Using Insulator-Based Dielectrophoresis. *Analytical Chemistry*, 89(3):1531–1539.

Kallay, N., Torbić, Z., Barouch, E., and Jednac˘ak-Bis˘c˘an, J. (1987). The determination of isoelectric point for metallic surfaces. *Journal of Colloid and Interface Science*, 118(2):431–435.

Kang, K. H. and Li, D. (2006). Dielectric Force and Relative Motion between Two Spherical Particles in Electrophoresis. *Langmuir*, 22(4):1602–1608.

Kawabata, T. and Washizu, M. (2001). Dielectrophoretic detection of molecular bindings. *IEEE Transactions on Industry Applications*, 37(6):1625–1633.

Kosmulski, M. (2001). *Chemical Properties of Material Surfaces*. Surfactant Science. CRC Press.

LaLonde, A., Romero-Creel, M. F., Saucedo-Espinosa, M. A., and Lapizco-Encinas, B. H. (2015). Isolation and enrichment of low abundant particles with insulator-based dielectrophoresis. *Biomicrofluidics*, 9(6):064113.

Lapizco-Encinas, B. H. (2019). On the recent developments of insulator-based dielectrophoresis: A review. *ELECTROPHORESIS*, 40(3):358–375.

Leroy, P., Devau, N., Revil, A., and Bizi, M. (2013). Influence of surface conductivity on the apparent zeta potential of amorphous silica nanoparticles. *Journal of Colloid and Interface Science*, 410:81–93.

Lin, I. J. and Benguigui, L. (1982). Dielectrophoretic Filtration of Liquids. II. Conducting Liquids. *Separation Science and Technology*, 17(5):645–654.

Lin, I. J. and Benguigui, L. (1985). Dielectrophoretic Filtration in Time-Dependent Fields. *Separation Science and Technology*, 20(5-6):359–376.

Lorenz, M., Malangré, D., Du, F., Baune, M., Thöming, J., and Pesch, G. R. (2020). High-throughput dielectrophoretic filtration of sub-micron and micro particles in macroscopic porous materials. *Analytical and Bioanalytical Chemistry*.

Mandzy, N., Grulke, E., and Druffel, T. (2005). Breakage of TiO2 agglomerates in electrostatically stabilized aqueous dispersions. *Powder Technology*, 160(2):121–126.

Matula, R. A. (1979). Electrical resistivity of copper, gold, palladium, and silver. *Journal of Physical and Chemical Reference Data*, 8(4):1147–1298.

McDowell-Boyer, L. M., Hunt, J. R., and Sitar, N. (1986). Particle transport through porous media. *Water Resources Research*, 22(13):1901–1921.

Menéndez, J. A., Illán-Gómez, M. J., y León, C. A., and Radovic, L. R. (1995). On the difference between the isoelectric point and the point of zero charge of carbons. *Carbon*, 33(11):1655–1657.

Molnar, I. L., Pensini, E., Asad, M. A., Mitchell, C. A., Nitsche, L. C., Pyrak-Nolte, L. J., Miño, G. L., and Krol, M. M. (2019). Colloid Transport in Porous Media: A Review of Classical Mechanisms and Emerging Topics. *Transport in Porous Media*, 130(1):129–156.

Morgan, H. and Green, N. G. (2003). *AC Electrokinetics: Colloids and Nanoparticles*. Microtechnologies and microsystems series. Research Studies Press, Baldock.

O'Konski, C. T. (1960). Electric properties of macromolecules. V. Theory of ionic polarization in polyelectrolytes. *The Journal of Physical Chemistry*, 64(5):605–619.

Pesch, G. (2018). *On the dielectrophoretic particle retention in porous media*. PhD thesis, University of Bremen.

Pesch, G. R. and Du, F. (2020). A review of dielectrophoretic separation and classification of non-biological particles. *ELECTROPHORESIS*, page elps.202000137.

Pesch, G. R., Du, F., Baune, M., and Thöming, J. (2017). Influence of geometry and material of insulating posts on particle trapping using positive dielectrophoresis. *Journal of Chromatography A*, 1483:127–137.

Pesch, G. R., Du, F., Schwientek, U., Gehrmeyer, C., Maurer, A., Thöming, J., and Baune, M. (2014). Recovery of submicron particles using high-throughput dielectrophoretically switchable filtration. *Separation and Purification Technology*, 132:728–735.

Pesch, G. R., Kiewidt, L., Du, F., Baune, M., and Thöming, J. (2016). Electrodeless dielectrophoresis: Impact of geometry and material on obstacle polarization. *ELECTROPHORESIS*, 37(2):291–301.

Pesch, G. R., Lorenz, M., Sachdev, S., Salameh, S., Du, F., Baune, M., Boukany, P. E., and Thöming, J. (2018). Bridging the scales in high-throughput dielectrophoretic (bio-)particle separation in porous media. *Scientific Reports*, 8(1):10480.

Pethig, R. (2010). Review Article—Dielectrophoresis: Status of the theory, technology, and applications. *Biomicrofluidics*, 4(2):022811.

Pethig, R. (2017a). *Dielectrophoresis*. John Wiley & Sons, Ltd, Chichester, UK.

Pethig, R. (2017b). Review-where is dielectrophoresis (DEP) going? *Journal of the Electrochemical Society*, 164(5):B3049–B3055.

Peukert, W. and Wadenpohl, C. (2001). Industrial separation of fine particles with difficult dust properties. *Powder Technology*, 118(1-2):136–148.

Pierson, H. O. (1993). Graphite Structure and Properties. In Pierson, H. O., editor, *Handbook of Carbon, Graphite, Diamonds and Fullerenes*, pages 43–69. Elsevier, Oxford.

Pohl, H. A. (1951). The Motion and Precipitation of Suspensoids in Divergent Electric Fields. *Journal of Applied Physics*, 22(7):869–871.

Pohl, H. A. and Hawk, I. (1966). Separation of Living and Dead Cells by Dielectrophoresis. *Science*, 152(3722):647–649.

Ramos, A., García-Sánchez, P., and Morgan, H. (2016). AC electrokinetics of conducting microparticles: A review. *Current Opinion in Colloid & Interface Science*, 24:79–90.

Ramos, A., Morgan, H., Green, N., and Castellanos, A. (1999). The role of electrohydrodynamic forces in the dielectrophoretic manipulation and separation of particles. *Journal of Electrostatics*, 47(1):71–81.

Ramos, A., Morgan, H., Green, N. G., and Castellanos, A. (1998). Ac electrokinetics: a review of forces in microelectrode structures. *Journal of Physics D: Applied Physics*, 31(18):2338–2353.

Schwarz, G. (1962). On the low-frequency dielectric dispersion of colloidal particles in electrolyte solution. *The Journal of Physical Chemistry*, 66(12):2636–2642.

Sisson, W. G., Brunson, R. R., Scott, T. C., Harris, M. T., and Look, J. L. (1995). Removal of Submicron Silica Particles from tert -Amyl Alcohol by Dielectric/Electric Packed Bed Filtration. *Separation Science and Technology*, 30(7-9):1421–1434.

Squires, T. M. and Bazant, M. Z. (2004). Induced-Charge Electro-Osmosis. *Journal of Fluid Mechanics*, 509(509):217–252.

Srivastava, S. K., Artemiou, A., and Minerick, A. R. (2011). Direct current insulator-based dielectrophoretic characterization of erythrocytes: ABO-Rh human blood typing. *ELECTROPHORESIS*, 32(18):2530–2540.

Suehiro, J., Guangbin Zhou, Imamura, M., and Hara, M. (2003). Dielectrophoretic filter for separation and recovery of biological cells in water. *IEEE Transactions on Industry Applications*, 39(5):1514–1521.

Thamida, S. K. and Chang, H.-C. (2002). Nonlinear electrokinetic ejection and entrainment due to polarization at nearly insulated wedges. *Physics of Fluids*, 14(12):4315–4328.

Tuncuk, A., Stazi, V., Akcil, A., Yazici, E., and Deveci, H. (2012). Aqueous metal recovery techniques from e-scrap: Hydrometallurgy in recycling. *Minerals Engineering*, 25(1):28–37.

Wakamatsu, T. and Numata, Y. (1991). Flotation of graphite. *Minerals Engineering*, 4(7-11):975–982.

Wakeman, R. and Butt, G. (2003). An Investigation of High Gradient Dielectrophoretic Filtration. *Chemical Engineering Research and Design*, 81(8):924–935.

Wakeman, R. and Tarleton, S. (2005). *Solid/liquid Separation: Principles of Industrial Filtration*. Elsevier Advanced Technology, Oxford, UK.

Wang, Q., Dingari, N. N., and Buie, C. R. (2017). Nonlinear electrokinetic effects in insulator-based dielectrophoretic systems. *Electrophoresis*, 38(20):2576–2586.

Wei, M. T., Junio, J., and Ou-Yang, D. H. (2009). Direct measurements of the frequency-dependent dielectrophoresis force. *Biomicrofluidics*, 3(1):1–9.

Weirauch, L., Lorenz, M., Hill, N., Lapizco-Encinas, B. H., Baune, M., Pesch, G. R., and Thöming, J. (2019). Material-selective separation of mixed microparticles via insulator-based dielectrophoresis. *Biomicrofluidics*, 13(6):064112.

Yossifon, G., Frankel, I., and Miloh, T. (2006). On electro-osmotic flows through microchannel junctions. *Physics of Fluids*, 18(11):117108.

Zangwill, A. (2012). *Modern Electrodynamics*. Cambridge University Press.

Zehavi, M., Boymelgreen, A., and Yossifon, G. (2016). Competition between Induced-Charge Electro-Osmosis and Electrothermal Effects at Low Frequencies around a Weakly Polarizable Microchannel Corner. *Physical Review Applied*, 5(4):044013.

Zhao, H. (2011). Double-layer polarization of a non-conducting particle in an alternating current field with applications to dielectrophoresis. *ELECTROPHORESIS*, pages n/a–n/a.

Zhao, H. and Bau, H. H. (2009). The polarization of a nanoparticle surrounded by a thick electric double layer. *Journal of Colloid and Interface Science*, 333(2):663–671.

List of Symbols

Roman

$\bar{v}_{\text{fluid}}$	superficial fluid velocity	$\mathrm{m\,s^{-1}}$
$\bar{x}$	correlation of relevant parameters for DEP separation efficiency	depends
$\hat{\mathbf{E}}$	amplitude of the electric field vector	$\mathrm{V\,m^{-1}}$
a	point vector between dipole charges	m
D	electric flux	$\mathrm{C\,m^{-2}}$
E	electric field vector	$\mathrm{V\,m^{-1}}$
$\mathbf{E}_{\text{RMS}}$	root-mean-square value of the electric field vector	$\mathrm{V\,m^{-1}}$
$\mathbf{E}_0$	applied electric field vector	$\mathrm{V\,m^{-1}}$
F	force vector	N
P	polarization	$\mathrm{C\,m^{-2}}$
p	dipole moment	Cm
v	velocity vector	$\mathrm{m\,s^{-1}}$
x	point vector	m
$\tilde{f}_{\text{CM}}$	complex Clausius-Mossotti factor	–
a	particle radius ($a = d_{\text{p}}/2$)	
A_{H}	Hamaker coefficient	J
C	constant	depends
c	number concentration	$\mathrm{m^{-3}}$

c	number concentration	m^{-3}
C_{DL}	double layer charge capacity	$\mathrm{F}\,\mathrm{m}^{-1}$
c_{ion}	number density of ions in solution	m^{-3}
D_{BM}	particle diffusion coefficient	$\mathrm{m}^2\,\mathrm{s}^{-1}$
d_{h}	hydraulic diameter	m
D_{p}	pore diameter	m
d_{p}	particle diameter	m
D_{w}	pore window diameter	m
E	electric field strength	$\mathrm{V}\,\mathrm{m}^{-1}$
E_0	applied electric field strength	$\mathrm{V}\,\mathrm{m}^{-1}$
F	force	N
f	frequency	s^{-1}
f_{CM}	Clausius-Mossotti (CM) factor	–
F_{DEP}	dielectrophoretic force	N
F_{drag}	drag force	N
f_{D}	friction factor	$\mathrm{kg}\,\mathrm{s}^{-1}$
f_{RC}	relaxation frequency to charge a particle DL	s^{-1}
i	imaginary unit ($i^2 = -1$)	–
K	electric conductance	S
k	thermal conductivity	$\mathrm{W}\,\mathrm{m}^{-1}\,\mathrm{K}^{-1}$
L	length	m
Q	electric charge	C
Q	volumetric flow rate	$\mathrm{m}^3\,\mathrm{s}^{-1}$
q_{th}	volume specific thermal energy	$\mathrm{J}\,\mathrm{m}^{-3}$
R	particle recovery rate	%

r	radius	m
T	temperature	K
U	voltage	V
V	volume	m^3
v	velocity	$m\,s^{-1}$
v_{fluid}	fluid velocity	$m\,s^{-1}$
W	energy	J
x	distance	m
y	distance	m
z	ion valence	–

Greek

α	electric polarizability	Fm^2
$\mathbf{\Gamma}$	torque	Nm
χ	electric susceptibility	–
ΔU	applied voltage	V
η	dielectrophoretic separation efficiency	%
η_{mech}	mechanical (depth filtration) separation efficiency	%
κ^{-1}	Debye length	m
λ_D	Debye length	m
μ	dynamic viscosity	Pa s
μ_{DEP}	dielectrophoretic mobility	$m^4\,V^{-2}\,s^{-1}$
μ_{EP}	electrophoretic mobility	$m^2\,V^{-1}\,s^{-1}$
μ_{ICEO}	induced-charge electroosmotic mobility	$m^2\,V^{-1}\,s^{-1}$
ω	angular frequency	$rad\,s^{-1}$
ρ	charge or mass density	$C\,m^{-3}$

ρ_s	surface specific charge density	$\mathrm{C\,m^{-2}}$
σ	electric conductivity	$\mathrm{S\,m^{-1}}$
σ_m	fluid (medium) electric conductivity	$\mathrm{S\,m^{-1}}$
σ_p	particle electric conductivity	$\mathrm{S\,m^{-1}}$
τ	relaxiation time	s
$\tilde{\varepsilon}$	complex permittivity	$\mathrm{F\,m^{-1}}$
ε	permittivity ($\varepsilon = \varepsilon_r \varepsilon_0$)	$\mathrm{F\,m^{-1}}$
ε_m	fluid (medium) permittivity	$\mathrm{F\,m^{-1}}$
ε_p	particle permittivity	$\mathrm{F\,m^{-1}}$
ε_r	relative permittivity	–
Φ	potential	V
ζ	zeta potential	V

Physics Constants

ε_0	permittivity of vacuum	$8.854 \times 10^{-12}\,\mathrm{F\,m^{-1}}$
k_B	Boltzmann constant	$1.38 \times 10^{-23}\,\mathrm{m^2\,kg\,s^{-2}\,K^{-1}}$
q_e	charge of an electron	$1.602 \times 10^{-19}\,\mathrm{C}$

Abbreviations

ac	alternating current
CT	computer tomography
CTCs	circulating tumor cells
dc	direct current
DEP	dielectrophoresis
DL	double layer
DLVO theory	Derjaguin-Landau-Verwey-Overbeck theory
ICEO	induced-charge electroosmosis

iDEP insulator-based dielectrophoresis

iep isoelectric point

nDEP negative dielectrophoresis

pDEP positive dielectrophoresis

PDMS polydimethylsiloxane

PS polystyrene

RMS root mean square

SEM scanning electron microscopy

vdW van der Waals

Students' work

In this dissertation, the results from the supervision of the following students' work is included:

Mahmoud Bizreh, "Selektivität in der dielektrophoretischen Filtration - Experimentelle Studie am Beispiel von Polystyrolpartikeln", *M. Sc. Thesis*, March 2019

Declaration

I hereby declare that I completed this dissertation without any unauthorized third party assistance, used no other sources or aids than the ones specified, and properly marked content and text passages that have been included word-by-word or by content from other sources as such. Further, I hereby declare that the electronic version of the doctoral thesis enclosed for examination purposes is identical to the submitted printed version.

Bremen, 02.12.2020

Malte Lorenz

Erklärung

Ich erkläre hiermit, dass ich die vorliegende Arbeit ohne unerlaubte fremde Hilfe angefertigt, keine anderen als die von mir angegebenen Quellen und Hilfsmittel benutzt und Stellen, die den benutzten Werken wörtlich oder inhaltlich entnommen wurden, als solche kenntlich gemacht habe. Desweiteren erkläre ich, dass die zu Prüfungszwecken beigelegte elektronische Version der Dissertation identisch ist mit der abgegebenen gedruckten Version.

Bremen, 02.12.2020

Malte Lorenz